Flow-Dependent Corrosion in Turbulent Pipe Flow

A thesis

Submitted to the College of Graduate Studies and Research

in Partial Fulfillment of the Requirements

for the Degree of

Doctor of Philosophy

in the Department of Chemical Engineering

University of Saskatchewan, Saskatoon

by

Yueping Wang

FALL 1997

UNIVERSITY OF SASKATCHEWAN

College of Graduate Studies and Research

SUMMARY OF DISSERTATION

Submitted in partial fulfillment

of the requirements for the

DEGREE OF DOCTOR OF PHILOSOPHY

by

Yueping Wang

Department of Chemical Engineering
University of Saskatchewan

FALL 1997

Examining Committee:

Dr. S. Sokhansanj	~~Dean/Associate Dean~~ Dean's Designate, Chair College of Graduate Studies and Research
Dr. D.-Y. Peng	Chair of Advisor Committee, Department of Chemical Engineering
Dr. J. Postlethwaite	Supervisor, Department of Chemical Engineering
Dr. D. J. Bergstrom	Co-supervisor, Department of Mechanical Engineering
Dr. M. N. Esmail	Department of Chemical Engineering
Dr. S. Yannacopoulos	Department of Mechanical Engineering

External Examiner:

Dr. P. Tontiwachwuthikul
Faculty of Engineering
University of Regina
Regina, Saskatchewan
S4S 0A2

Flow-Dependent Corrosion in Turbulent Pipe Flow

Flow-dependent corrosion in turbulent pipe flow is a complex process with enhanced mass transport, development of concentration gradients and film formation which all affect the corrosion rate. The objectives of this study are the numerical simulation and experimental investigation of the effects of flow on the corrosion rate and film formation and disruption under both attached and disturbed flow conditions.

The turbulence model (based on Launder and Spalding's standard k-ε model) is modified with a recently developed low Reynolds number (LRN) model in the near wall region. This modification enables the near-wall limiting behavior to be reproduced correctly and the species concentration to be determined all the way down to the wall, which makes it possible to determine pipe-wall mass transfer accurately.

Comparison has been made between the simulation with the LRN k-ε model and the experimental results of others for the mass transfer. Good agreement is reported between the predictions and the experimental results in both the mass transfer entry length and the fully developed region. Effects of mass transfer on the corrosion of metals are simulated throughout the mass transfer entrance region. Profiles of corrosion rate, surface metal ion concentration and surface pH for corrosion under charge transfer control; oxygen-mass transfer control; and anodic partial mass transfer control are presented. The concentration profiles along the entrance region are discussed in terms of their effects on film formation. The turbulence model is also applied to the numerical simulation of the effects of both electrode misalignment and electrode length on corrosion rate measurements in turbulent pipe flow. Both protruding and recessed electrodes are considered with misalignment in the range 0 to 500 μm. The formation and disruption of the corrosion films on a flat copper surface in flowing 3% NaCl solutions are also studied under disturbed flow conditions. The development and destruction of the corrosion films are observed through the transparent cell top. The resulting interactions between the disturbed flow and the films are discussed in terms of the near-wall turbulence parameter profiles and the mass transfer profile along the length of flow cell, calculated using LRN k-ε turbulence model.

In presenting this thesis in partial fulfillment of the requirements for a Postgraduate degree from the University of Saskatchewan, I agree that the Libraries of this University may make it freely available for inspection. I further agree that permission for copying of this thesis in any manner, in whole or in part, for scholarly purpose may be granted by the professor or professors who supervised my thesis work or, in their absence, by the Head of the Department or the Dean of the college in which my thesis work was done. It is understood that any copying or publication or use of this thesis or parts thereof for financial gain shall not be allowed without my written permission. It is also understood that due recognition shall be given to me and to the University of Saskatchewan in any scholarly use which may be made of any material in this thesis.

Requests for permission to copy or to make use of material in this thesis in whole or part should be addressed to:

Head of the Department of Chemical Engineering
University of Saskatchewan
Saskatoon, Saskatchewan
Canada
S7N 5C9

To my family

Acknowledgments

Thanks are due in the first place to my supervisors Dr. J. Postlethwaite and Dr. D. J. Bergstrom. Firstly, to Dr. J. Postlethwaite for his financial assistance, exceptional support and sound guidance during all stages of my work. Secondly, to Dr. D. J. Bergstrom for his critical review of the work and this manuscript.

In addition, I would like to thank my committee members: Dr. M. N. Esmail, Dr. D.-Y. Peng and Dr. S. Yannacopoulos for their supervision.

My special thanks go to Guang Yang, my wife, for her encouragement and support in all aspects of my life and especially through the last five and half years.

Financial support also came from the University of Saskatchewan in the form of a graduate scholarship and computing facilities.

Abstract

Flow-dependent corrosion in turbulent pipe flow is a complex process with enhanced mass transport, development of concentration gradients and film formation which all affect the corrosion rate. Flow-dependent corrosion can be accelerated in the mass transfer entry length, where the concentration boundary layers of both oxidants and corrosion products are developing, and under disturbed flow condition, where the high intensity fluctuations produced by flow separation and reattachment can disturb the mass transfer boundary layer and disrupt corrosion product films if they are present on the metal surface.

This thesis describes the application of the low Reynolds number (LRN) k-ε eddy viscosity model and an electrochemical (or corrosion) model to simulate the corrosion rate, the metal/solution interface concentration of both oxidants and corrosion products, and the film formation conditions in turbulent pipe flow. The overall objectives of this study were the numerical simulation and experimental investigation of the effects of flow on the corrosion rate and film formation and disruption under both attached and disturbed flow conditions.

The turbulence model used in this study is based on the standard k-ε model proposed by Launder and Spalding (1974). The model was modified with a recently

developed LRN model (Abe et al, 1994) in the near wall region which enables the calculation of species concentration all the way down to the wall. The mass transfer was modelled by simultaneously solving the transport equation for mass, momentum, kinetic energy of turbulence and its dissipation as well as species concentration. The corrosion model was developed to construct E/log*i* diagrams which take into account the effects of mass transfer resistance on the anodic and cathodic reactions.

The pipe-wall mass transfer in the mass transfer entrance region has been simulated with LRN k-ε model and tested against the experimental results of Berger and Hau (1977), in the range $Re=10^4$ to 10^5, for Sc=2244, and of Son and Hanratty (1967), in the range $Re=10^4$ to 5×10^4, for Sc=2400, in both the mass transfer entrance region and the fully developed region and good agreement was reported. The application of small cathodes embedded in a larger active cathode to measure local mass transfer rates was also simulated. The size of the electrode and the thickness of the electrical insulation around the small electrode give rise to errors that increase as the insulation thickness increases and the electrode size decreases.

Effects of mass transfer on the corrosion of metals were simulated throughout the mass transfer entrance region in turbulent pipe flow. Iron was chosen to represent metals with a low exchange current density and copper those whose anodic dissolution is more reversible. Profiles of corrosion rate, surface metal ion concentration and surface pH for corrosion under charge transfer control; oxygen-mass transfer control; and anodic partial

mass transfer control are presented. The concentration profiles along the entrance region are discussed in terms of their effect on film formation.

The turbulence models have also been applied to the numerical simulation of the effect of electrode misalignment on corrosion rate measurements in turbulent pipe flow. The effect of the mass transfer entry length was also taken into consideration. Both protruding and recessed electrodes were considered with misalignment in the range 0 to 500 μm. The determination of the effect for partially mass transfer controlled corrosion rate measurements is illustrated.

The formation and disruption of the corrosion films on a flat copper surface in flowing 3% NaCl solutions were also studied in a flow cell with a rectangular cross section, 50 mm wide × 15 mm high. The 140 mm long copper deck and the symmetrical cover had backward and forward facing 2 mm steps to form a constriction resulting in disturbed flow in the immediate downstream region of the sudden constriction and the recirculation zone downstream of the sudden expansion. The bulk velocity range based on the unconstricted cross section of the flow cell was 0.3~1.49 m/s. The development and destruction of the corrosion films were observed through the transparent cell top. The resulting interactions between the disturbed flow and the films are discussed in terms of the near-wall turbulence parameter profiles and the mass transfer profile along the length of flow cell, calculated by the application of LRN k-ε turbulence model.

TABLE OF CONTENTS

LIST OF FIGURES

LIST OF TABLES

List of symbols

a_P, a_E, a_W, a_N, a_S transport coefficients in the discretized transport equations

$\tilde{c}$, c, c' species concentration (instantaneous, mean, fluctuating components)

C_μ, $C_{\varepsilon 1}$, $C_{\varepsilon 2}$ turbulence model constants

D, D_t diffusion coefficient (molecular, eddy)

d diameter of straight pipe

d_e equivalent diameter

E electrode potential or additive constant in the law of the wall

F Faraday constant, 96500 c/mol

F_e, F_w, F_n, F_s mass flow rate through the faces of the control volume

f_μ, f_1, f_2 turbulence model functions

i_0 exchange current density

i_a , i_c partial current density (anodic, cathodic)

J_e, J_w, J_n, J_s integrated total fluxes over the control-volume faces

K local mass transfer coefficient

<K> mean mass transfer coefficient

K^+ dimensionless local mass transfer coefficient, K/U_τ

$<K^+>$ dimensionless mean mass transfer coefficient, $<K>/U_\tau$

k	kinetic energy of turbulence, $\frac{1}{2}\overline{u_i' u_i'}$
L	distance from the mass transfer entrance
L^+	dimensionless distance from the entrance, LU_τ/ν
l	turbulence length scale
l_m	mixing length
[ ]	metal ion, complex ion, H^+, OH^-, and O_2 concentration
P	pressure term
P'	pressure correction
P_e	Peclet number, $\frac{\rho U \Delta s}{\Gamma}$
P_k	production of turbulence
R	gas constant, 8.314 J/mol K
r	radial coordinate
Re	Reynolds number
Re_t	turbulence Reynolds number, $\rho k^2 / \mu\varepsilon$
S	source term
Sc	Schmidt number, ν/D
S_C	constant or coefficient of the linearized source term
S_P	coefficient of the linearized source term
St_d	local Stanton number, K/U_b
$<St_d>$	mean Stanton number, $< K >/U_b$
S_{ij}	instantaneous strain-rate tensor

t_{ij} instantaneous viscous stress tensor

U_b bulk flow velocity

U, V, W mean velocity components in x, y, z directions

u, v, w instantaneous velocity components in x, y, z directions

u', v', w' fluctuating velocity components in x, y, z directions

u_i, U_i, u_i' instantaneous, mean, fluctuating velocities in tensor notation

$\hat{u}$ velocity scale

U^+ dimensionless mean velocity

U_τ friction velocity, $(\tau_w/\rho)^{1/2}$

u_ε Kolmogorov velocity, $(\nu\varepsilon)^{1/4}$

x axial coordinate

x_i position vector in tensor notation

y distance from the wall

y^+ dimensionless distance from the wall, yU_τ/ν

y^* dimensionless distance from the wall, yu_ε/ν

z charge of ion

Greek symbols

α relaxation factor

α_a, α_c transfer coefficient

Γ diffusion coefficient

δy distance of nearest node from wall surface

ε dissipation of kinetic energy of turbulence, $\nu\overline{\frac{\partial u_i'}{\partial x_j}\frac{\partial u_i'}{\partial x_j}}$

η, η_t, η_b overpotential, E-E_{rev}

η_{ct} charge transfer overpotential

η_d diffusion overpotential

κ Karman constant

μ molecular viscosity

μ_t eddy or turbulent viscosity

ν kinematic molecular viscosity

ν_t kinematic eddy or turbulent viscosity

ρ fluid density

$\sigma_k, \sigma_\varepsilon, \sigma_m$ turbulent Prandtl-Schmidt numbers

Φ general variable

Subscripts

b bulk value

eff effective value (molecular + turbulent)

f nearest node from wall surface

k kinetic energy of turbulence

lim limiting value

s metal surface

t	turbulent value
w	wall
∞	fully developed value

Overbar

$\bar{}$	time-averaging

Acronyms

AKN	Abe, Kondoh and Nagano
DNS	direct numerical simulation
EVM	eddy viscosity model
LES	large eddy simulation
LDCT	limiting diffusion current technique
LDV	laser Doppler velocimetry
LHS	left hand side
LRN	low Reynolds number
RHD	right hand side
RMS	root mean square
NT	Nagano and Tagawa
SEM	scanning electron microscope

1. Introduction

The effect of fluid flow on corrosion is a subject of continuing scientific interest and practical concern for the testing of materials, prediction of performance in the field, and modelling of the corrosion process at a fundamental level. The corrosion that is associated with or affected by fluid flow is often called flow-dependent corrosion, which can be classified into flow-accelerated corrosion and erosion-corrosion in single phase liquid flow. Flow-accelerated corrosion can be defined as increased corrosion from increasing turbulence intensity and mass transfer as a result of the flow of a fluid over a surface (Efird et al, 1993). Erosion-corrosion is defined as accelerated corrosion as a result of the degradation and/or removal of protective film on metal surface due to the impingement of fluid as a result of the flow of fluid over the metal surface. The present study addressed both flow-accelerated corrosion and erosion-corrosion.

Flow-dependent corrosion can occur in a variety of industrial systems including oil/gas production piping systems, power plant piping systems, and heat exchangers and condensers. Flow-dependent corrosion can result in serious damage and possible

catastrophic failure of these system from both a safety and economic point of view (Chexal et al, 1996).

Flow-dependent corrosion in pipe flow can be enhanced in the mass transfer entrance region where the concentration boundary layers of both oxidants (e.g. O_2 and H^+) and corrosion products (e.g. Fe^{2+}, Cu^+, and Cu^{2+}) are developing. Also higher corrosion rates occur under disturbed flow conditions where flow separation and reattachment produce high intensity turbulence and mass transfer that can lead to an increased corrosion rate. The high intensity fluctuations can also cause the disruption of protective film if they are present on metal surface.

The overall objectives of this study were the numerical simulation and experimental investigation of the effects of flow on the corrosion rate, film formation and film disruption under both attached and disturbed flow conditions. The detailed objectives were:

- Investigation of effects of mass transfer on the corrosion rate, surface metal ion concentration and surface pH in mass transfer entrance region and the prediction of the possibility of film formation on the corroding metal surface using a LRN k-ε model and an electrochemical model.
- Prediction of the effect of electrode misalignment and electrode length on electrochemical corrosion rate measurements in turbulent pipe flow using a LRN k-ε model.

- Determination of the flow conditions (flow rate, geometrical structure of the test cell) under which the formation and removal of corrosion product films are observed. Correlation of observed film formation and disruption condition with modelled near-wall turbulence profile, mass transfer profile and surface concentration profiles of corroded species and pH profile along the length of copper specimen corroding under disturbed flow condition.

This study is a continuation of the previous work done in the same laboratory on straight pipe erosion-corrosion in single phase and two phase flows (Postlethwaite et al, 1986; Nesic and Postlethwaite, 1990; 1991a; 1991b; 1991c). The "original" numerical code (using a k-ε turbulence model) which was used by Nesic (1991) and Adamopoulos (1995) was fine-tuned and modified with a recently developed low Reynolds number (LRN) model in the near wall region. This modification can satisfy the wall limiting behavior and enable the calculation of variables concerned all the way down to the wall. An electrochemical model was also developed which is based on the rate equations for the anodic dissolution of the metal and cathodic reduction of the oxidants concerned. This electrochemical model took into account the effect of mass transport of both reactants and corrosion products so that the surface metal ion concentration and surface pH can be predicted.

In the following chapter (Chapter 2), the existing research results on modelling studies in turbulent flow, modelling and experimental studies on mass transfer and modelling studies on corrosion under attached and disturbed flow conditions have been

reviewed. The studies of the stability of corrosion film on copper surface in flowing NaCl solution have also been reviewed in this chapter.

In Chapters 3, 4, and 5, the models of turbulence, mass transfer, and corrosion used in present studies are described. The turbulence model which is based on the standard k-ε eddy viscosity turbulence model proposed by Launder and Spalding (1974) was described, together with a low Reynolds number (LRN) formulation for the near wall region. For the model of mass transfer, the time-averaged transport equation for species was described, as well as the eddy diffusivity relation used in the transport equation. The species transport equation has been solved simultaneously with the transport equations of flow, using a LRN model in the near-wall region. Special attention has been paid to the arrangement of the grid points in the near-wall region in order to evaluate the mass transfer coefficient accurately. In the corrosion model, a mechanistic model taking into account mass transfer effects has been adopted which is based on the rate equations for the anodic dissolution of the metals concerned (Cu, Fe) and for the cathodic reduction of oxidants such as O_2, H^+.

In Chapter 6, the LRN k-ε turbulence model was first used to predict the mass transfer coefficients in the mass transfer entrance region (Wang et al, 1996), and compared with previous experimental measurements (Berger and Hau, 1977; Son and Hanratty, 1967). Then, the k-ε turbulence model and the electrochemical model are used to predict corrosion rates, corrosion product concentration and pH on metal surfaces, and film formation condition in the mass transfer entry length (Wang and Postlethwaite,

1997). Both the k-ε turbulence model and the corrosion model were further used to predict the effect of electrode misalignment and electrode length on the electrochemical corrosion rate measurement (Wang et al, 1997; Postlethwaite and Wang, 1996). Some experimental studies were made to determine the flow conditions under which the formation and removal of corrosion product film are observed. The experimental observations were discussed in relation to the modelled near-wall turbulence, wall shear stress, mass transfer and corrosion product concentration and pH on metal surface, predicted using the LRN k-ε turbulence model and the corrosion model.

Conclusions were made based on the present studies and future work was recommended. These are presented in Chapter 7.

2. Literature Review

2.1. Introduction

Flow-dependent corrosion in turbulent pipe flow is a complex process with enhanced mass transport, development of a concentration gradient and film formation which all affect the corrosion rate. The study of flow-dependent corrosion covered in this thesis includes several individual topics such as mass transfer entrance length, corrosion in mass transfer entrance length, effects of entrance length and electrode misalignment on corrosion rate measurement, and film growth and removal under disturbed flow conditions. Since this study is primarily devoted to the modelling of mass transfer and corrosion in turbulent pipe flow under attached and disturbed flow conditions, previous modelling studies on turbulence flow, mass transfer and corrosion are reviewed in this section. Related experimental studies are also mentioned since these experimental studies can be used to validate the turbulence model in the prediction of the hydrodynamic parameters and mass transfer parameters or as a benchmark for the development of the corrosion model. The literature review consists of the following four

parts: 1). Modelling studies in turbulent pipe flow; 2). Modelling and experimental studies on mass Transfer; 3). Modelling studies on corrosion, 4). Copper corrosion in flowing chloride solution.

2.2. Modelling Studies in Turbulent Pipe Flow

The turbulence models can be classified as: zero-, one-, or two-equation models; Reynolds stress model; large eddy simulation; and direct numerical simulation models. The **n-equation** model represents a model that requires solution of **n** additional differential transport equations in addition to those expressing the transport equations of mass and momentum.

The zero-equation model (also called algebraic model) is the simplest turbulence model to use the Boussinesq eddy-viscosity concept. The first zero-equation model, called the mixing-length model, was suggested by Prandtl (1925). It relates the eddy viscosity to the local mean-velocity gradient and involves a single unknown parameter, the mixing length, l_m, and can be expressed as follows:

$$\nu_t = l_m^2 \left| \frac{\partial U}{\partial y} \right| \tag{2-1}$$

There are many other zero-equation models such as the ones of Cebeci and Smith (1974) and Baldwin and Lomax (1978). Such models can only be applied to relatively simple flow where l_m can be specified by simple empirical formulae and lack generality.

One-equation models also use the eddy viscosity concept. In such models (e.g. Goldberg, 1991) the Kolmogorov-Prandtl expression ($\nu_t = C_\mu k^{0.5} l$) is used where k, kinetic energy of turbulence, can be determined by solving the transport equation of this quantity, while l, the length scale, needs to be specified. Although the one-equation model performs better than the zero-model in general, it still cannot account for more complex flow because of the difficulty of specifying empirically the length-scale distribution in more complex flow. To reach a more-nearly universal model, especially for separated flow, more advanced models are needed in which transport effects on the turbulence length scale are also accounted for.

Two-equation models provide computations not only for k, but also for the turbulent length scale or equivalent. Consequently, two-equation models are complete and can be used to predict properties of a given turbulent flow without prior knowledge of the turbulence structure. The most popular two-equation model is the k-ε model, which was first proposed by Jones and Launder (1972). In the k-ε model the turbulent length scale in the Kolmogorov-Prandtl expression ($\nu_t = C_\mu k^{0.5} l$) is expressed as: $l \propto k^{3/2}/\varepsilon$. Other two-equation models include k-ω model (Saffman and Wilcox, 1974) and k-kl model (Rotta, 1951). The k-ε model has been used in this study since the model has been well established for shear-layers and confined recirculating flows and is becoming a powerful tool for solution of many engineering problems.

Unlike the zero-, one- and two-equation models where the Reynolds stresses, $\overline{u_i' u_j'}$, are modelled using eddy viscosity model relation, the Reynolds stress model aims to calculate $\overline{u_i' u_j'}$ by solving the transport equations themselves. These transport equations can be derived in exact form, but they contain higher order correlations that have to be approximated in order to obtain a closed system. The increased complexity of the equations and the large amount of computational effort required are counterbalanced by more accurate solutions especially for the Reynolds shear stress. Reynolds stress models have been used in the simulation of complex turbulent flows (Farhanieh et al, 1993; Nikjooy and Mongia, 1991), and will become more popular as more powerful computers are available in the near future.

The idea for large eddy simulation (LES) is to do a three-dimensional time-dependent numerical computation of the large-scale turbulence while modelling the small-scale motions. The underlying premise is that the largest eddies are directly affected by the boundary conditions and must be computed. By contrast, the small-scale turbulence is more nearly isotropic and has universal characteristics; it is thus more amenable to modelling. A direct numerical simulation (DNS) means a complete time-dependent solution of the Navier-Stokes and continuity equations (Kim et at, 1987). Although the cost of such simulations is still high with computers of the early 1990's, both LES and DNS will receive extensive application as more and more powerful computers appear in the future.

In this study attention will be focused on the application of the k-ε model to calculate the mass transfer coefficient, near-wall turbulence parameters and wall shear stress in turbulent pipe (or duct) flow under attached and disturbed flow conditions. A few previous simulation studies in straight pipe flow will be reviewed, as well as some simulation studies on axisymetric flow in a sudden pipe (or duct) expansion or constriction are also reviewed since part work of this study involves flow in a pipe with a sudden change in pipe diameter. As indicated by Nallasamy (1987), flow in a pipe expansion is one of the basic problems encountered in common engineering flow systems. The separated, reattached and recirculating flow downstream of the expansion greatly affects the transport of momentum, heat and mass, which lead to enhanced heat and mass transfer rate.

2.2.1. Straight Pipe under Attached Flow Conditions

A form of the k-ε turbulence model was first proposed by Harlow and Nakayama (1968). Jones and Launder (1972; 1973) and Launder and Spalding (1974) presented more detailed descriptions of the k-ε model and reviewed some predictions using the k-ε model. In nature, the k-ε model is valid only for fully turbulent flows. In the near wall regions, the local turbulent Reynolds number is so small that viscous effects predominate over turbulent ones. Two methods have been developed to account for near wall regions in numerical methods for computing turbulent flow: the wall function (WF) method and low-Reynolds number (LRN) method. In the wall function method, the first node close to the wall is placed in the region where y^+ is between 30 to 150 and a

uniform shear stress prevails. This results in the "logarithmic velocity profile" and the generation and dissipation of energy are in balance (Launder and Spalding, 1974). Application of the low Reynolds number method extends the k-ε model from fully turbulent flow to the laminar flow in the near-wall region. Launder and Spalding (1974) compared the predicted velocity profile using a low Reynolds number method in the near wall region with experimental measurement (Kudova and Sesonske, 1972) for Re=6000. The prediction is in general accord with the experimental data except in the region $10<y^+<40$ where the prediction is lower than the experimental measurement.

Martinuzzi and Pollard (1989), and Pollard and Martinuzzi (1989) presented comparative studies of turbulence models in predicting turbulent pipe flow. They compared eleven turbulence models including a high Reynolds number k-ε model of Launder and Spalding (1974), a low Reynolds number model of Lam and Bremhorst (1981), four algebraic stress models, and five Reynolds stress models. The comparison was made for axial velocity profile, Reynolds shear stress, turbulence kinetic energy, *etc.* in developing turbulent pipe flow with Reynolds number of 10^4 to 3.8×10^5. They found that the results obtained with a low Reynolds number k-ε model are generally in better agreement with experimental data than those obtained from the high Reynolds number model and other models, especially at low Reynolds number. However, one flaw in the low Reynolds number model of Lam and Bremhorst (1981) is that it predicts limiting behavior for Reynolds shear stress $\overline{u'v'} \propto y^4$ as the wall is approached, while the correct limiting behavior is believed to be $\overline{u'v'} \propto y^3$ (Wilcox, 1993). Another flaw is that the

Lam and Bremhorst (1981) low Reynolds number model fails to make model function, f_μ, to satisfy the limiting behavior, $f_\mu \propto y^{-1}$. The f_μ is one of the damping functions which are responsible for modifying the turbulent field by taking into account the viscous effect in the near-wall region. Modifications aiming to remove the above-mentioned defects of the k-ε models have been developed since then. Myong et al (1989) presented an improved low-Reynolds number k-ε model and compared the predicted mean velocity, eddy diffusivity and Reynolds shear stress profiles with experimental data and other k-ε models including the one proposed by Lam and Bremhorst (1981). They reported better agreement between the prediction and experimental data, especially for the limiting behavior of the Reynolds shear stress.

Nagano and Tagawa (1990) also modified the damping functions f_μ, f_1 and f_2 as well as the model constants for a low Reynolds number k-ε model based on the limiting behavior near the wall. With the improved model, the above-mentioned defects of the k-ε model have been removed. They have verified the validity of the improved form of the k-ε model in the light of the experimental data.

In summary, the improved low Reynolds number k-ε models can now been used to reproduce the mean velocity profile and the limiting behavior of wall for $\overline{u'v'}$, k, and υ_t in turbulent pipe flow. This is very important to the application of the k-ε model to calculating near wall species concentration profile and local mass transfer coefficient.

2.2.2. Straight Pipe under Disturbed Flow Conditions

One of the earliest simulation studies of the two-dimensional turbulent recirculating flow using the k-ε model was done by Gosman et al (1979). They used a wall function (WF) k-ε model to calculate the flow properties (velocity, kinetic energy of turbulence and its dissipation rate) and to predict the reattachment length downstream of an axisymetric sudden enlargement. The predictions made were compared with the experimental measurement of Back and Roschke (1972). They reported good agreement between the prediction and experimental results for the reattachment length, but poor agreement for swirling-pipe flow and bluff-body stabilized flow which is attributed to the performance of the dissipation equation.

Gould et al (1990) compared the predicted results using a k-ε model with their own simultaneous two-component Laser Doppler Velocimetry (LDV) measurements made in the incompressible turbulent air flow field following an axisymmetric expansion. They reported good agreement for the mean axial velocity, kinetic energy of turbulence and Reynolds shear stress, but poor agreement for the radial velocity and the normal turbulent stresses. The disagreement was partially attributed to the inability of the eddy-viscosity models to account for the anisotropy of the flow.

In the above-mentioned model studies, the wall function model has been used. However, as pointed out by Wilcox (1993), there are some problems in the application of wall functions in disturbed flow conditions because the law of the wall does not

always hold for flow near solid boundaries, most notably for separating flows. While recently developed low Reynolds number models, like the one proposed by Nagano and Tagawa (1990), can reproduce the limiting behavior of the wall in a straight pipe flow, they have a singularity problem related to the simulation of recirculating flow in a sudden expansion because the model functions f_μ and f_2 contain the friction velocity, u_τ, and will collapse at separating and reattaching points where $u_\tau = 0$.

More recently Abe et al (1994) have modified the low Reynolds number model proposed by Nagano and Tagawa (NT) (1990) for calculating the complex turbulent flows with separation and reattachment. They introduced a new velocity scale of turbulence, $u_\varepsilon \equiv (\nu\varepsilon)^{1/4}$, to replace u_τ in the NT model and to reevaluate the model constants. They used the revised model to calculate the flow structure for a backward facing step flow and compared their results with various experimental cases. They reported excellent agreement for reattachment length between prediction and experimental data for a variety of experimental conditions. They also reported good agreement for axial velocity, turbulent kinetic energy and Reynolds shear stress for the backward facing step flow in addition to good agreement for mean velocity and eddy viscosity between prediction and direct simulation data (DNS) (Abe et al, 1994) for straight pipe flow. This improved low Reynolds number k-ε model will be used throughout this study.

Chang et al (1995) performed a similar modification to the low Reynolds number model aiming to remove the singular problem related to the simulation of recirculating

flow in a sudden-expansion pipe. However, they introduced "$\sqrt{k}$", instead of $u_\varepsilon \equiv (\nu\varepsilon)^{1/4}$, to replace u_τ as the velocity scale of turbulence. They compared their prediction with the modified model with the experimental data of Durret et al (1988) and reported good agreement for the reattachment length, mean axial velocity and turbulent kinetic energy at five axial stations in pipe-expansion flow.

It is concluded from the review that significant improvement in predictions of flow properties particularly in the near wall region of the reattachment point can be achieved through the use of the improved low Reynolds number model (e. g. Abe et al, 1994; Chang et al, 1995). It is realized that the eddy viscosity is an important transport property in modelling turbulent transport of momentum, heat and mass. The accurate prediction of the f_μ distribution in a near wall region is a prerequisite for correct simulation of wall mass transfer.

2.3. Mass Transfer

2.3.1. Experimental Studies

Many experimental studies have been done during the last three decades on measurement of mass transfer rate in straight pipe flow (e.g. Shaw et al, 1963; Son and Hanratty, 1967; Berger and Hau, 1977), in swirling flow (e.g. Yapici et al, 1994), and in the pipe flow with sudden expansion (Runchal, 1971; Sydberger and Lotz, 1982). The

following discussion will be limited to the mass transfer in straight pipe flow, for both mass transfer entrance region and fully developed region.

Two techniques have been developed to measure mass transfer coefficient. One technique is to measure the dissolution rate of soluble sections of a pipe wall, as used by Linton and Sherwood (1950), and Meyerink and Friedlander (1962). One disadvantage of this technique is that the surface roughness and internal diameter of the test section change during the experiment and will affect the measurement accuracy. The other technique is so called limiting diffusion current technique (LDCT). This technique has received extensive application in evaluating transport phenomena in hydrodynamic environments. The details of the LDCT have been described by Wragg (1977), and Berger and Ziai (1983).

Shaw et al (1963), Son (1965), and Son and Hanratty (1967) investigated the effect of the length of the mass transfer section on the rate of mass transfer. In these studies, ten test sections with internal diameter of 25.4 mm and varying lengths from 0.0177 to 4.31 pipe-diameter were used with Reynolds number from 4000 to 62000 and Schmidt number of 2400. They found that the measured mean mass transfer coefficient as a function of length of mass transfer section fits nicely with following correlation

$$< K^{+} >= 0.81 L^{+^{-0.33}} Sc^{-0.67} \qquad (2\text{-}2)$$

with the smallest transfer section showed the poorest agreement equation.

Berger and Hau (1977) measured mass transfer coefficients in mass transfer entrance length and in fully developed flow in smooth pipe using LDCT. Their studies include experiments with nine mass transfer sections with an internal diameter of 54.8 mm and varying length from 0.008 to 9.12 pipe-diameter. The Reynolds number ranges from 12900 to 135000 with a Schmidt number of 2400. They concluded that when the concentration boundary layer was fully developed, the results could be represented by the relation

$$St_d = 0.0165\,\mathrm{Re}^{-0.14}\,Sc^{-0.67} \tag{2-3}$$

In the mass transfer entrance section where the concentration boundary layer is developing, they plotted the mean Stanton number as a function of dimensionless distance from the entrance for one Schmidt number and varying Reynolds numbers and found that the experimental data in the linear parts of the lines agree well with the integrated turbulent Leveque equation

$$St_d = 0.276\,\mathrm{Re}^{-0.417}\,Sc^{-2/3}\left(\frac{L}{d}\right)^{-1/3} \tag{2-4}$$

They also show that the validity range of equation (2-4) is dependent on the Reynolds number and change from $0<L/d<0.5$ for $Re\leq 10^4$ to $0<L/d<0.1$ for $Re>10^5$.

From this short review it is clear that there are several reliable and detailed mass transfer measurements in the mass transfer entrance region and fully developed region in straight pipe that can be used for the validation of the mass transfer model. The above

experimental data (Son and Hanratty, 1967; Berger and Hau, 1977) have been used for the verification of the mass transfer prediction in the present study (section 6.2.3).

2.3.2. Modelling Studies

2.3.2.1.Mass Transfer Entry Length

There is no report available in the literature on the modelling studies for mass transfer entrance length in turbulent pipe flow. An analytical method for the calculation of mean mass transfer coefficient in mass transfer entrance region in a pipe flow was presented by Linton and Sherwood (1950). For the condition of large Schmidt numbers, the concentration boundary layer is much thinner than the viscous sublayer. Therefore, the curvature of the wall may be neglected, and the concentration profile may be described in a Cartesian coordinate system. Furthermore, the mean velocity within the concentration boundary layer may be simplified as a linear function of y:

$$U = \frac{u_\tau^{\,2}}{\nu} y \tag{2-5}$$

With equation (2-5), the time averaged transport equation of species in turbulent straight pipe flow with very large Schmidt number can be expressed as

$$\frac{u_\tau^{\,2}}{\nu} y \frac{\partial c}{\partial x} = \frac{\partial}{\partial x}\left(D\frac{\partial c}{\partial x}\right) + \frac{\partial}{\partial y}\left(D\frac{\partial c}{\partial y}\right) - \frac{\partial(\overline{u'c'})}{\partial x} - \frac{\partial(\overline{v'c'})}{\partial y} \tag{2-6}$$

Linton and Sherwood (1950) have suggested that equation (2-6) can be simplified as

$$\frac{u_\tau^{\,2}}{\nu} y \frac{\partial c}{\partial x} = D\frac{\partial^2 c}{\partial y^2} \tag{2-7}$$

Integrating equation (2-7) and using the Blasius relation yield

$$\langle St_d \rangle = 0.276\,\mathrm{Re}^{-0.417}\,Sc^{-2/3}\left(\frac{L}{d}\right)^{-1/3} \tag{2-8}$$

There are two defects with the above correlation (2-8) and its derivation process. One defect is that the term, $-\frac{\partial(\overline{u'c'})}{\partial x}$, in equation (2-6) was omitted without sound explanation (Shaw et al, 1963). Another defect is that equation (2-8) has a very limited range of validity as it applies only to less than 10% mass transfer entry length (Wang and Postlethwaite, 1997). A LRN k-ε turbulence model has been used in the present study to calculate the local and mean mass transfer coefficients throughout the mass transfer entrance region to the fully developed mass transfer region.

2.3.2.2.Disturbed Flow Conditions

There are very few modelling studies on the mass transfer downstream of an abrupt pipe expansion in turbulent pipe flow. Amano (1985) presented a modelling study of turbulent mass transport downstream of an abrupt pipe expansion using the k-ε turbulence model. Attention has been focused on the simulation of the region in the immediate vicinity of the wall, by formulating a near-wall model for the evaluation of the mean generation and destruction rate of the ε equation. The detailed near-wall model was also presented by Amano in a separate paper (Amano, 1983). The computed results were compared with the experimental data of Runchal (1971). The predicted Stanton numbers are in general higher than the experimental data and the predicted maximum Stanton number position is always upstream of the measured one. One ambiguous point in his study is the calculation of the local Stanton number, since the first near wall node

used by Amano (1985) is at $y^+ = 29 \sim 36$ which is not within the mass transfer controlled diffusion sublayer (even not in the viscous sublayer) and Fick's first law cannot be simplified here.

In the experiment of Runchal (1971), a nozzle is used followed by the straight pipe with a larger pipe diameter forming a sudden pipe expansion. It is not clear if the hydrodynamic flow conditions for the nozzle were taken into account when the inlet flow condition was set for calculating of mass transfer along the pipe. All these factors would affect the calculation of the mass transfer.

Nesic et al (1992) performed the calculation of mass transfer in a pipe involving sudden pipe expansion using a LRN k-ε model (Lam and Bremhorst, 1981). The predictions were compared with the data reported by Sydberger and Lotz (1982) for Reynolds numbers of 2.1×10^4 to 1.3×10^5. The predicted mass transfer is in general higher than the experimental data using a turbulent Schmidt number of $\sigma_m = 0.9$ throughout the computational domain. With $\sigma_m = 1.7$ used in the near wall region ($y^+<5$), the predictions are in better agreement with the experimental data.

Herrero et al (1994) presented a numerical study aiming to investigate the effect of grid size on the calculation of mass transfer rate using the LRN model proposed by Lam and Bremhorst (LB) (1981) and a modification of Herreo et al (1991) which is also based on the Lam and Bremhorst (LB) model. The predictions were compared with the data of both Sydberger and Lotz (1982) at $Re=4.2\times10^4$ and Sc=1460, and Runchal

(1971) at Re=6.53×10^4 and Sc=2500. However, use of the Lam and Bremhorst model for calculating wall mass transfer has been questioned by Nagano and Tagawa (1990) and Abe et al (1994), because the LB model gives the incorrect near-wall limiting behavior for the Reynolds stress, $\rho\overline{u'v'}$, and the damping function, f_μ. Hence correct prediction of mass transfer could not be expected in high Schmidt number flow. On the other hand, the experiments were performed in a straight pipe with various sizes and types of orifices. The experimental data used for comparison with the predictions are obtained from an experiment in a straight pipe with a diameter of 4.0 cm downstream from a flow obstacle consisting of an orifice with an inner diameter of 2.0 cm and with a length of 2.0 cm in the flow direction. In the simulation studies by Nesic et al (1992), the inlet boundary of the computational domain is at the sudden expansion section where inlet flow conditions have to be guessed as the hydrodynamic condition of flow at the sudden expansion section is not given by the original experiment. This might be one of the factors which affects the accuracy of the prediction for the mass transfer downstream of sudden expansion.

It can be concluded from the above review that there is no well defined experimental measurement for mass transfer along with hydrodynamic parameters of flow available for pipe flow with sudden expansion. Such an experiment should provide detailed hydrodynamic data (in addition to detailed mass transfer data) which could be used as boundary conditions for a numerical simulation. On the other hand, the improved LRN model, such as the AKN model, can reproduce the near wall limiting behavior correctly and therefore can predict both attached and separated wall shear flows

accurately. But, the AKN LRN model has not yet been tested against experimental data for mass transfer under disturbed flow conditions.

2.4. Modelling Studies on Corrosion

There is a large number of corrosion models which are available in literature. Many of them are for CO_2 corrosion (e.g. DeWaard and Milliams, 1975; Gray et al, 1989, 1990; DeWaard and Lotz, 1993; Dustad et al, 1994; Nesic et al, 1996). Based on how firmly they are theoretically based, these models can be classified as mechanistic models (models describing the mechanism of the underlying corrosion process have a strong theoretical background), semi-empirical models (models based only partially on firm theoretical background) and empirical models (models based very little on theoretical background and most of the constants used have little physical meaning). Since the corrosion model used in this study is based on a mechanistic model, some mechanistic models are described in this section.

Corrosion is a very complex phenomenon relating to the surface electrochemical reaction and the transport process of reactants and corrosion products. A mechanistic model is based on the rate equations of anodic dissolution of metals and of cathodic reduction of oxidants (e.g. O_2, H^+). All kinetic parameters have physical meaning and are available from experimental measurements.

DeWaard and Milliams (1975) were among the first to develop an electrochemical model for Fe-CO_2 solution system. They derived the rate equation of anodic dissolution

of iron based on the pH-dependent mechanism proposed by Bockris et al (1961). For the mechanism of cathodic reaction, they suggested that the reduction of undissociated carbonic acid is the rate-determining step. The resulting model can quantitatively explain their own experimental results and can predict the effects of temperature and CO_2 partial pressure on corrosion rate.

Gray et al (1989; 1990) presented an electrochemical model as part of their experimental studies of CO_2 corrosion. The cathodic reduction reactions taken into account include H^+ reduction, H_2CO_3 reduction and water reduction. The anodic dissolution reaction considered is the oxidation of Fe to Fe^{2+} which is based on pH-dependent mechanism (Bockris et al, 1961). The electrochemical model has been used successfully to calculate the active dissolution rate of carbon steel at 25 °C and to resolve complex polarization curves in their constituent oxidation and reduction reactions. The model can also be used to predict the effect of partial pressure of CO_2 (P_{CO_2}) and fluid flow rate on corrosion rate.

Nesic et al (1996) conducted a follow up study on CO_2 corrosion. The cathodic reactions considered include: H^+ reduction, O_2 reduction, direct reduction of H_2CO_3 and H_2O. The charge transfer controlled oxidation of Fe to Fe^{2+} was adopted for the dissolution of iron. When modelling the limiting current density of H^+ and O_2 reduction reactions, the correlations of Berger and Hau (1977), and of Eisenberg et al (1954) were used for straight pipe flow and for rotating cylinder flow system. They reported that the corrosion model developed can be used to predict corrosion rate, to determine the

governing corrosion mechanism (charge transfer control, mass transfer control, reaction or mixed control), and to predict the effect of temperature, pH, flow velocity and P_{CO_2} on corrosion rate and governing corrosion mechanism.

From the above review it is seen that mechanistic corrosion models have received quite extensive application in CO_2 corrosion. Although the corrosion systems dealt with in the present study are Fe-H_2O, Cu-H_2O and Cu-NaCl solution systems which are different from Fe-CO_2 solution system. The well established theoretical path developed or used by DeWaard and Milliams (1975), Gray et al (1989; 1990), and Nesic et al (1996) has been adopted in developing corrosion models taking into account the effect of mass transfer in turbulent pipe flow for Fe-H_2O, Cu-H_2O and Cu-NaCl solution systems.

2.5. Stability of Corrosion Product Film on Copper in Flowing NaCl Solution

Copper and its alloys have been used widely in marine environments for many years because of their resistance to corrosion in sea water. This resistance is a result of the formation of protective layers on the metal surface which provides a diffusion barrier for the transport of species involved in the corrosion process. However, copper and its alloys are known to be susceptible to enhanced corrosion in sea water when there is sufficient relative motion between the metal and the fluid (Efird, 1977; Wood et al, 1990). Danek (1966) conducted exposure tests to Cu-based alloys and other alloys and found that Cu-based alloys exhibit excellent corrosion resistance at low velocities but are

subject to excessive degradation by erosion-corrosion at higher velocities. It was thought that the protective corrosion films are removed from the metal surface at these higher velocities.

There are several possible mechanisms for the film removal or disruption from metal surface in single phase flowing solution:

- Dissolution or removal of protective layers by hydrodynamic shear stress occurs when the shear stress is greater than the binding force between the film and the substrate (Efird, 1977).

- In disturbed flow conditions, local near-wall intensity of turbulence has been proposed as the governing factor for the removal of film. Intensive turbulence fluctuations close to the wall contribute to disrupting the protective corrosion product film and disturbing the mass transfer boundary layer, thus enhancing the corrosion rate (Blatt and Heitz, 1990; Nesic and Postlethwaite, 1990).

- Dissolution of films which are controlled by mass transfer. Thus the breakaway velocity may reflect conditions where the dissolution rate of film is greater than the growth rate of film (Syrett, 1976).

Over the past few decades an attempt was made to find universal fluid parameters which could be related to the onset of accelerated corrosion which is triggered by the disruption of the protective corrosion product film. These parameters include bulk flow

velocity (Copson, 1952), bulk Reynolds number (Mahato et al, 1968; Shemilt et al, 1980), wall shear stress (Efird, 1977; Silverman, 1984), and the local near-wall turbulence (Blatt and Heitz, 1990; Nesic and Postlethwaite, 1990).

For a simple flow geometry like straight pipe flow, an increase in bulk velocity corresponds to higher Reynolds number, higher wall stress and higher local turbulence in the near-wall region. In this case the simplest parameter, a critical or breakaway velocity is most often used as a criterion. In industry, the bulk flow velocity is often used as a design parameter in terms of breakaway velocity. For instance, the design velocity for CA 706 (89Cu-10Ni-1Fe) is typically 1.5 to 2.1 m/s for 2.54 cm diameter tubes (Syrett, 1976).

However, the velocity or Reynolds number as a criterion will fail when results from two different flow systems (e.g., rotating cylinder system and straight pipe system) are compared because similar flow velocity and Reynolds numbers defined by two systems do not guarantee the similarities in hydrodynamics and mass transfer, and the results from two different studies are not comparable. In this case, critical velocity or Reynolds number cannot be used as a criterion.

Use of wall shear stress overcomes this problem. Based on the idea that corrosion product film on metal surface degrades and is physically removed when the wall shear stress exceeds the binding force between the corrosion film and the substrate, Efird (1977) presented a study in which the critical wall shear stress can be found for copper-based alloys in flowing sea water. He suggested that these data can be applied to other

hydrodynamic systems to determine the critical sea water flow velocity for a specific application.

Although the removal of protective layer by wall shear stress has been accepted by many researchers as the cause of accelerated corrosion of copper, this cause has been questioned by others who suggested that the adhesion forces for oxide film are too large for the film to be removed by hydrodynamic forces (Syrett, 1976; Bianchi, et al, 1978; MacDonald et al, 1978).

Disturbed flow conditions are often encountered in industry under which turbulence is transported downstream from the point of separation and there is no simple relation between the bulk flow parameters and the local near-wall hydrodynamic and mass transfer conditions. In these systems there is no similarity between wall shear stress and the turbulence profiles. Blatt and Heitz (1990), and Nesic and Postlethwaite (1990) have proposed the local near-wall turbulence as a key parameter related to the onset of accelerated corrosion. Near-wall turbulent fluctuation interferes with the formation of protective films and also affects the rate of mass transfer of both corrosion reactants and products by disrupting corrosion product film and thinning the diffusion controlled mass transfer boundary layer. The study of Lotz and Postlethwaite (1990) has shown that for a flow through a sudden pipe expansion the position of highest rate of erosion-corrosion is close to the point of flow reattachment. Since the wall shear stress, calculated based on mean velocity gradient at the wall, is zero at the reattachment point, use of wall shear stress as a sole explanation for film removal is not appropriate.

Based on their numerical simulations, Nesic and Postlethwaite (1991a) have shown that the maximum value position of the local level of turbulence is close to the point of flow reattachment where maximum rate of erosion-corrosion was observed (Lotz and Postlethwaite, 1990), and suggested that the near-wall turbulence level could be the determining factor.

Chemical dissolution of film can also occur as an additional mechanism for film removal. Syrett (1976) suggested that the so-called erosion-corrosion of oxide film may actually be the result of mass transfer phenomena. Thus, the breakaway velocity may reflect conditions where the rate of film removal (e.g., by dissolution in sea water) is higher than the rate at which the film can reform by other competing reactions.

Under service conditions involving disturbed flow (such as at elbows, weld beads, various fillings and other sudden change in flow geometry) the corrosion product film can differ from place to place in many aspects: thickness, porosity, compactness, etc. These differences lead to variation in film strength and protectivity. So, it is possible under certain flow conditions that a corrosion film can not form on the metal surface in some areas even in the initial service stage, and accelerated corrosion occurs in these areas. Bianchi et al (1978) presented a study on "Horse Shoe" corrosion of copper alloys in flowing sea water, in which the influence of mass transfer on film formation on copper surface was discussed in detail. They proposed that the 'Horse Shoe' corrosion, which takes place preferentially at the inlet region of a pipe (e.g., in condenser), is the localization of the active anodic dissolution reaction in small areas, in which the high

rate of mass transfer inhibits the formation of a protective film of corrosion products (Cu_2O). It has been proposed that the formation of stable passive film depends on a delicate balance between the diffusion of the chloride cuprous complexes ($CuCl_2^-$) formed by the primary anodic reaction:

$$Cu + 2Cl^- \Leftrightarrow CuCl_2^- + e^- \tag{2-9}$$

and the precipitation reaction

$$2CuCl_2^- + 2OH^- \Leftrightarrow Cu_2O + H_2O + 4Cl^- \tag{2-10}$$

The surface pH, which is produced by the reduction of oxygen at a metal surface and has an overriding influence on the film of stable Cu_2O film, could also be affected by mass transfer condition as proposed by Bianchi et al (1978). An increase in mass transfer results in decreases of both surface pH and surface $CuCl_2^-$ concentration, and hence, in the reversal of reaction (2-10). Furthermore, the oxidation of the Cu_2O film results eventually in the formation of a top layer of sparingly soluble atacamite, $Cu_2(OH)_3Cl$ (Wood et al, 1990).

3. Model of Turbulence

3.1. Introduction

The task of a turbulence model is to provide equations which enable calculation of the Reynolds stress, $\overline{u_i' u_j'}$, which arise when the time averaged Navier-Stokes equations are obtained from the instantaneous Navier-Stokes equations. In this chapter, the time-averaging process of the instantaneous Navier-Stokes equations were first briefly introduced. The eddy viscosity model and the k-ε model were then presented. Finally the numerical process to solve the resulting set of partial differential equations was briefly summarized.

3.2. Instantaneous Flow Equations

For incompressible flow, the instantaneous equations for conservation of mass and momentum can be expressed as:

Mass conservation: continuity equation

$$\frac{\partial u_i}{\partial x_i} = 0 \tag{3-1}$$

Momentum conservation: Navier-Stokes equations

$$\rho \frac{\partial u_i}{\partial t} + \rho u_j \frac{\partial u_i}{\partial x_j} = -\frac{\partial p}{\partial x_i} + \frac{\partial t_{ij}}{\partial x_j} \tag{3-2}$$

The term t_{ij} in equation (3-2) is the instantaneous viscous stress tensor defined by

$$t_{ij} = 2\mu s_{ij} \tag{3-3}$$

where s_{ij} is the instantaneous strain-rate tensor

$$s_{ij} = \frac{1}{2}\left(\frac{\partial u_i}{\partial x_j} + \frac{\partial u_j}{\partial x_i}\right) \tag{3-4}$$

The instantaneous equations (3-1) and (3-2) cannot at present be solved for turbulent flows of practical relevance since turbulence consists of random fluctuations of the various flow properties. Therefore, a statistical approach has been taken as explained in the following section.

3.3. Time Averaged Flow Equations

Based on Reynolds decomposition rules (Reynolds, 1895), the instantaneous values of the velocity, u_i, and the pressure, p, in equations (3-1) and (3-2) are separated into mean and fluctuating quantities:

$$u_i = U_i + u_i', \quad p = P + p' \tag{3-5}$$

The mean quantities in above equations are defined as

$$U_i = \frac{1}{T}\int^{+T} u_i dt, \quad P = \frac{1}{T}\int^{+T} p dt \tag{3-6}$$

where the averaging time, T, is long compared with the time scale of turbulent motion.[1] If the overbar ($\bar{}$) is used to denote time-averaging, the following relationships are satisfied:

$$\bar{a} = a, \text{ if } a = const \tag{3-7}$$

$$\overline{af} = a\bar{f}, \text{ if } a = const \tag{3-8}$$

$$\overline{f+g} = \bar{f} + \bar{g} \tag{3-9}$$

$$\frac{\overline{\partial f}}{\partial s} = \frac{\partial \bar{f}}{\partial s}, \text{ where } s \text{ is } x_1, x_2, x_3 \text{ or } t \tag{3-10}$$

$$\overline{af'} = a\overline{f'} = 0, \text{ if } a = const \tag{3-11}$$

$$\overline{\bar{f}g} = \bar{f}\bar{g} \tag{3-12}$$

If equation (3-5) is substituted into equations (3-1) and (3-2), and the relationships (3-7), (3-8), (3-9), (3-10), (3-11), (3-12) are employed, the time averaged conservation equations of mass and momentum, after some manipulation, are given as:

$$\frac{\partial U_i}{\partial x_i} = 0 \tag{3-13}$$

[1] In a transient problem, the averaging time has to be small compared with the time scale of the mean flow.

$$\rho\frac{\partial U_i}{\partial t}+\rho U_j\frac{\partial U_i}{\partial x_j}=-\frac{\partial P}{\partial x_i}+\frac{\partial}{\partial x_j}\left[\mu\left(\frac{\partial U_i}{\partial x_j}+\frac{\partial U_j}{\partial x_i}\right)-\rho\overline{u_i'u_j'}\right] \tag{3-14}$$

The equation (3-14) is usually referred to as the Reynolds-averaged Navier-Stokes equation. The quantity, $-\rho\overline{u_i'u_j'}$, is known as the Reynolds-stress tensor and is denoted by τ_{ij}, i.e.

$$\tau_{ij}=-\rho\overline{u_i'u_j'} \tag{3-15}$$

Since $\tau_{ij}=\tau_{ji}$, this is a symmetric tensor. We have introduced one additional unknown variable as a result of the time-averaging process. Unfortunately, we have gained no additional equations. For example, in two-dimensional flow, we have three mean-flow properties, pressure (P), and two velocity components (U_1 and U_2) plus one Reynolds-stress component ($-\rho\overline{u_i'u_j'}$), in total four unknowns. The equations available are the continuity equation (3-13) and momentum equations (3-14) for a total of three. This illustrates the closure problem of turbulence. In order to compute all mean-flow properties of the turbulent flow under consideration, we need a prescription for computing $\overline{u_i'u_j'}$. The function of turbulence modelling is to devise approximations for $\overline{u_i'u_j'}$ in term of flow properties that are known so that a sufficient number of equations exists. In making such approximations, we close the system of equations. In this study, the turbulence modelling is divided into two steps: 1) eddy viscosity relations for the Reynolds stress, and 2) a model for the eddy viscosity.

3.4. Eddy Viscosity Relations

Boussinesq's (1877) eddy-viscosity relation is the oldest proposal for modelling the Reynolds stress, $-\rho\overline{u_i'u_j'}$, and has become a significant part of most turbulence models of practical use today. The eddy viscosity relation assumes that, in analogy to the viscous stresses in laminar flows, the turbulent stresses are proportional to the mean-velocity gradients. For general flow situations, the eddy viscosity relation can be expressed as

$$-\overline{u_i'u_j'} = \nu_t\left(\frac{\partial U_i}{\partial x_j}+\frac{\partial U_j}{\partial x_i}\right)-\frac{2}{3}k\delta_{ij} \tag{3-16}$$

where ν_t is the kinematic turbulent or eddy viscosity which, in contrast to the kinematic molecular viscosity ν, is not a fluid property but depends strongly on the state of turbulence. The term involving k and kronecker delta, δ_{ij}, in equation (3-16) makes the expression applicable also to the normal stress (when i=j). Since the normal stress acts like pressure forces, this second part can be absorbed into the pressure gradient term when equation (3-16) is used to eliminate $\overline{u_i'u_j'}$ in the momentum equation (3-14). Given the eddy viscosity relation (3-16), the main problem is now shifted to modelling the kinematic eddy (turbulent) viscosity, ν_t.

3.5. Models for Eddy Viscosity

As mentioned in the above section, the eddy viscosity relation was conceived by presuming an analogy between the molecular motion and the turbulent motion. The turbulent eddies were thought of as lumps of fluid which, like molecules, collide and exchange momentum. The molecular viscosity is proportional to the average velocity and mean free path of the molecules. Accordingly the eddy viscosity is considered proportional to a velocity characterizing the fluctuating motion, $\hat{u}$, and to a typical length of this motion which Prandtl called the mixing length, l_m, (Prandtl, 1925). Thus,

$$\nu_t \propto \hat{u} l_m \tag{3-17}$$

Different approaches for determining the velocity scale, $\hat{u}$, and the length scale, l_m, lead to different turbulent models:

1. zero-equation model: l_m and $\hat{u}$ are specified in advance or related to known mean flow properties. For example, in Prandtl's (1925) mixing length model: $\hat{u} = l_m \left|\frac{\partial U}{\partial y}\right|$, thus $\nu_t = l_m^2 \left|\frac{\partial U}{\partial y}\right|$, where the mixing length could be determined from flow geometry such as the distance from the wall.

2. one-equation model: Kolmogorov (1942) and Prandtl (1945) proposed independently that the velocity scale, $\hat{u}$, can be represented using $k = \frac{1}{2}\overline{u_i' u_i'}$ by the

expression $\nu_t = C_\mu k^{0.5} l$. The value of k can be determined by solving the transport equation for k, while the length scale, l, has to be somehow prescribed.

3. two-equation model: there are a few two-equation models as we mentioned in the literature review. The most popular one is the k-ε model in which the turbulence length scale is expressed as: $l = k^{1.5}/\varepsilon$ so that the kinetic eddy viscosity, ν_t, can be determined from the kinetic energy of turbulence and its dissipation rate according to following relation:

$$\nu_t = C_\mu f_\mu \frac{k^2}{\varepsilon} \tag{3-18}$$

where the f_μ is the damping function (to be defined in section 3.7.3) which is equal to one in fully turbulent flow and is less than one in the near-wall region where the flow is directly affected by molecular viscosity.

In this study we choose to use k-ε model for two reasons. Firstly, this method has been extensively tested in last two decades and performs well in most test cases. In particular, the predicted limiting behavior of flow properties in the near wall region has been substantially improved with the low Reynolds number model employed in near-wall region. Secondly, the primary purpose of this project was not to develop the most sophisticated turbulence model but to be able to have a reasonably accurate model of turbulent flow that can be used in the study of wall-mass transfer and corrosion.

The question now arises as to how to determine k and ε. As mentioned before, to determine the values of k and ε, the transport equations for these quantities have to be solved. As the first step, the corresponding transport equations need to be derived. The kinetic energy (per unit mass) of turbulence is defined as:

$$k = \frac{1}{2}\overline{u_i' u_i'} = \frac{1}{2}\left(\overline{u_1'^2} + \overline{u_2'^2} + \overline{u_3'^2}\right) \tag{3-19}$$

Two methods can be used to derive the transport equation for the kinetic energy of turbulence, k. In the first method (Hinze, 1975), the transport equation for *total* kinetic energy of the flow (which includes the contribution from both mean flow and turbulence) is derived by multiplying the instantaneous momentum equation (3-2) with u_i. Similarly, the transport equation for the kinetic energy of the *mean* flow is derived by multiplying the time-averaged momentum equation (3-14) with U_i. Finally, the transport equation for kinetic energy of *turbulence* fluctuation is obtained by the subtraction of the equation for kinetic energy of *mean* flow from the equation for *total* kinetic energy of flow. In the second method (Wilcox, 1993), the Reynolds stress transport equation is derived first. The kinetic energy of turbulence can be related to the trace of the Reynolds stress as follows:

$$\tau_{ii} = -\rho\overline{u_i' u_i'} = -2\rho k \tag{3-20}$$

The transport equation for k can be derived by taking the trace of the Reynolds stress transport equation. The derivation procedures for both methods can be found from advanced textbooks about turbulence (e. g. Hinze, 1975 and Wilcox, 1993). The derived transport equation for k has the form

$$\frac{\partial k}{\partial t} + \underbrace{U_j \frac{\partial k}{\partial x_j}}_{Convection} = \underbrace{\frac{\partial}{\partial x_j}\left(\nu \frac{\partial k}{\partial x_j} - \frac{1}{2}\overline{u_i' u_i' u_j'} - \frac{\overline{p' u_j'}}{\rho} \right)}_{Diffusion} \underbrace{-\overline{u_i' u_i'} \frac{\partial U_i}{\partial x_j}}_{Production} \underbrace{-\varepsilon}_{Dissipation} \tag{3-21}$$

The sum of the turbulent transport term (triple correlation), $\frac{1}{2}\overline{u_i' u_i' u_j'}$, and pressure diffusion term, $\frac{\overline{p' u_j'}}{\rho}$, can be approximated as:

$$\frac{1}{2}\overline{u_i' u_i' u_j'} + \frac{\overline{p' u_j'}}{\rho} = -\frac{\nu_t}{\sigma_k}\frac{\partial k}{\partial x_j} \tag{3-22}$$

The dissipation rate of kinetic energy of turbulence is defined by the following correlation.

$$\varepsilon = \nu \overline{\frac{\partial u_i'}{\partial x_l}\frac{\partial u_i'}{\partial x_l}} \tag{3-23}$$

The derivation of the transport equation for the dissipation rate of kinetic energy of turbulence is much more complicated than that for the kinetic energy of turbulence and is omitted here. The idea is that the instantaneous momentum equation (3-2) is differentiated by x_l and then multiplied by $2\nu\frac{\partial u_i'}{\partial x_l}$ and finally time-averaged to yield:

$$\rho\frac{\partial \varepsilon}{\partial t}+\underbrace{\rho U_j\frac{\partial \varepsilon}{\partial x_j}}_{Convection}=\underbrace{\frac{\partial}{\partial x_j}\left(\mu\frac{\partial \varepsilon}{\partial x_j}-\mu\overline{u_j'\frac{\partial u_i'}{\partial x_l}\frac{\partial u_i'}{\partial x_l}}-2\nu\overline{\frac{\partial p'}{\partial x_l}\frac{\partial u_j'}{\partial x_l}}\right)}_{Diffusion}$$

$$\underbrace{-2\mu\left(\overline{\frac{\partial u_i'}{\partial x_l}\frac{\partial u_j'}{\partial x_l}}+\overline{\frac{\partial u_l'}{\partial x_i}\frac{\partial u_l'}{\partial x_j}}\right)\frac{\partial U_i}{\partial x_j}-2\mu\overline{u_l'\frac{\partial u_i'}{\partial x_j}}\frac{\partial^2 U_i}{\partial x_l\partial x_j}}_{Production}$$

$$\underbrace{-2\mu\overline{\frac{\partial u_i'}{\partial x_j}\frac{\partial u_i'}{\partial x_l}\frac{\partial u_j'}{\partial x_l}}-2\mu\nu\overline{\left(\frac{\partial^2 u_i'}{\partial x_j\partial x_l}\right)^2}}_{Destruction} \qquad (3\text{-}24)$$

This equation is far more complicated than the turbulent kinetic energy equation and involves several new unknown double and triple correlations of fluctuating velocity, pressure and velocity gradients. The modelled forms of this equation was given in the subsequent section.

3.6. Two Dimensional k-ε Model

We will further limit our studies to a steady state, two-dimensional turbulent pipe flow. The corresponding transport equations are elliptic. In an axisymmetric cylindrical coordinate system, the transport equations have the following form:

Continuity equation:

$$\frac{\partial}{\partial x}(\rho U)+\frac{1}{r}\frac{\partial}{\partial r}(r\rho V)=0 \qquad (3\text{-}25)$$

Momentum equation in axial direction:

$$\frac{\partial}{\partial x}\left(\rho U^2\right)+\frac{1}{r}\frac{\partial}{\partial r}\left(r\rho UV\right)=\frac{\partial}{\partial x}\left(\mu_{eff}\frac{\partial U}{\partial x}\right)+\frac{1}{r}\frac{\partial}{\partial r}\left(r\mu_{eff}\frac{\partial U}{\partial r}\right)$$
$$\frac{\partial}{\partial x}\left(\mu_{eff}\frac{\partial U}{\partial x}\right)+\frac{1}{r}\frac{\partial}{\partial r}\left(r\mu_{eff}\frac{\partial V}{\partial x}\right)-\frac{\partial P}{\partial x} \tag{3-26}$$

Momentum equation in radial direction:

$$\frac{\partial}{\partial x}\left(\rho UV\right)+\frac{1}{r}\frac{\partial}{\partial r}\left(r\rho V^2\right)=\frac{\partial}{\partial x}\left(\mu_{eff}\frac{\partial V}{\partial x}\right)+\frac{1}{r}\frac{\partial}{\partial r}\left(r\mu_{eff}\frac{\partial V}{\partial r}\right)$$
$$+\frac{\partial}{\partial x}\left(\mu_{eff}\frac{\partial U}{\partial r}\right)+\frac{1}{r}\frac{\partial}{\partial r}\left(r\mu_{eff}\frac{\partial V}{\partial r}\right)-2\mu_{eff}\frac{V}{r^2}-\frac{\partial P}{\partial r} \tag{3-27}$$

Equation for kinetic energy of turbulence:

$$\frac{\partial}{\partial x}\left(\rho Uk\right)+\frac{1}{r}\frac{\partial}{\partial r}\left(r\rho Vk\right)=\frac{\partial}{\partial x}\left[\left(\mu+\frac{\mu_t}{\sigma_k}\right)\frac{\partial k}{\partial x}\right]+\frac{1}{r}\frac{\partial}{\partial r}\left[r\left(\mu+\frac{\mu_t}{\sigma_k}\right)\frac{\partial k}{\partial r}\right]$$
$$+P_k-\rho\varepsilon \tag{3-28}$$

Equation for dissipation rate of kinetic energy of turbulence:

$$\frac{\partial}{\partial x}\left(\rho U\varepsilon\right)+\frac{1}{r}\frac{\partial}{\partial r}\left(r\rho V\varepsilon\right)=\frac{\partial}{\partial x}\left[\left(\mu+\frac{\mu_t}{\sigma_\varepsilon}\right)\frac{\partial \varepsilon}{\partial x}\right]+\frac{1}{r}\frac{\partial}{\partial r}\left[r\left(\mu+\frac{\mu_t}{\sigma_\varepsilon}\right)\frac{\partial \varepsilon}{\partial r}\right]$$
$$+\frac{\varepsilon}{k}\left(C_1 f_1 P_k-C_2 f_2\rho\varepsilon\right) \tag{3-29}$$

where μ_{eff} is the effective viscosity defined as:

$$\underbrace{\mu_{eff}}_{effective}=\underbrace{\mu}_{molecular}+\underbrace{\mu_t}_{turbulent} \tag{3-30}$$

The production of kinetic energy of turbulence, P_k, is:

$$P_k=\mu_t\left\{2\left[\left(\frac{\partial U}{\partial x}\right)^2+\left(\frac{\partial V}{\partial r}\right)^2+\left(\frac{V}{r}\right)^2\right]+\left(\frac{\partial U}{\partial r}+\frac{\partial V}{\partial x}\right)^2\right\} \tag{3-31}$$

for the eddy viscosity model adopted.

Although the equations (3-25) to (3-29) are for fluid flow in cylindrical coordinate system, they can be easily converted into those for fluid flow in Cartesian x~y coordinate system by setting:

$$\frac{\partial}{\partial r} = \frac{\partial}{\partial y}, \qquad r = 1, \qquad \frac{1}{r^2} = 0 \tag{3-32}$$

which is convenient for programming purpose in switching from one coordinate system to another one.

3.7. Boundary Conditions

Since the set of partial differential equations (3-25) to (3-29) are elliptic, it is necessary to provide boundary conditions for all variables on all boundaries of a computational domain: inlet, outlet, symmetry axis, and wall. Fully developed flow was assumed at the inlet of the computational domain. The inlet mean axial velocity profile, U, can be obtained from the empirical formula for turbulent pipe flow (Schlichting, 1979). The inlet mean radial velocity, V, is zero. The inlet profiles of turbulent kinetic energy, k, and its dissipation rate, ε, are given by the following empirical forms (Nallasamy, 1987):

$$k = 0.003\,U^2, \quad \varepsilon = C_\mu \frac{k^{1.5}}{0.015d}. \tag{3-33}$$

In order to get the fully developed profiles of U, k and ε, the above profiles for U, k, and ε are first used at the inlet to the computational domain for a straight pipe. With an

adequately long computational domain in the straight pipe, fully developed values for U, k and ε are obtained at the outlet of computational domain. These fully developed values and V=0 are then used as inlet conditions in present studies.

At the symmetry axis and outlet, zero gradient for U, V, k, ε can be set:

$$\frac{\partial U}{\partial y} = \frac{\partial V}{\partial y} = \frac{\partial k}{\partial y} = \frac{\partial \varepsilon}{\partial y} = 0 \tag{3-34}$$

On the wall we can set:

$$U = V = k = 0 \tag{3-35}$$

3.7.1. Boundary Conditions for ε on Solid Wall

Two boundary conditions for ε at solid wall have been used in previous studies:

$$\frac{\partial \varepsilon}{\partial y} = 0 \tag{3-36}$$

$$\varepsilon_w = \nu \left. \frac{\partial^2 k}{\partial y^2} \right|_{wall} \tag{3-37}$$

Many researchers have used $\frac{\partial \varepsilon}{\partial y} = 0$ as the boundary condition for ε (e. g. Cho and Goldstein, 1994; Herrero et al, 1991). This boundary condition was also used for an algebraic stress model by Hanjalic and Launder (1976). The advantage is that no turbulent kinetic energy and second order derivative are involved in boundary condition

and convergence can be easily reached. Other researchers chose $\varepsilon_w = \nu \left.\frac{\partial^2 k}{\partial y^2}\right|_{wall}$ as boundary condition for ε (e. g. Lam and Bremhorst, 1981, Nagano and Tagawa, 1990; Myong and Kasagi, 1990; Abe *et al*, 1994). This is strictly the correct boundary condition for ε at the wall as derived from the differential equation of kinetic energy of turbulence (3-28). Since equation (3-36) was still used as the boundary condition for ε by some researchers very recently (e.g. Cho and Goldstein, 1994). It is necessary to reinvestigate which boundary condition for ε performs better in satisfying the limiting behavior of the wall. The predicted limiting behavior for dimensionless turbulent kinetic energy, $k^+ (k/u_\tau^2)$, using low-Reynolds number (LRN) k-ε model was compared for two boundary conditions and plotted in Fig. 3-1. In the immediate vicinity of the wall, the turbulent kinetic energy can be expressed by the Taylor expansion series (Myong and Kasagi, 1990):

$$k^+ \equiv \frac{k}{u_\tau^2} = A^+ y^{+2} + B^+ y^{+3} + O(y^{+4}) \tag{3-38}$$

which indicates that the turbulent kinetic energy, k^+, is proportional to y^{+2} as $y^+ \to 0$. The direct numerical simulation results of Kim et al (1987) also yielded the y^{+2} behavior of k^+. Fig. 3-1 shows that the y^{+2} behavior of k^+ was predicted with the boundary condition $\varepsilon_w = \nu \left.\frac{\partial^2 k}{\partial y^2}\right|_{wall}$. Therefore, this boundary condition was adopted in this study. However, this type of boundary condition, if employed directly, may lead to instabilities during the initial stage of iterative calculations because the second-order derivative

cannot be guaranteed to provide the positive value. The same problem was also encountered by other researchers (e. g. Abe et al, 1994). In order to avoid using the second order derivative at the boundary, $\varepsilon_w = \nu \frac{2k_f}{(\delta y)^2}$ was used in this study as boundary condition for ε. The validity of the expression can be shown by expanding k_f about y in a Taylor expansion series

$$k_f = k_w + \left.\frac{\partial k}{\partial y}\right|_w (\delta y) + \frac{1}{2}\left.\frac{\partial^2 k}{\partial y^2}\right|_w (\delta y)^2 + O(\delta y)^3 \tag{3-39}$$

Since k_w=0 and $\left.\frac{\partial k}{\partial y}\right|_w = 0$ based on the definition of k and the continuity equation, the following equation can be obtained:

$$\varepsilon_w = \nu \left.\frac{\partial^2 k}{\partial y^2}\right|_w = \nu \frac{2k_f}{(\delta y)^2} \qquad \text{for } \delta y \to 0 \tag{3-40}$$

The boundary conditions for the pressure term, P, have not been introduced. In the SIMPLE algorithm used in this study, the pressure correction term, P', instead of pressure term itself was solved. The boundary condition for pressure correction term, P', will be introduced in 3.8.2.

The k-ε model is generally valid in fully turbulent flow characterized by high Reynolds number. This high-Reynolds-number turbulence model can not be applied in the near wall region without modification because of both the viscous and the wall blocking effects in near-wall region. Two basic approaches in the near-wall region have

been widely used to account for the viscous effect: the universal wall function (WF) model and the low Reynolds number (LRN) model.

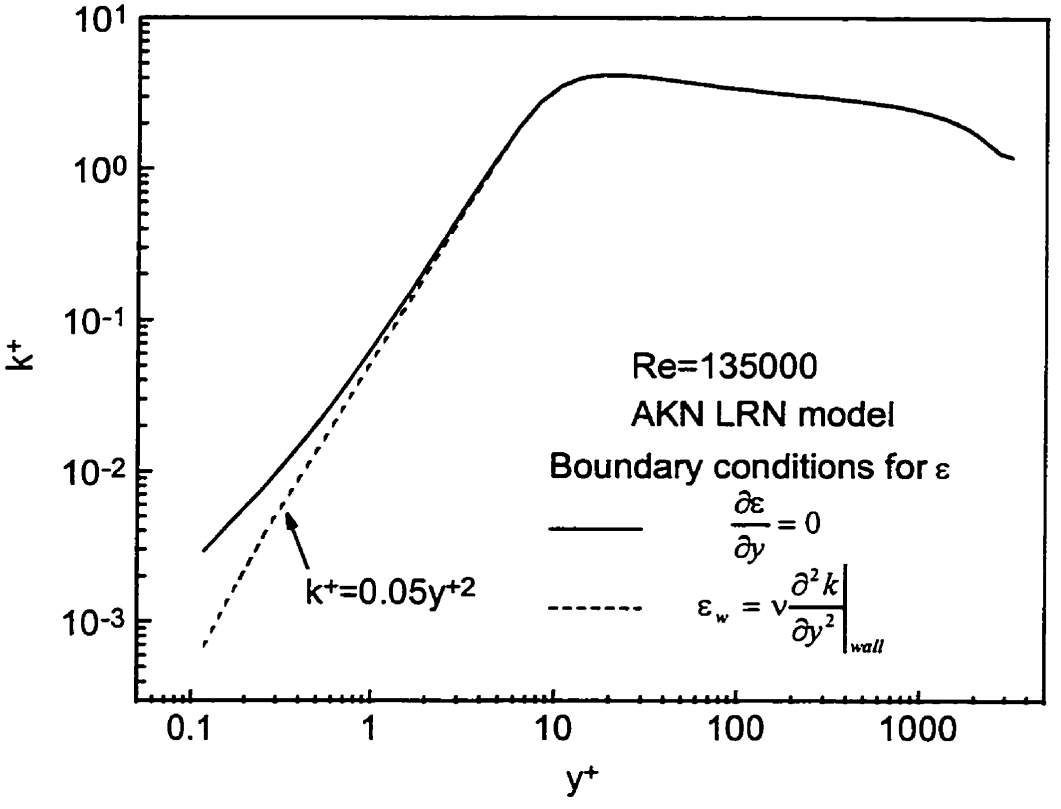

Fig. 3-1 Predicted limiting behavior of turbulent kinetic energy in near-wall region.

3.7.2. The wall function Model

In order to avoid direct modelling of turbulent flow very close to the solid wall (within the viscous sublayer), the universal law-of-the-wall can be used to connect the wall conditions to the dependent variables just outside the viscous sublayer. In the law-of-the-wall region where $30 < y^+ = \frac{y_f \rho U_\tau}{\mu} < 150$, the mean velocity profile, U^+, has a logarithmic behavior with the distance from the wall, y^+:

$$U^+ = \frac{1}{\kappa} \ln\left(y^+ E\right) \tag{3-41}$$

where $\kappa = 0.433$, and for smooth surfaces $E = 9.5$ and

$$U^+ = \frac{U}{U_\tau}, \qquad U_\tau = \left(\frac{\tau_w}{\rho}\right)^{0.5}. \tag{3-42}$$

In the law-of-wall region ($30<y^+<150$), the total shear stresses are nearly constant and the convection and diffusion of $\overline{u_i' u_j'}$ is negligible, which indicates that local equilibrium prevails. This implies that the production of turbulence is equal to its dissipation. If the first computational node is placed in the law-of-the-wall region, the turbulence kinetic energy, k, and its dissipation rate, ε, at the first node can be obtained based on the following relations:

$$k_f = \frac{\tau_w}{\rho C_\mu^{0.5}} \tag{3-43}$$

$$\varepsilon_f = \frac{C_\mu^{0.75} k_f^{1.5}}{\kappa \delta y} \tag{3-44}$$

Although the wall function approach bridges over the near wall region with a logarithmic velocity profile, the first node is typically located so that $30<y^+<150$, which misses important features of the mass transfer sublayer, the thickness of which is an order of magnitude smaller than the thickness of the hydrodynamic viscous sublayer for aqueous flow at high Schmidt numbers (Levich, 1962). Hence it is not appropriate to use the wall function approach in the case of modelling mass transfer in turbulent aqueous flow. The low-Reynolds number approach (to be introduced in the following section), which enables the application of the k-ε model through the viscous sublayer down to the wall, should be used in the case of modelling mass transfer in turbulent aqueous flow.

3.7.3. Low Reynolds Number Model

When the wall is approached, the local turbulent Reynolds number decreases and the molecular viscosity becomes important in the balance of turbulent kinetic energy and its dissipation. The low-Reynolds number (LRN) turbulence model uses the empirical function f_μ, f_1 and f_2 (also called damping functions) to account for this wall proximity effect by modifying the original high Reynolds number k-ε model. The low-Reynolds number model was originally proposed by Jones and Launder (1972 and 1973). Since then many versions have been proposed (e. g. Launder and Sharma, 1974; Lam and Bremhorst, 1981; Myong and Kasagi, 1990; Nagano and Tagawa, 1990, Herrero et al, 1991, Abe et al, 1994; Cho and Goldstein, 1994). In a review article, Patel et al (1985) have compared seven different low-Reynolds number models developed before 1985 and showed that the model of Lam and Bremhorst (1981) was one of the successful models

at that time based on experimental data. However, it was found that the Lam and Bremhorst model gives the incorrect near-wall limiting behavior of the Reynolds stress. To accurately predict mass/heat transfer in high Schmidt or Prandtl number flows, it is necessary to reproduce the near-wall limiting behavior of the turbulent properties. Since then, more low-Reynolds number models have been proposed to give an accurate prediction of the near-wall limiting behavior. Among these models, the model developed by Nagano and Tagawa (1990) (hereinafter referred to as the NT model) can reproduce the near-wall limiting behavior and provides accurate predictions for attached turbulent flows, such as pipe flow, that are required for accurate prediction of wall mass transfer. More recently, a modification of the NT model has been proposed by Abe, Kondoh and Nagano (hereinafter referred to as the AKN model), in which the Kolmogorov velocity scale $u_\varepsilon \equiv (\nu\varepsilon)^{1/4}$, instead of the friction velocity u_τ, is used to account for near-wall and low Reynolds number effects in both attached and separated flows. In the present study, the two models were compared, and the AKN model was selected for subsequent calculations. The turbulence model functions f_μ, f_1 and f_2, which are responsible for the modification of turbulent field in the near-wall region, as well as the constants for the both models are given in Table 1.

Table 1. Constants and functions in the NT and AKN models

a) NT model

c_μ	$c_{\varepsilon 1}$	$c_{\varepsilon 2}$	σ_k	σ_ε
0.09	1.45	1.9	1.4	1.3
$f_\mu = \left[1-\exp\left(-\frac{y^+}{26}\right)\right]^2\left[1+\frac{4.1}{\mathrm{Re}_t^{0.75}}\right]$				
$f_1 = 1$				
$f_2 = \left[1-0.3\exp\left(-\left(\frac{\mathrm{Re}_t}{6.5}\right)^2\right)\right]\left[1-\exp\left(-\frac{y^+}{6}\right)\right]^2$				

b) AKN model

c_μ	$c_{\varepsilon 1}$	$c_{\varepsilon 2}$	σ_k	σ_ε
0.09	1.5	1.9	1.4	1.4
$f_\mu = \left[1-\exp\left(-\frac{y^*}{14}\right)\right]^2\left[1+\frac{5}{\mathrm{Re}_t^{0.75}}\exp\left\{-\left(\frac{\mathrm{Re}_t}{200}\right)^2\right\}\right]$				
$f_1 = 1$				
$f_2 = \left[1-0.3\exp\left(-\left(\frac{\mathrm{Re}_t}{6.5}\right)^2\right)\right]\left[1-\exp\left(-\frac{y^*}{3.1}\right)\right]^2$				

3.8. Solutions of the Differential equations

The solution of a partial differential equation can be divided into two steps:

1). Discretization of the partial differential equations;

2). Solution of the resulting algebraic equations.

3.8.1. Discretization of the Partial Differential Equation

The numerical method used in this study is based on the control volume approach for discretization of the partial differential equations as proposed by Patankar (1980). The computational domain is divided into a number of control volumes each one containing only one grid point. The partial differential equations are integrated over each control volume. Linear or other types of profiles expressing the variation of a property between the grid points are used to evaluate the required integral. In this manner, the resulting discretization equation expresses the conservation principle for quantities such as mass or momentum over the finite control volume, just as the differential equation expresses it for the infinitesimal volume. In this way, the formulation is straightforward.

For ease of explanation, the discretization procedure of the partial differential equation is discussed only for Cartesian coordinates. A typical control volume for an arbitrary grid point is shown in Fig. 3-2. For grid point **P**, points **W** and **E** (denoting west and east sides) are its x-direction neighbors, while **N** and **S** (standing for north and

south sides) are the y-direction neighbors. The control volume around **P** is shown by dashed lines. The letters *w*, *e*, *s*, and *n* indicate the faces of control volume on the west, east, south, and north sides; Δx and Δy are the width and height of the control volume, while unit thickness is assumed in third direction.

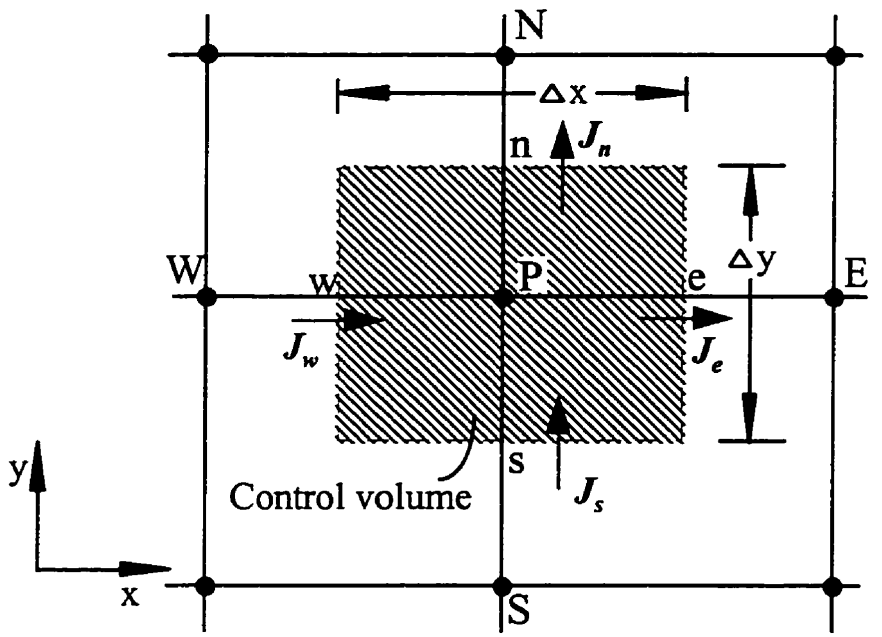

Fig. 3-2 A typical control volume in the two dimensional computational domain.

The general form of the partial differential equation for a Cartesian coordinate system is

$$\frac{\partial}{\partial x}(\rho U\Phi)+\frac{\partial}{\partial y}(\rho V\Phi)=\frac{\partial}{\partial x}\left(\Gamma_\Phi\frac{\partial\Phi}{\partial x}\right)+\frac{\partial}{\partial y}\left(\Gamma_\Phi\frac{\partial\Phi}{\partial y}\right)+S_\Phi \tag{3-45}$$

where the left hand side (LHS) of equation (3-45) denotes the convective terms. The first two terms of right hand side (RHS) are diffusion terms and the third term is a source term which contains all other transports including production and dissipation of Φ.

Equation (3-45) can be rewritten as

$$\frac{\partial}{\partial x}\left(\rho U\Phi-\Gamma_\Phi\frac{\partial\Phi}{\partial x}\right)+\frac{\partial}{\partial y}\left(\rho V\Phi-\Gamma_\Phi\frac{\partial\Phi}{\partial y}\right)=S_\Phi \tag{3-46}$$

If we define

$$J_x\equiv\rho U\Phi-\Gamma_\Phi\frac{\partial\Phi}{\partial x},\quad J_y\equiv\rho V\Phi-\Gamma_\Phi\frac{\partial\Phi}{\partial y} \tag{3-47}$$

the equation (3-47) can be rewritten as

$$\frac{\partial J_x}{\partial x}+\frac{\partial J_y}{\partial y}=S_\Phi \tag{3-48}$$

Integrating equation (3-48) over the control volume shown in Fig. 3-2 gives

$$J_e-J_w+J_s-J_n=S_\Phi\Delta x\Delta y \tag{3-49}$$

As mentioned earlier, the source term, S_Φ, includes all modes of transport except convection and diffusion. It is expected that the source term is usually significant compared to convection and diffusion terms. The source term itself is also a function of Φ and its derivatives, which makes equation (3-45) nonlinear and complicated for

numerical solution. To overcome this problem, an effective way is to linearize the source term as suggested by Patankar (1980):

$$S_\Phi = S_C + S_P \Phi \tag{3-50}$$

where S_C and S_P are constants. The problem now arises as how to transform a given expression for S_Φ into S_C and $S_P \Phi$. Patankar (1980) has provided a few basic rules to be followed (e. g. S_P must be nonpositive) in order to ensure a stable and convergent solution procedure. Now with expression (3-50) for S_Φ, equation (3-49) becomes

$$J_e - J_w + J_n - J_s = \left(S_c + S_p \Phi\right)\Delta x \Delta y \tag{3-51}$$

We return to the general form of the transport equation (3-45). If we set $\Phi=1$ and $S_\Phi=0$, the equation becomes the continuity equation:

$$\frac{\partial}{\partial x}(\rho U) + \frac{\partial}{\partial y}(\rho V) = 0 \tag{3-52}$$

In a similar manner, the continuity equation can be integrated over the control volume (see Fig. 3-2) and the result is as follows:

$$(\rho U)_e \Delta y - (\rho U)_w \Delta y + (\rho V)_n \Delta x - (\rho V)_s \Delta x = 0 \tag{3-53}$$

The above equation can be rewritten as:

$$F_e - F_w + F_n - F_s = 0 \tag{3-54}$$

where

$$F_e = (\rho U)_e \Delta y \tag{3-55}$$

$$F_w = (\rho U)_w \Delta y \tag{3-56}$$

$$F_n = (\rho V)_n \Delta x \tag{3-57}$$

$$F_s = (\rho V)_s \Delta x \tag{3-58}$$

If we multiply equation (3-54) by Φ_P and subtract it from equation (3-51), we obtain

$$(J_e - F_e\Phi_P) - (J_w - F_w\Phi_P) + (J_n - F_n\Phi_P) - (J_s - F_s\Phi_P) = (S_C + S_P\Phi_P)\Delta x\Delta y \tag{3-59}$$

where Φ_P is any property at grid point **P** in Fig. 3-2. Patankar (1980) provides the following two relations to express $J - F\Phi$:

$$J - F\Phi_i = \mathrm{A}(\Phi_i - \Phi_{i+1}) \tag{3-60}$$

$$J - F\Phi_{i+1} = \mathrm{B}(\Phi_i - \Phi_{i+1}) \tag{3-61}$$

Using these two relations in equation (3-59), we can obtain, after rearrangement, the two-dimensional discretization equation as follows:

$$a_P\Phi_P = a_E\Phi_E + a_W\Phi_W + a_N\Phi_N + a_S\Phi_S + S_C\Delta x\Delta y \tag{3-62}$$

where

$$a_P = a_E + a_W + a_N + a_S - S_P\Delta x\Delta y \tag{3-63}$$

The coefficients a_E, a_W, a_N, and a_S, representing the convection and diffusion influence on the four faces of the control volume, are affected by the interpolation functions which can transform the equation (3-62) into central difference, upwind, hybrid, power law and other discretization schemes. The hybrid scheme has been used in this study. The hybrid

scheme is a combination of the central difference scheme and upwind scheme. It is identical to the central difference scheme for the Peclet-number range $-2 \le P_e \le 2$. Out of this range it reduces to the upwind scheme in which the diffusion has been set to zero. The coefficients a_E, a_W, a_N, and a_S must also be positive as reported by Patankar (1980).

Finally, the discretization equation (3-62) is written for each variable, Φ, on each control volume surrounding each grid point in the computational domain. The solution of the resulting set of algebraic equations will be introduced in section 3.8.2.

3.8.1.1. Special Treatment for Momentum Equation

The discretization procedure for the general differential equation described above is applicable to the cases where the velocity profiles are given. A difficulty is encountered when this method is used to calculate the velocity profiles. This difficulty is caused by the unknown pressure field. The pressure gradient is included in the source term and there is no obvious equation to obtain the pressure field. On the other hand, the pressure field is indirectly specified via the continuity equation. That is, only with the correct pressure field, will velocity profiles obtained from the momentum equations satisfy the continuity equation. Thus, the main task is to convert the indirect information in the continuity equation into a direct algorithm for the pressure field. But two related difficulties must be resolved before we begin this task.

One of the difficulties encountered is the representation of the pressure gradient term in the momentum equation. When pressure gradient term, $-\frac{dP}{dx}$ for example, for

the one-dimensional situation as shown in Fig. 3-3 is integrated over the control volume, the resulting discrete form of the pressure difference is $P_w - P_e$, which is the net pressure force exerted on the control volume. When the pressure difference, $P_w - P_e$, is expressed in terms of the grid-point pressure value, the pressure drop becomes the pressure difference between two alternate grid points, not between adjacent grid points. This will cause a so-called "zig-zag" pressure field as shown in Fig. 3-4(a). Such a zig-zag field, of course, can not be regarded as realistic, but is interpreted as a uniform pressure by the momentum equation because the alternate pressure values are equal everywhere. A similar kind of problem arises when we try to represent the continuity in discrete form. The discretized continuity equation demands the equality of velocities at alternate grid points and not at adjacent ones. A consequence is that unrealistic velocities fields, as shown in Fig. 3-4(b), can satisfy the continuity equation.

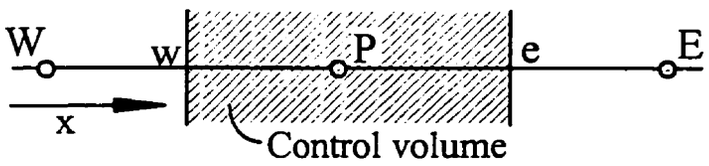

Fig. 3-3 Three-grid cluster.

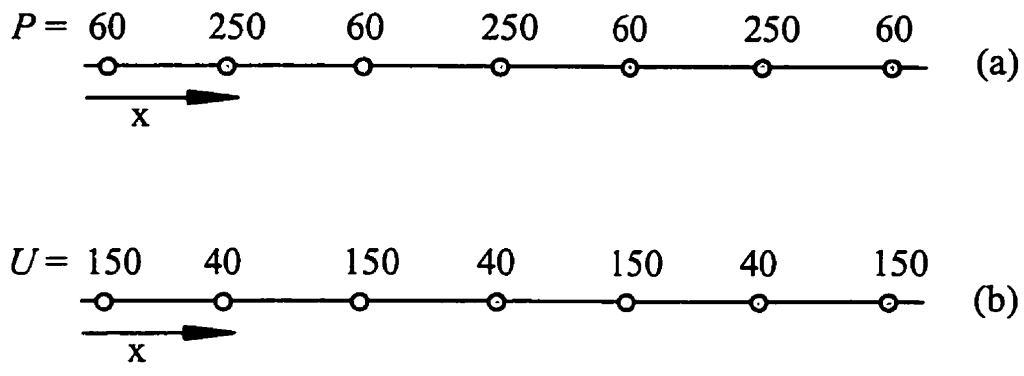

Fig. 3-4 Zig-zag pressure field (a) and wavy velocity field (b).

A remedy to this kind of problem is to use a staggered grid system. In the case of calculation of velocity components, we use control volumes that are different from the ones used for the calculation of other variables (e. g. pressure, turbulence kinetic energy and its dissipation rate). The staggered grid system is arranged so that the velocity components are calculated for control volumes which are located on the faces of the scalar control volume around grid point P (hereafter called as the scalar control volume). For example, the velocity component in the x-direction, U, is calculated at the faces that are normal to the x direction, and the control volume for U is displaced one half control volume from the main control volume in x-direction (Fig. 3-5). The velocity component in y-direction, V, is calculated at faces that are normal to the y-direction and the control volume for V is displaced one half control volume from the main one in y-direction (Fig. 3-6).

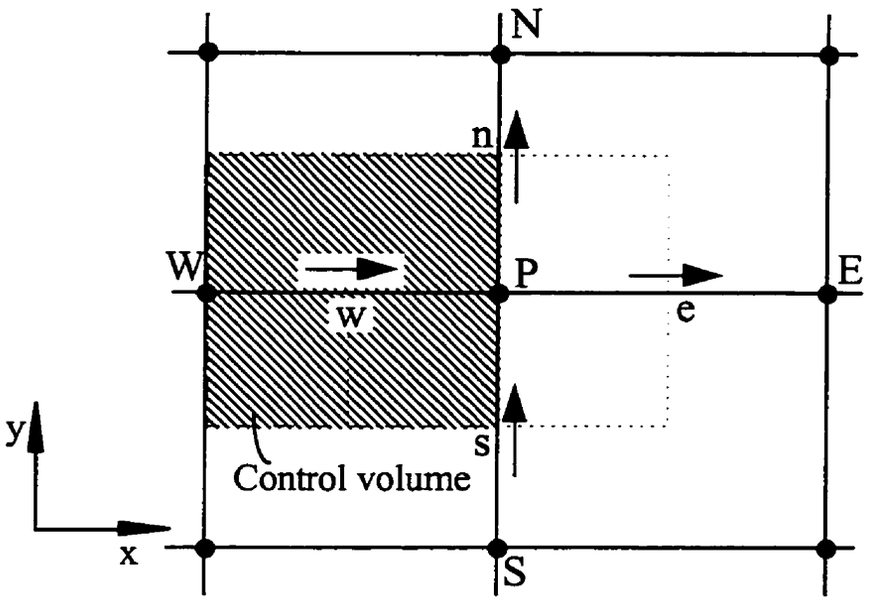

Fig. 3-5 Control volume for *U*.

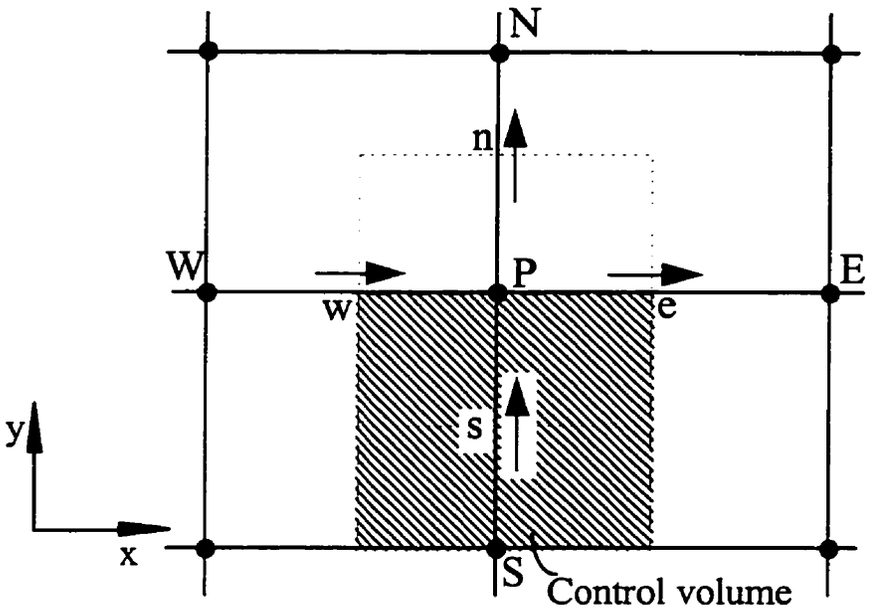

Fig. 3-6 Control volume for *V*.

The advantages of using a staggered grid system are obvious. First of all, the pressure difference between any two adjacent grid points naturally becomes the driving force for the velocity component located between the two grid points. The zig-zag pressure field shown in Fig. 3-4(a) is no longer felt as a uniform pressure field and could not become a possible solution. Another advantage is that if the continuity equation is integrated over the main control volume, the discretized form will contain the velocity difference of adjacent velocity components, which will prevent a wavy velocity field. It seems that the difficulties described earlier could be attributed to the practice of

calculating all variables at one single grid system. With a staggered grid system, these difficulties are completely eliminated.

Now we return to our main problem--how to link the continuity equation to the momentum equation via the pressure term. With staggered grid, the discretized equation for U can be expressed as:

$$a_w U_w = \sum a_{nb} U_{nb} + b + (P_W - P_P)\Delta y \tag{3-64}$$

where the term $(P_W - P_P)\Delta y$ is the pressure force acting on the control volume for U (see Fig. 3-5). The discretized momentum equation (3-64) can not be solved unless the pressure field is given or somehow estimated. If a guessed pressure field is given, the velocity field solved based on the guessed pressure field will be imperfect and will not satisfy the continuity equation. We have to somehow correct the guessed pressure field and the velocity field during the iterative calculation so that the calculated velocity field will gradually approach the real velocity field. Patankar (1980) introduced the concept of *pressure correction*, P', and *velocity correction*, U' which are defined as follows:

$$P = P^* + P' \tag{3-65}$$

$$U = U^* + U' \tag{3-66}$$

where P^* and U^* are guessed pressure and velocity fields, while P and U are real pressure and velocity fields. In order to show how the velocity correction responses to pressure correction, Patankar (1980) proposed following relation:

$$U'_w = d_w (P'_W - P'_P)\,. \tag{3-67}$$

where d_w is a coefficient yet to be determined. With this relation, the velocity correction formula (3-66) becomes

$$U_w = U_w^* + d_w(P'_W - P'_P). \tag{3-68}$$

This shows how the guessed velocity, U_w^*, is to be corrected in response to the pressure corrections to produce U_w. Recall that the continuity equation in two-dimensional form is

$$\frac{\partial}{\partial x}(\rho U) + \frac{\partial}{\partial y}(\rho V) = 0 \tag{3-52}$$

If we integrate the equation (3-52) over the main control volume for grid point P (See Fig. 3-2) and then substitute the expressions given by the velocity correction formulas (such as equation (3-68)) for all velocity components, we obtain, after rearrangement, the following discretization equation for the pressure-correction, P':

$$a_P P'_P = a_E P'_E + a_W P'_W + a_N P'_N + a_S P'_S + b \tag{3-69}$$

As we see that the pressure correction term has been introduced into the continuity equation and in this way the continuity equation is linked to the momentum equation. The modified continuity equation is called the pressure correction equation (equation (3-69)). The method used above is called the SIMPLE (Semi-Implicit Method for Pressure Linked Equation) algorithm which is proposed by Patankar and Spalding (Patankar and Spalding, 1972; Patankar, 1980). The execution of the algorithm is as follows:

1. Guess the pressure field, P^*.
2. Solve momentum equations, such as equation (3-64), for U^* and V^*.
3. Solve the P' equation and calculate P from equation (3-65).

4. Calculate the corrected U and V using the velocity-correction formulas, such as equation (3-68).
5. Solve the discretization equations for other variables (such as k, ε, et al).
6. Treat P as a new guessed pressure P^*, return to step 2 and repeat the whole procedure until a converged solution is achieved.

The determination of the boundary conditions for the pressure correction equation can be based on the definition of the pressure correction itself. Recall that the boundary conditions for velocity components in this study are known or given at all boundaries (inlet, outlet, symmetry axis and wall). The values of velocity components at these boundaries will not need to be corrected in terms of equation (3-68). Therefore, the boundary conditions at all boundaries for the pressure correction, P', will be

$$\frac{\partial P'}{\partial x} = 0, \qquad \frac{\partial P'}{\partial y} = 0 \tag{3-70}$$

3.8.2. Solution of Discretized Equations

We have obtained the two-dimensional algebraic equations for each variable involved in this study through the discretization procedure discussed in the previous section. The set of algebraic equations contains $n_i \times n_j$ equations for each variable, where n_i and n_j are the number of grid point in x and y directions for the flow domain. Application of the direct methods, such as Gauss-Jordan elimination method, to solve

such a set of equation is impractical especially when a large number of grid points are involved.

The alternative is to use an iterative method. There are various formulations of iterative method which can be divided into two categories: point iterative method and line iterative method. The point iterative method, such as point Gauss-Seidel iterative method, involves only one unknown in a formulation, while line iterative method involves more than one unknown (usually three unknowns) in a formulation. The major disadvantage for point iterative method is that the convergence is too slow. The reason is that the boundary-condition information is transmitted at a rate of one grid interval per iteration. In this study we will use the line Gauss-Seidel iteration method (Hoffmann, 1989). This line-by-line scheme can be easily visualized with reference to Fig. 3-7. The discrete equations for the grid points along a chosen line in y direction was considered. Since the variables at the grid points along the two neighboring lines are known values at $k+1$ iteration level or at k iteration level, the equations for the grid points along the chosen line would look like one-dimensional equation. The equation for each grid point has following form:

$$-a_S\Phi_S^{k+1} + a_P\Phi_P^{k+1} - a_N\Phi_N^{k+1} = a_W\Phi_W^{k+1} + a_E\Phi_E^{k} + b \tag{3-71}$$

This equation, applied to all j at a constant i, results in a system of linear equations which has a tridiagonal matrix coefficient and thus can be solved using the TDMA (TriDiagonal Matrix Algorithm). In this study, we chose to use the line Gauss-Seidel iteration method in the y direction since the value of the dependent variables changes

more rapidly in the y direction and faster convergence can be achieved. Besides, the sweep direction is also important. A left-to-right sweep was employed in this study since a sweep from upstream to downstream would produce much faster convergence than a sweep against the stream.

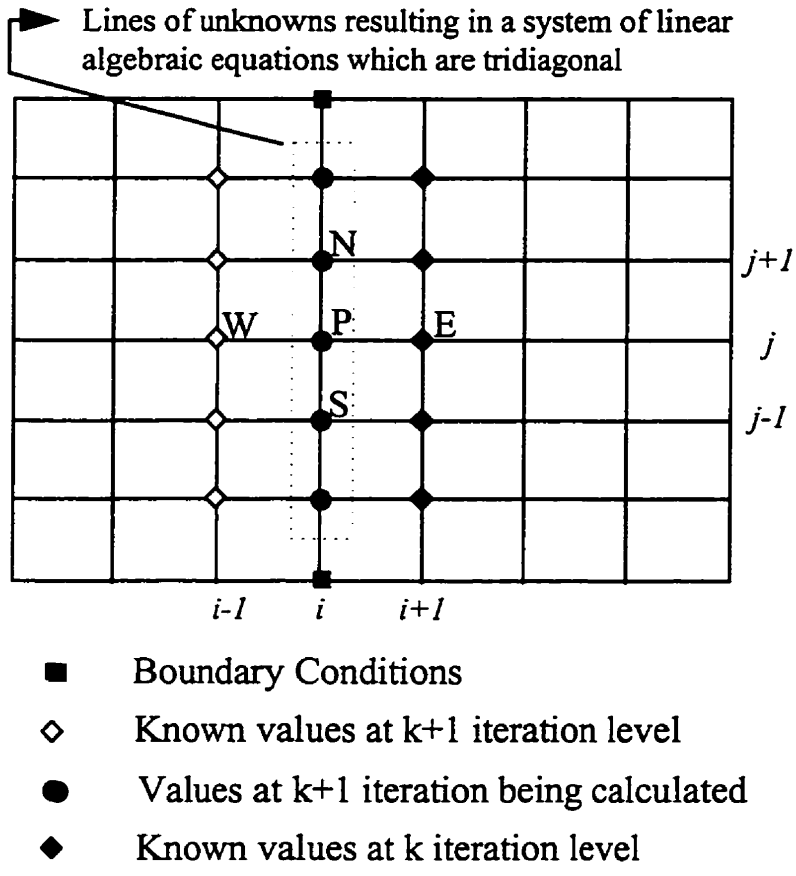

Fig. 3-7 Grid points employed in the line Gauss-Seidel iteration method

The overrelaxation and underrelaxation methods have been extensively used in the iterative solution of the algebraic equation to speed up or slow down the change of variables. In this study, the underrelaxation has been used to ensure the stable and convergent solution since the equations to be solved contain strongly nonlinear convective terms. The general formula for introducing overelaxation and underrelaxation is as follows:

$$\Phi^{k+1^*} = \Phi^k + \alpha(\Phi^{k+1} - \Phi^k) \tag{3-72}$$

where Φ^{k+1} and Φ^k are the values of variable Φ at $k+1$ and k level iteration. α is relaxation factor which is underrelaxation when $0<\alpha<1$ or overrelaxation when $\alpha>1$. Φ^{k+1^*} is new value of variable Φ after relaxation. Based on the discrete equation, such as equation (3-62), Φ^{k+1}, at the grid point P, can be expressed as

$$\Phi_P^{k+1} = \frac{\sum a_{nb}\Phi_{nb} + S_C}{a_P} \tag{3-73}$$

Substitute equation (3-73) to equation (3-72) and rearrange equation (3-72), we obtain:

$$\frac{a_P}{\alpha}\Phi_P^{k+1^*} = \sum a_{nb}\Phi_{nb} + S_C + (1-\alpha)\frac{a_P}{\alpha}\Phi_P^k \tag{3-74}$$

This equation shows that it is the coefficients a_P and S_C, not variable Φ, that have been underrelaxed. This underrelaxation method was proposed by Patankar (1980) and has been used in this study.

Another problem is that how to declare the achievement of a convergent solution. In this study, we chose to check the balance of each variable for each control volume in

every iteration. The error or residual for each variable for each control volume in every iteration is defined as:

$$R_\Phi = a_N\Phi_N + a_S\Phi_S + a_W\Phi_W + a_E\Phi_E + S_C - a_P\Phi_P \tag{3-75}$$

where the coefficients a_i and S_C are updated values while the variables Φ_i are the values calculated from previous iteration. When convergence is achieved, the residual, R_Φ, should be equation to zero. In practice, the residual, R_Φ, is required to be smaller than a given value. In this study, we have chosen to calculate the sum of the residuals of all control volumes for each variable in the computational domain and then to normalize it. To declare the convergence of the solution, this normalized value should be smaller than 0.001. The normalization is done for continuity equation with the inlet fluid flow rate and for the momentum equation with the inlet momentum rate. Besides, one or more locations in the computational domain are checked to ensure the smooth change of any variable during the iteration procedure. As final convergence is achieved, the changes of the variables from iteration to iteration in whole computational domain should be negligible.

3.9. Overall Algorithm

The overall algorithm used for this study is based on the TEACH code proposed by Patankar and Spalding (1972). This code has been modified to include low-Reynolds-number model (Abe et at, 1994) and mass transfer model for calculating the wall mass

transfer rate of reactants and corrosion products concerned. The block diagram of the overall algorithm is shown in Fig. 3-8. The computation steps are outlined as follows:

1. Input parameters. Set grid parameters and program control parameters. Set inlet boundary values. Set turbulence constants. Call subroutine INIT to calculate geometry quantities; set all variables to zero; and then set guessed pressure field. Calculate initial variable fields.
2. Call PROPS to set initial flow properties (such as effective viscosity and diffusivity, local turbulent Reynolds number, the damping function).
3. Call CALCU to calculate momentum equation in axial direction.
4. Call CALCV to calculate momentum equation in radial direction.
5. Call CALCP to calculate modified continuity equation (pressure correction equation).
6. Call CALCTE to calculate equation for kinetic energy of turbulence.
7. Call CALCED to calculate equation for dissipation rate of turbulent kinetic energy.
8. Call CALCMH to calculate transport equation for chemical species, such as O_2, Fe^{++}, Cu^{++}, H^+, OH^-).
9. Call PROPS to calculate updated flow properties (such as effective viscosity, μ_{eff}, effective diffusivity, D_{eff}, local turbulent Reynolds number, Re_n and damping function, f_μ).
10. Check convergence. If a convergent solution is not achieved, return to step 3.
11. If a convergent solution is achieved, calculate final results for mass transfer rate, wall shear stress, near wall turbulence parameters and other relevant parameters and print out all these results.

The code structures for subroutines CALCU, CALCV, CALCP, CALCTE, CALCED and CALCMH are in a similar pattern. The main steps for such a code can be summarized as follows:

1. Calculation of the area and volume for each control volume in the flow domain.
2. Calculation of the convection, diffusion and source term coefficients.
3. Assembly of the main coefficients: a_E, a_W, a_N, a_S, S_C and S_P.
4. Introduction of the boundary conditions at the wall, symmetry axis and outlet. This was done by calling subroutine PROMOD.
5. Computation of the coefficient a_p and sum of absolute value of the Residual.
6. Uses of line Gauss-Seidel iteration algorithm to perform left-to-right sweep and of TDMA method to solve the resulting set of algebraic equations at each sweep step. These were done by calling subroutine LISOLV.

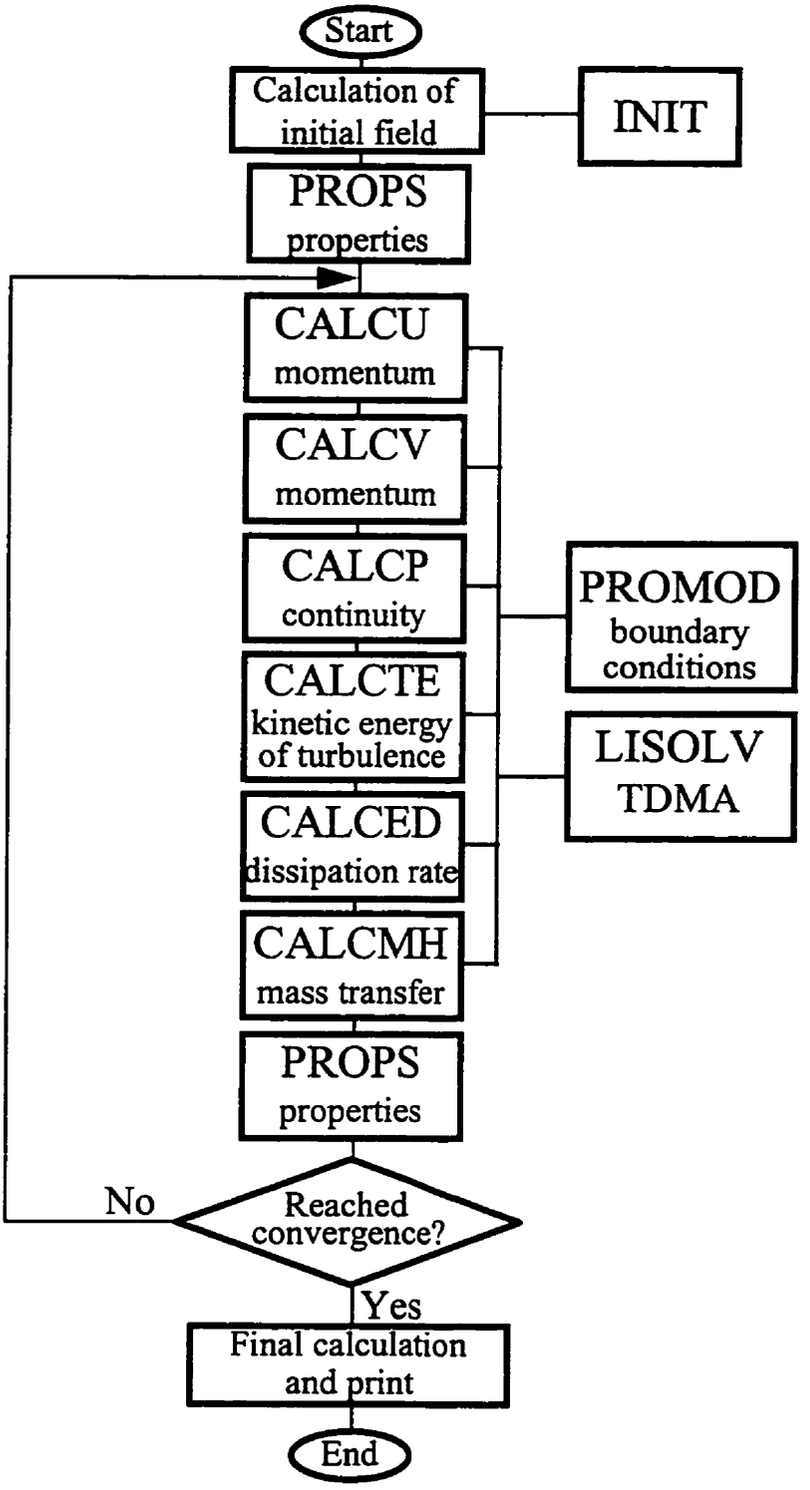

Fig. 3-8 The block diagram of the algorithm.

4. Model of Mass Transfer

The mass transfer model was used to calculate the wall-mass-transfer rate of the chemical species concerned in this study (such as O_2, Fe^{2+}, Cu^{2+}, OH^- and H^+). The model includes two parts: Calculation of the species concentration distribution and calculation of the mass transfer coefficient.

4.1. Time-Averaged Transport Equation

In analog to the treatment of the instantaneous velocity in section 3.3, the instantaneous species concentration can be replaced by the sum of the mean concentration and the fluctuating concentration:

$$\tilde{c} = c + c' \tag{4-1}$$

The instantaneous transport equation for species concentration can be expressed as

$$u_j \frac{\partial \tilde{c}}{\partial x_j} = \frac{\partial}{\partial x_j}\left(D \frac{\partial \tilde{c}}{\partial x_j} \right) \tag{4-2}$$

The terms on the left hand side are convection terms while the terms on the right hand side are diffusion terms. If we substitute equation (4-1) into equation (4-2) and then take time-averaging process on equation (4-2), we obtain

$$U_j \frac{\partial c}{\partial x_j} = \frac{\partial}{\partial x_j}\left(D\frac{\partial c}{\partial x_j} - \overline{c'u_j'} \right) \tag{4-3}$$

The term $-\overline{c'u_j'}$ is called the turbulent mass flux and has to be related to c or its gradient if equation (4-3) is to be solved. By analogy with Fick's law of diffusion, we can write

$$-\overline{u_j'c'} = D_t \frac{\partial c}{\partial x_j} \tag{4-4}$$

where D_t is turbulent or eddy diffusivity of mass and, like the eddy viscosity, is not a fluid property but depends on the state of turbulence. In fact, the Reynolds analogy between mass transport and momentum transport suggests that D_t is closely related to μ_t :

$$D_t = \frac{\mu_t}{\rho\sigma_m} \tag{4-5}$$

where σ_m is called turbulent Prandtl Schmidt number. It is defined as the ratio of the eddy diffusivity for momentum transfer to the eddy diffusivity for heat/mass transfer. Based on the Reynolds analogy, the turbulent Prandtl Schmidt number (σ_m) is equal to one. The experimental data for air indicate that the σ_m is close to one (Kays and Crawford, 1980). In this study the σ_m was set at 0.9 according to Kays and Crawford (1980). With equations (4-5) and (4-3), the two dimensional time-averaged mass transport equation in a cylindrical coordinate system can be expressed as

$$\frac{\partial}{\partial x}(Uc)+\frac{1}{r}\frac{\partial}{\partial r}(rVc)=\frac{\partial}{\partial x}\left(D_{eff}\frac{\partial c}{\partial x}\right)+\frac{1}{r}\frac{\partial}{\partial r}\left(rD_{eff}\frac{\partial c}{\partial r}\right) \tag{4-6}$$

The D_{eff} is called effective diffusivity. In a similar manner as for μ_{eff} in equation (3-30), the effective diffusivity, D_{eff}, is defined as the sum of molecular diffusivity and turbulent diffusivity and is expressed as

$$\underbrace{D_{eff}}_{effective} = \underbrace{\frac{\mu}{\rho Sc}}_{molecular} + \underbrace{\frac{\mu_t}{\rho\sigma_m}}_{turbulent} \tag{4-7}$$

4.1.1. Boundary Conditions

The inlet conditions for dissolved species are different depending on the two specific cases concerned. In the case that the mass-transfer-entry-length effect on mass transfer section or working electrode is taken into account, a uniform or flat species concentration profile (normalized concentration c=1) is set at the inlet of computational domain and remain uniform until the mass transfer section or working electrode is reached. If the entry effect is not taken into account, a fully developed species concentration profile is used at the inlet to the computational domain. Zero gradients can be set at the symmetrical axis and outlet. At the wall, the normalized species concentration, c, are also different depending on following various situations:

1. $c_w = 0$ on mass transfer section or working electrode.
2. $c_w = 1$ on non-mass transfer section or non-metallic spacer.

Above boundary conditions have been applied to all species concerned in this study for the calculation of the concentration profiles. Although we may aware that in practice the concentration of corrosion product (such as Fe^{2+}, Cu^{2+}, OH^-) at the corroding metal surface is higher than that in the bulk solution, instead of zero, the boundary conditions given above are still valid. The purpose of calculating the species concentration profile in this study is to calculate the wall mass transfer coefficient in pipeline flow. The experimental results of Berger and Hau (1977), and Son and Hanratty (1967) have showed that the mass transfer coefficient is affected only by the Reynolds number (*Re*) and the Schmidt number ($Sc = \nu/D$) in fully developed pipe flow. It is also affected by the distance from the mass transfer entrance (x/d) in addition to the Reynolds number and Schmidt number in the mass transfer entrance length. Therefore, the wall mass transfer coefficient can be calculated from any concentration distribution which is solved from given Re, Sc (in fully developed flow), and x/d (in mass transfer entrance region).

In the case of the corroding metal surface (e. g. working electrode) on which at least one anodic dissolution reaction and one cathodic reduction reaction will occur simultaneously, the electromigration effects are not taken into account since only uniform (or general) corrosion is considered where the metal surface is covered with a multitude of microscopic corrosion cells, with the anodic and cathodic sites intimately mixed and in statistical change. In such cases there will be no concentration variations with respect to position on the metal surface but only with respect to the bulk solution and these will be governed solely by diffusional and convective mass transport

considerations (Postlethwaite and Sharp, 1969). As pointed out by Newman (1974) and Bianchi et al (1978) in general corrosion there is no separation between anodic and cathodic area, so that electric transport processes need not be considered.

4.2. Mass Transfer Coefficient

Based on Fick's law of diffusion, the mass flux toward the pipe wall is expressed as

$$K(c_b - c_w) = D\left.\frac{\partial c}{\partial y}\right|_w \tag{4-8}$$

As mentioned earlier, the application of the low Reynolds number model enables the calculation of species concentration profiles all the way to the wall. If the first node is placed within the diffusion controlled mass transfer sublayer within which the concentration profile is linear, the local mass transfer coefficient, K, can be calculated by rewriting equation (4-8):

$$K = \frac{D(c_f - c_w)}{(\delta y)(c_b - c_w)} \tag{4-9}$$

The mean mass transfer coefficients are estimated by integrating local values over a certain length of mass transfer section.

In this study the first near-wall node has been placed at $y \leq 1\mu m$ (where $y^+ \leq 0.1$) from the wall in most of simulations. Two grid systems (91 × 41) have been used to evaluate the effects of the distance of first node from the wall on the calculation of mass

transfer coefficients (see Fig. 4-1). The results indicate that the concentration profile is approximately linear within diffusion controlled boundary layer ($y^+ \leq 0.1$) and equation (4-9) is suitable to estimate the first derivative of the concentration profile.

The diffusion coefficients for O_2, H^+ and OH^- are 1.8×10^{-9}, 9.34×10^{-9} and 5.23×10^{-9} m^2/sec respectively according to Cussler (1984) and Parsons (1959). The diffusion coefficients for metal ions at 25 °C can be calculated by using following equation:

$$D_i = \frac{2.662 \times 10^{-7}}{|z_i|}\lambda_i \tag{4-10}$$

Taking $\lambda_{Cu^{2+}} = 53.5$ and $\lambda_{Fe^{2+}} = 56.6$ (Parsons, 1959) gives $D_{Cu^{2+}} = 7.53 \times 10^{-10}$ m^2/sec and $D_{Fe^{2+}} = 7.12 \times 10^{-10}$ m^2/sec.

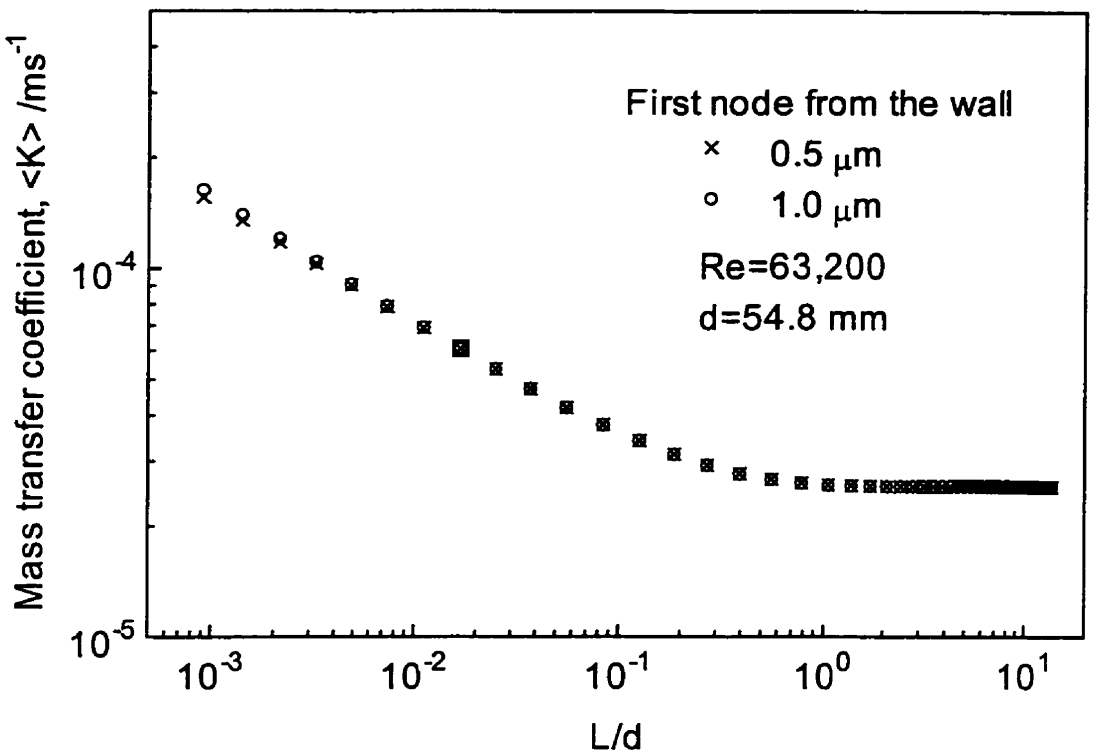

Fig. 4-1 Effect of the distance of first node from the wall on the evaluation of mass transfer coefficients.

5. Model of Corrosion

5.1. Basic Corrosion kinetics

Metallic corrosion can be defined as the destructive attack of a metal by chemical and electrochemical reaction with its environment. An overall corrosion reaction is composed of at least one anodic dissolution reaction of metal and one cathodic reduction reaction of oxidant. Since both reactions involve the transport process, a typical corrosion process can be divided into three basic steps:

1. Transport of oxidants (e.g. O_2, H^+) from bulk solution to metal/solution interface.
2. Surface electrochemical reactions during which the metal corrodes and dissolves into solution and oxidants are reduced on the corroding surface.
3. Transport of dissolved corrosion product and from metal/solution interface to bulk solution.

The corrosion rate may be controlled or affected by any one of the above steps. The first step and the third step are directly affected by the mass transfer rate of the oxidants to be

reduced on the metal surface and the dissolved corrosion product. In this study the effects of the mass transfer on the corrosion of metals throughout the mass transfer entry lengths in turbulent flow in pipes were investigated. Kinetic corrosion diagrams (E-log i) were constructed to determine the local corrosion rates for metals with a wide range of electrochemical rate constants, k_s, corroding in neutral and acidic solutions. Iron was chosen as a representative of metals, with an incomplete d-shell and a low value of k_s, and consequently i_o, whose anodic dissolution is not affected by flow in the absence of film formation (Postlethwaite et al, 1978; Postlethwaite , 1970; Lorenz and Heusler, 1987) and copper to represent metals with a complete d-shell (in the metallic state) whose anodic dissolution is flow sensitive (Postlethwaite et al, 1978; Faita et al, 1975; Bjorndahl and Nobe, 1984). Following Piontelli, Evans (1960) classified the two groups of metals as abnormal metals (*Fe, Ni, ...*) and normal metals (*Cu, Zn, ...*) with respect to their electrochemical behavior. Oxygen, hydrogen ion and water reduction are the cathodic reactions considered. In addition to corrosion rates the surface concentration of metal ions and pH along the entry length are established.

In this study, the anodic dissolution of iron and copper and cathodic reduction of oxygen, hydrogen and water were assumed to proceed on the film-free inside surface of a tubular electrode, with internal diameter of 25 mm. The Reynolds number ranged from 10^4 to 10^5. The flowing medium was aerated water at pH values of 1 and 6.

5.2. Anodic Dissolution of Iron

For the anodic dissolution of iron, the pH-dependent mechanism in acid solution proposed by Bockris et al (1961) was used:

$$Fe + H_2O \Leftrightarrow FeOH + H^+ + e^- \tag{5-1a}$$

$$FeOH \rightarrow FeOH^+ + e^- \tag{5-1b}$$

$$FeOH^+ + H^+ \Leftrightarrow Fe^{2+} + H_2O \tag{5-1c}$$

where the reaction (5-1b) is rate-determining-step.

The rate equation which takes into account the resistance to charge transfer and mass transport has been derived based on the above pH-dependent mechanism. The detailed derivation procedure is given in Appendix I. The final form of the rate equation is as follows:

$$i = i_a - i_c = i_0\left(\frac{[OH^-]_s}{[OH^-]_b}\right)^n\left[\exp\left(\frac{\alpha_a F\eta}{RT}\right) - \frac{[Fe^{2+}]_s}{[Fe^{2+}]_b}\exp\left(-\frac{\alpha_c F\eta}{RT}\right)\right] \tag{5-2}$$

where i_0 is the exchange current density based on the bulk Fe^{2+} and OH^- concentrations. The overpotential, η, is E-E_{rev}, where E_{rev} is based on the bulk Fe^{2+} concentration.

The Fe^{2+} concentration dependence of the exchange current density is:

$$\frac{\partial \log i_0}{\partial \log[Fe^{2+}]} = 0.8 \tag{5-3}$$

and the OH^- concentration dependence of exchange current density is:

$$\frac{\partial \log i_0}{\partial \log[OH^-]} = n \tag{5-4}$$

where n is pH dependent. According to Bockris et al. (1961), $n=1$ in acid solution and $n \approx 0$ in near-neutral solutions.

Since the cathodic partial is negligible at the net current densities observed in corrosion processes, because of small exchange current density, only the anodic part of the general equation is used:

$$i = i_0 \frac{[OH^-]_s^n}{[OH^-]_b^n} 10^{\frac{\eta}{b_a}} \tag{5-5}$$

where $b_a = \frac{2.303RT}{\alpha_a F}$. According to Bockris et al. (1961), $\alpha_a = 1.5$ giving b_a=0.04 V at 25°C. The exchange current density for iron dissolution, 9×10^{-4} A/m^2 at pH=3.1 and [Fe^{2+}]=9×10^{-4} mol/dm^3 (Bockris et al, 1961), was used as the reference value in this study. The bulk Fe^{2+} concentration for the present study was assumed to be 10^{-6} mol/dm^3, giving E_{rev}=*-0.617 V* at 25 °C. The calculated exchange current density at pH=1 and Fe^{2+}=10^{-6} mol/dm^3 was 3.1×10^{-8} A/m^2 and the value at pH=6 was estimated at 3.1×10^{-5} A/m^2 based on the above study.

5.3. Anodic Dissolution of Copper

The anodic dissolution reaction of copper

$$Cu \Leftrightarrow Cu^{2+} + 2e \tag{5-6}$$

can be regarded as being composed of two elementary steps:

$$Cu \rightarrow Cu^{+} + e \tag{5-7a}$$

$$Cu^{+} \rightarrow Cu^{2+} + e \tag{5-7b}$$

According to Mattsson and Bockris (1959), the second step is the rate-determining-step. In this study, it is assumed that the cuprous ions do not diffuse away from the electrode, that their concentrations reach a value such that reaction (5-7a) and (5-7b) occur at the same rate and that reaction (5-7a) is in equilibrium. The rate equation based on this mechanism is:

$$i = i_a - i_c = i_0\left[\exp\left(\frac{\alpha_a F\eta}{RT}\right) - \frac{[Cu^{2+}]_s}{[Cu^{2+}]_b}\exp\left(-\frac{\alpha_c F\eta}{RT}\right)\right] \tag{5-8}$$

In the case of copper, which has much higher i_0 values than iron, the cathodic partial is not negligible at the net anodic current densities of the magnitude found in corrosion processes and the rate equation cannot be simplified as was done for iron above.

The mass transport rate equation for Cu^{2+} is

$$i = \frac{zK_{M^{z+}}F}{(1 - t_{M^{z+}})}([Cu^{2+}]_s - [Cu^{2+}]_b) \tag{5-9}$$

Since uniform corrosion with microscopic corrosion cells was being modelled ionic transport is not a factor and $t_{M^{z+}}$=0. After eliminating $[Cu^{2+}]_s$ from equations (5-8) and

(5-9), the following current versus overpotential equation for metal dissolution was obtained:

$$i = \frac{i_0\left(10^{\frac{\eta}{b_a}} - 10^{-\frac{\eta}{b_c}}\right)}{1 + \frac{i_0}{zK_{M^{z+}}F[Cu^{2+}]_b}10^{-\frac{\eta}{b_c}}} \tag{5-10}$$

where $b_a = \frac{2.303RT}{\alpha_a F}$ and $b_c = \frac{2.303RT}{\alpha_c F}$. According to Mattsson and Bockris (1959) α_a=1.5 and α_c=0.5 giving b_a=0.04 V and b_c=0.12 V at 25°C. The reference exchange current density, i_0=32 A/m^2 at [Cu^{2+}]=0.011 mol/dm^3, and the Cu^{2+} dependence, $\frac{\partial \log i_0}{\partial \log[Cu^{2+}]} = 0.75$ (Mattsson and Bockris, 1959), was used to determine a value of i_0 =0.03 A/m^2 at [Cu^{2+}]$_s$ = 10^{-6} mol/dm^3.

5.4. Oxygen Reduction

For oxygen reduction the anodic partial is negligible, and the rate equation can be written as follows:

$$i = i_0\left\{\frac{[O_2]_s}{[O_2]_b}\exp\left(-\frac{\alpha_c F}{RT}\eta\right)\right\} \tag{5-11}$$

The metal/solution interface concentration, $[O_2]_s$, can be determined from the mass transfer equation:

$$i = zK_{O_2}F([O_2]_b - [O_2]_s) \tag{5-12}$$

After eliminating $[O_2]_s$ from equations (5-11) and (5-12), equation (5-13) was obtained:

$$\frac{1}{i}=\left(\frac{1}{i_0 10^{\frac{\eta}{b_c}}}\right)+\left(\frac{1}{i_{\lim}^{d}}\right) \tag{5-13}$$

where the cathodic Tafel slope for O_2 reduction is $b_c=\frac{2.303RT}{\alpha_c F}$. Assuming α_c=0.5 for O_2 reduction gives b_c=0.12 V at 25°C. The limiting current density for O_2 reduction is

$$i_{\lim}^{d}=4K_{O_2}F[O_2]_b \tag{5-14}$$

5.5. Hydrogen Ion Reduction

For hydrogen reduction

$$i=i_0\left\{\frac{[H^+]_s}{[H^+]_b}\exp\left(-\frac{\alpha_c F}{RT}\eta\right)\right\} \tag{5-15}$$

The surface concentration can be determined from the mass transfer equation:

$$i=K_{H^+}F([H^+]_b-[H^+]_s) \tag{5-16}$$

Eliminating $[H^+]_s$ from equations (5-15) and (5-16) gives after manipulation the same current versus voltage relationship given by equation (5-13). The cathodic Tafel slope for hydrogen ion reduction is

$$b_c=\frac{2.303RT}{\alpha_c F} \tag{5-17}$$

According to Bockris et al (1961), α_c=1 giving b_c=0.12 V at 25°C. The limiting diffusion current density for hydrogen reduction is

$$i_{\lim}^{d} = K_{H^+} F[H^+]_b \tag{5-18}$$

5.6. Water Reduction

Since water molecules are present in virtually unlimited quantities at the metal/solution interface, the water reduction rate is only controlled by the charge transfer process and the rate equation has pure Tafel behavior:

$$i = i_0 \cdot 10^{\frac{\eta}{b_c}} \tag{5-19}$$

The Tafel slope for water reduction is assumed to be the same as that for H^+ reduction (Nesic et al, 1996).

5.7. Implementation of the Corrosion Model

To construct the corrosion diagram (E/logi curves) and then to determine the type of corrosion behavior and surface metal ion concentration and surface pH profiles, the local mass transfer coefficients of O_2, H^+, OH^-, Cu^{2+} and Fe^{2+} in the mass transfer entrance length and fully developed region at various Reynolds numbers were determined by solving the set of transport equations (equations (3-25) to (3-29) and

equation (4-6)) simultaneously and then from equation (4-9). Equation (5-13) was used to determine the E/log*i* curves for oxygen reduction and hydrogen ion reduction respectively and equation (5-19) for water reduction. Equations (5-5) and (5-10) were used to determine E/log*i* curves for iron and copper dissolution respectively. The corrosion potential, E_{corr}, was determined numerically by determining the value of E at which

$$i_a = \sum i_c \tag{5-20}$$

The corrosion current densities, $i_{corr.}$ for iron and copper are then determined from equations (5-5) and (5-10). The metal/solution interface concentrations of Fe^{2+} and Cu^{2+} are calculated as follows:

$$[M^{z+}]_s = \frac{i_{corr}}{zFK_{M^{z+}}} + [M^{z+}]_b \tag{5-21}$$

Considering the fundamental definition of pH in terms of hydrogen ion concentration ($pH = -\log[H^+]$ where the unit for [H$^+$] is mol/dm^3) and knowing the ionization constant for water to be 10^{-14} at 25°C, the metal surface pH is determined by

$$pH_s = 14 + \log\left[\left(\frac{i_{corr}}{FK_{OH^-}} + [OH^-]_b\right) \times 10^{-3}\right] \tag{5-22}$$

where the $[OH^-]_b$ is bulk hydroxyl ion concentration (mol/m^3). Equation (5-22) is valid only when the current density for hydrogen evolution is negligible compared to that for oxygen reduction.

It should be mentioned that although exchange current densities for the above mentioned electrochemical reactions are based on previous experimental results (e. g. Bockris et al, 1961; Mattsson and Bockris, 1959), they are not reproducible. They vary substantially with small changes in the metal and solution composition and with the experimental technique used to determine them. Thus, in this study any calculation done for corrosion which is wholly or partially charge transfer control is done to illustrate the type of behavior to be expected rather than predict actual corrosion rates with any degree of accuracy. On the other hand mass transfer rate can be determined or calculated within 10% of error and wholly mass transfer controlled corrosion rates can be accurately predicted.

6. Results and Discussion

6.1. Introduction

All simulation results and experimental observation done for this study are presented in this chapter. The low Reynolds number k-ε eddy viscosity model was first used to predict the pipe-wall mass transfer rate in the developing concentration boundary layer region under fully developed hydrodynamic conditions, and tested against previous electrochemical measurement results (section 6.2). This turbulence model was then applied to simulate the effects of mass transfer on the corrosion of metals throughout the mass transfer entrance region in turbulent pipe flow (section 6.3). The low Reynolds number k-ε model was used to determine the local mass transfer coefficients and the corrosion model was used to construct the E/logi corrosion diagrams which take into account the effects of mass transfer resistance on the both anodic and cathodic reactions. In section 6.4, the turbulence model and the corrosion model have been applied to the numerical simulation of the effects of both electrode misalignment and mass transfer entry length on corrosion rate measurements in turbulent pipe flow. The interfacial metal

ion concentration and pH profiles were also determined in both section 6.3 and section 6.4 for mass transfer controlled, partial mass transfer controlled and charge transfer controlled corrosion and discussed in terms of their possible effect on film formation. The experimental observation results of the disruption of corrosion films formed on copper in flowing aerated 3% NaCl solution are presented in section 6.5. The resulting interaction between the disturbed flow and the films are also discussed in this section in terms of the near-wall turbulence parameter profiles calculated by the k-ε turbulence model.

6.2. Prediction and Comparison with Experimental Results

6.2.1. Introduction

As outlined in the literature review, a number of experimental studies of mass transfer to the pipe wall both in the developing concentration boundary layer and in the fully developed regions in turbulent flow have been published. This provides abundant experimental data to test the turbulence model used in this study. In this section, the low Reynolds number k-ε eddy viscosity model has been used to predict wall-mass transfer rates in the region of developing concentration boundary layer and compared with previous experiments. This model is then applied to predict the entrance length effects, relating to the discontinuity caused by the electrical insulation, on small local cathodes located in a large active cathode.

6.2.2. Computational Domain

The computational domain is shown in Fig. 6-1, where the mass transfer section commences at 100 mm. Non-uniform staggered grids (91×40) were used with the majority of nodes clustered in the near-wall region and mass transfer entrance region. The first near-wall node was placed at y=0.5~1μm so that $y^+ \leq 0.1$, and the first node close to the mass transfer entrance was placed at x=1μm. In order to account for the rapid change of concentration profile caused by the insulating layer of epoxy resin in the near wall region in the case of small electrodes embedded in large active electrodes, a finer grid system, 201×60, was used with the first near-wall node placed at y=0.2 μm.

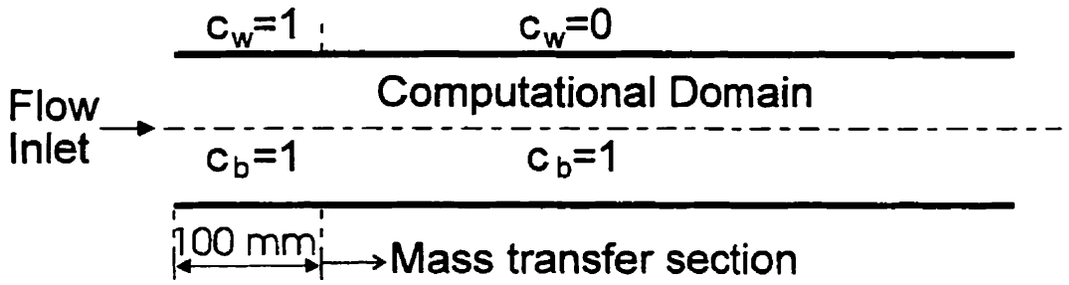

Fig. 6-1. Computational domain. Fully developed flow at inlet. Mass transfer section commences at 100 mm. Concentrations c_w and c_b are normalized. Pipe diameter: 54.8 mm, 25.4 mm and 40 mm.

6.2.3. Mass Transfer Entrance Length

Grid independence test Two grid systems (91×40 and 121×60) have been used to evaluate the grid dependence of the computational results. The comparison is shown in Fig. 6-2 where it is seen that the grid system (91×40) is sufficiently accurate to calculate the mass transfer coefficient profile in mass transfer entrance region when $L/d>10^{-3}$.

Comparison of NT and AKN low Reynolds number models The predicted (NT and AKN low Reynolds number models) and measured (Berger and Hau, 1977) wall-mass transfer rates, expressed in terms of mean Stanton numbers, in the developing concentration boundary layer and fully developed regions are compared in Fig. 6-3 for a Reynolds number of 63,200. Since the measured mass transfer rates are the mean value for each mass transfer test section, the numerically predicted local mass transfer rates have been averaged over each mass transfer section. The Stanton number in the fully developed region where,

$$St_d = 0.0165\,\mathrm{Re}^{-0.14}\,Sc^{-0.67} \tag{6-1}$$

given by Berger and Hau (1977) is also shown. In the developing concentration boundary layer region, the predictions with both, NT and AKN, LRN models are in good agreement with the experimental measurements. In the fully developed region, both models give predictions that are lower than the measurements, with the relative error -

18.5% for the NT model and -7% for the AKN model. Therefore, the AKN LRN model was used for the remainder of the study.

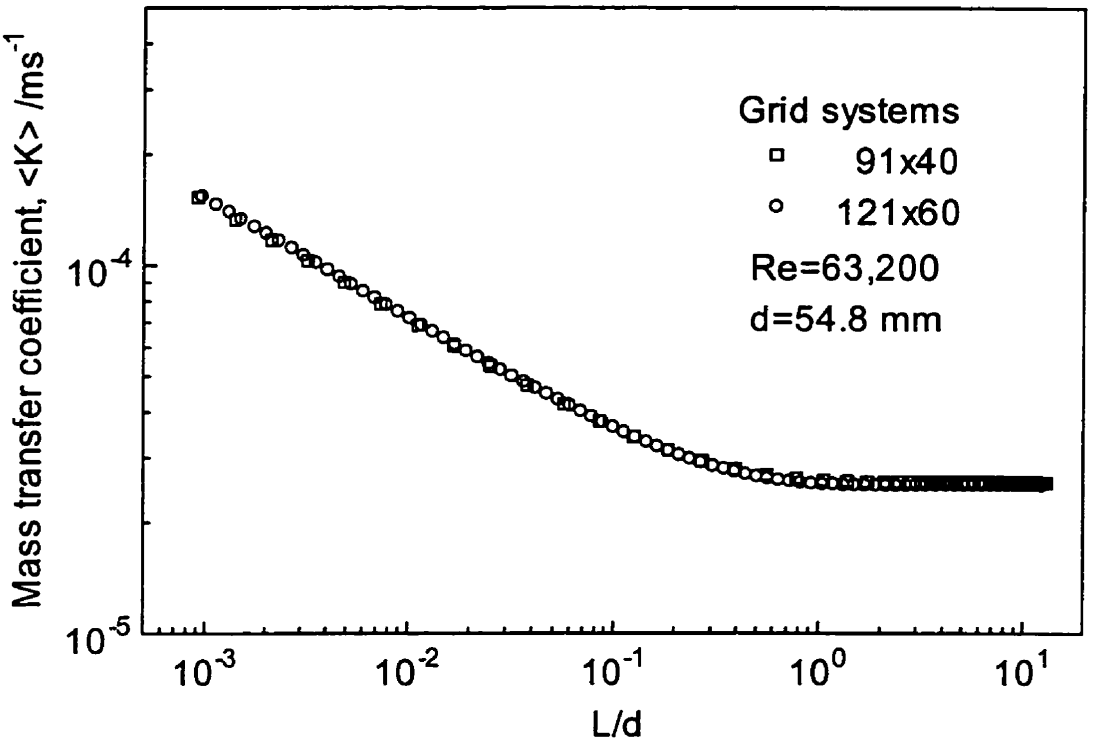

Fig. 6-2 Evaluation of grid dependence on computational results.

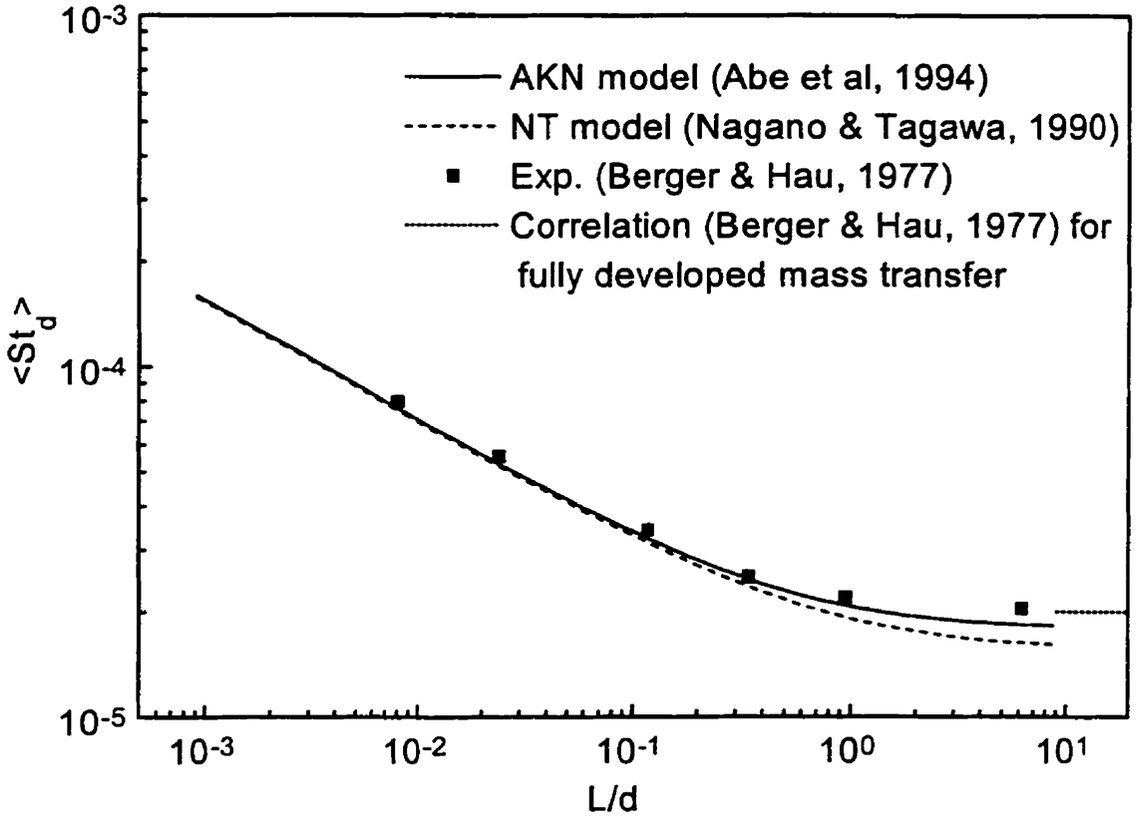

Fig. 6-3 Variation of mean Stanton number with L/d; Re=63,200, d=54.8mm, Sc=2244.

6.2.3.1.Comparison with Experiments of Son and Hanratty

The experimental studies of Son and Hanratty (1967) of mass transfer in the developing concentration boundary layer region were first numerically simulated. As mentioned in the literature review, Son and Hanratty applied the limiting diffusion current technique to measure the mass transport rate of $Fe(CN)_6^{3-}$ ion from bulk solution to the pipe wall electrode in turbulent pipe flow. In the Son and Hanratty experiments ten test sections with internal diameter of 25.4 mm and varying lengths from 0.0177 to 4.31 pipe-diameters, were used, with Reynolds numbers from 4000 to 62,000 and a Schmidt number of 2400.

The variation of predicted dimensionless mean mass transfer coefficients, $\langle K^+ \rangle$, with dimensionless distance from the entrance, L^+, are shown in Fig. 6-4, where they are compared to the results of Son and Hanratty (1967). It is seen that the present numerical predictions are in good agreement with the measurements for four Reynolds numbers in the mass transfer entrance region. In the fully developed region, the predictions are also in good agreement with the measurements with relative error less than 5%. The predictions indicate that the entrance length needed for the local mass transfer coefficient to become fully developed, $K^+ \approx K_\infty^+$, varies from $L^+ \approx 2500$ ($L/d \approx 4.32$) for Re=10,000 to $L^+ \approx 1700$ ($L/d=0.58$) for Re=55,100 at Sc=2400. The entrance length for the mean mass transfer coefficient to approach the fully developed value, $\langle K^+ \rangle \approx K_\infty^+$, varies from $L^+ \approx 1.5 \times 10^4$ ($L/d \approx 12.48$) for Re=20,000 to $L^+ \approx 1.1 \times 10^4$ ($L/d \approx 3.81$) for Re=55,100. Both

predictions for dimensionless entrance lengths are in good agreement with other researchers' experimental results (Shaw and Hanratty, 1977; Shaw, 1963; Son, 1965).

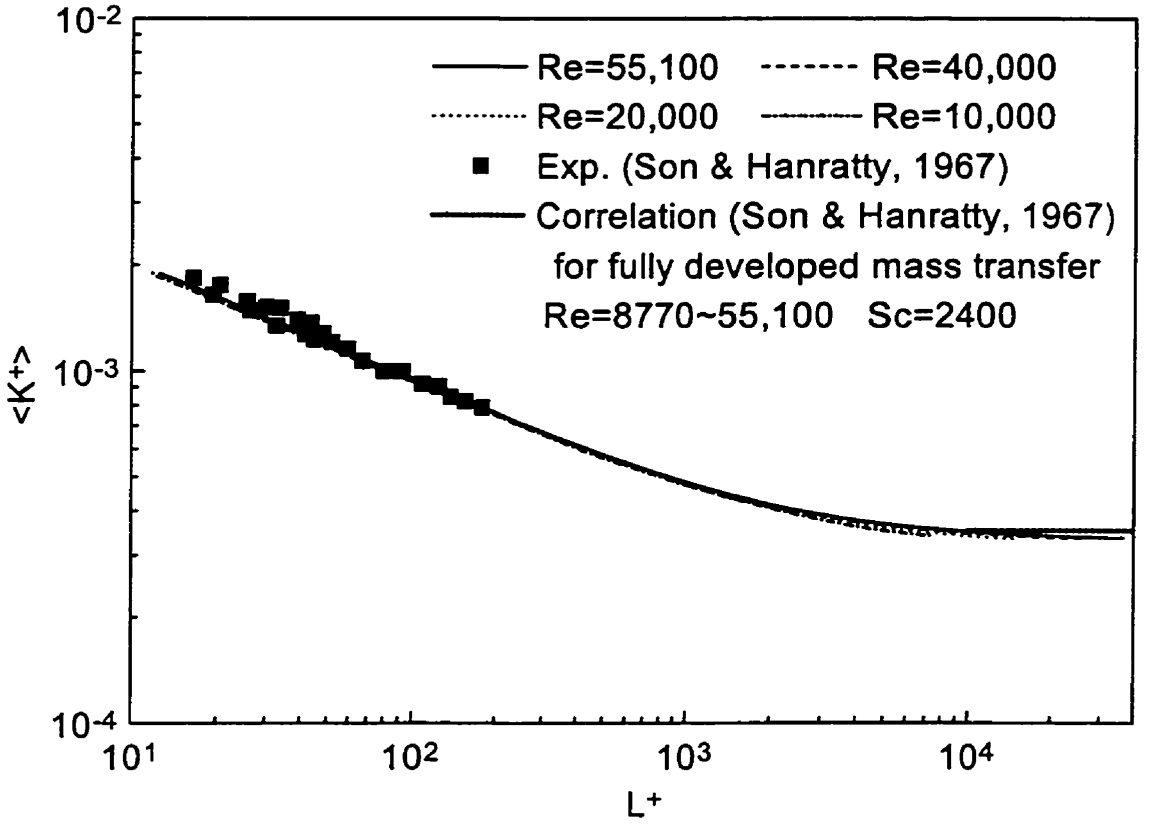

Fig. 6-4 Variation of dimensionless mass transfer coefficient with L^+; d=25.4 mm.

6.2.3.2.Comparison with Experiments of Berger and Hau

The experimental studies of Berger and Hau (1977) of mass transfer in the developing concentration boundary layer region were then numerically simulated. Berger and Hau also applied the limiting diffusion current technique to measure the mass transport rate of $Fe(CN)_6^{3-}$ ion to a pipe wall electrode in turbulent pipe flow. Their study included experiments with nine mass transfer sections with an internal diameter of 54.8 mm and varying lengths from 0.008 to 9.12 pipe-diameters, with Reynolds numbers from 1.29×10^4 to 13.5×10^4 and a Schmidt number of 2244.

The variation of the predicted and measured (Berger and Hau, 1977) mean Stanton numbers with L/d in the region of developing concentration boundary layer, for four different Reynolds numbers, are shown in Fig. 6-5, as well as the Stanton numbers in the fully developed region. The predictions are in excellent agreement with the measurements for all four Reynolds numbers in the region of developing concentration boundary layer. In the fully developed region, the predicted Stanton numbers are very close to the experimental values.

The above tests show that the predictions of the mass transfer are in good agreement with the electrochemical measurements of Son and Hanratty (1967), and of Berger and Hau (1977) in both the developing concentration boundary layer region and

the fully developed region. While the experimental results of Son and Hanratty (1967) in the developing boundary region were expressed by the following correlation:

$$< K^+ > \quad = \quad 0.81(L^+)^{-1/3} Sc^{-2/3} \tag{6-2}$$

which is derived by Son and Hanratty (1967), the experimental results of Berger and Hau (1977) in the developing concentration boundary region were best fitted with the integrated Leveque equation:

$$St_d = 0.276\,\mathrm{Re}^{-0.417} Sc^{-2/3}\left(\frac{L}{d}\right)^{-1/3}. \tag{6-3}$$

Since the predictions are in good agreement with both experimental results, the correlations (6-2) and (6-3) should be equivalent despite the different dimensionless form used. In fact, the derivation (see Appendix II) has showed that equation (6-2) can be derived from equation (6-3) by using Blasius friction relation:

$$f \quad = \quad 0.316\,\mathrm{Re}^{-0.25} \qquad 4000 < \mathrm{Re} < 10^5. \tag{6-4}$$

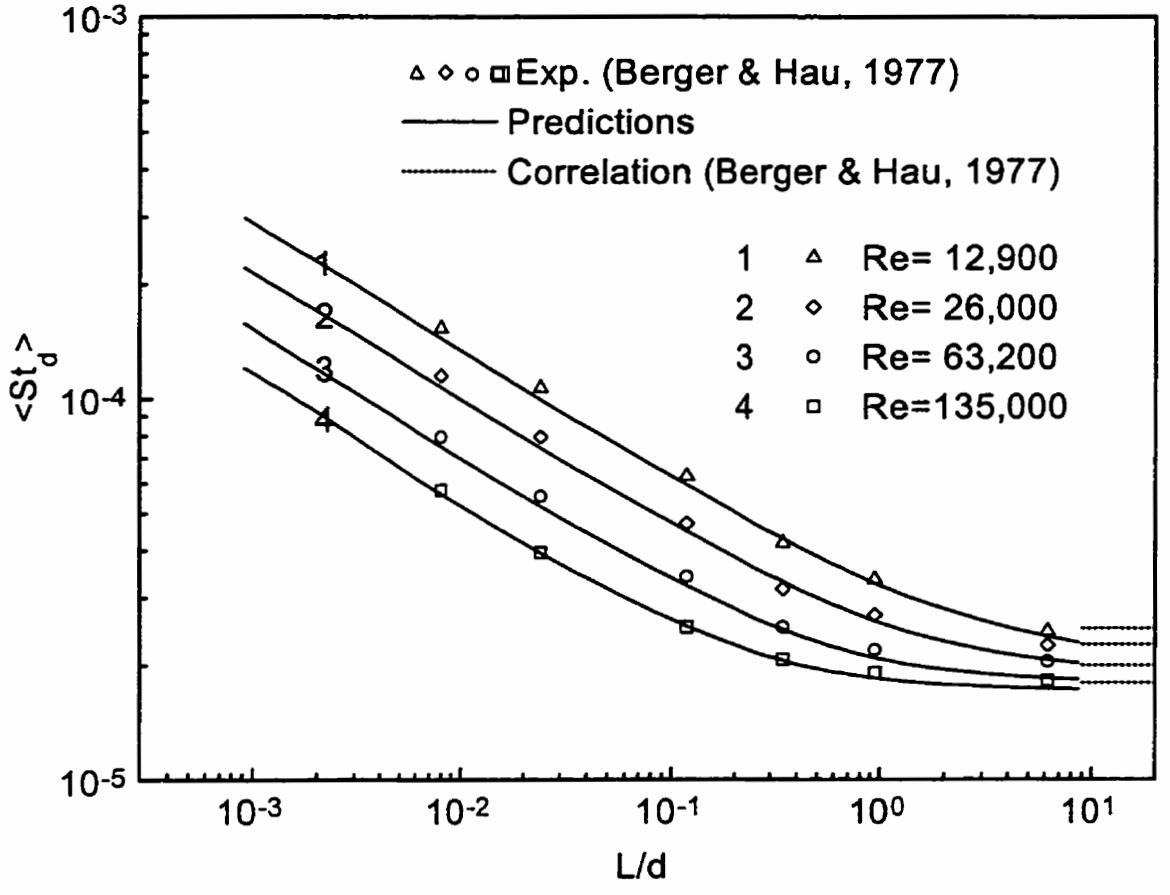

Fig. 6-5 Variation of mean Stanton number with L/d; d=54.8 mm, Sc=2244.

6.2.3.3. Concentration Distribution in Entrance Region

The normalized simulated concentration distributions of $Fe(CN)_6^{3-}$ for four Reynolds numbers in the mass transfer entrance region where the concentration boundary layer is developing (Fig. 6-6) show the effect of the Reynolds number on the entrance length and on the thickness of the fully developed concentration boundary layer. The variation of local Stanton numbers (calculated from the simulated local mass transfer coefficients) with L/d is shown in Fig. 6-7. The mass transfer rates approach infinity at the beginning of the mass transfer section. For all Reynolds numbers investigated, the Stanton numbers reach the fully developed values at $L/d \leq 5$. If the entrance length is defined as the distance from the entrance to where the local Stanton number reaches a value 5% higher than the fully developed value, the entrance length, based on the predictions, was found to vary from $L/d \approx 5$ for Re=12,900 to $L/d \approx 0.25$ for Re=135,000 at Sc=2244. If experiments are to be done under conditions where the effect of the entrance length can be neglected and the mean mass transfer coefficients approach the fully developed values then L/d values ≈ 9.7 at Re=26,000 to $L/d \approx 1.6$ at Re=135,000, with Sc=2244 are required.

Fig. 6-8 shows the variation of concentration profile with distance from the entrance in the near-wall region. It is seen that the concentration profile undergoes a rapid change after entering the mass transfer section. An original flat profile changes to

one exhibiting a large gradient of concentration near the wall. Finally, a fully developed concentration profile is reached if the mass transfer section is long enough.

The predicted momentum and mass transfer transport coefficients μ_{eff} and D_{eff} in the fully developed concentration boundary layer region for Re=63,200 and Sc=2244 are shown in Fig. 6-9. Far from the wall (y≥1 mm), the effective viscosity is about 10 times larger than the molecular viscosity, indicating that the flow is dominated by turbulent transport. As the wall is approached, the magnitude of effective the viscosity approaches the value of the molecular viscosity, indicating that the turbulence is gradually being damped. Consequently, the viscous sublayer with a thickness of y≈60 μm is formed, in which the flow is controlled by viscous forces. Although very little turbulence is retained at the edge of the viscous sublayer, the effective diffusivity is still about 60 times larger than the molecular diffusivity. This demonstrates that residual turbulence, which has negligible effect on momentum transport, still has considerable effect on mass transfer. This behavior is to be expected for fluid with a large Schmidt number. The turbulent diffusivity is reduced as the wall is approached, becoming insignificant at about 4 μm from the wall (y^+≈0.25) when mass is transported exclusively by molecular diffusion.

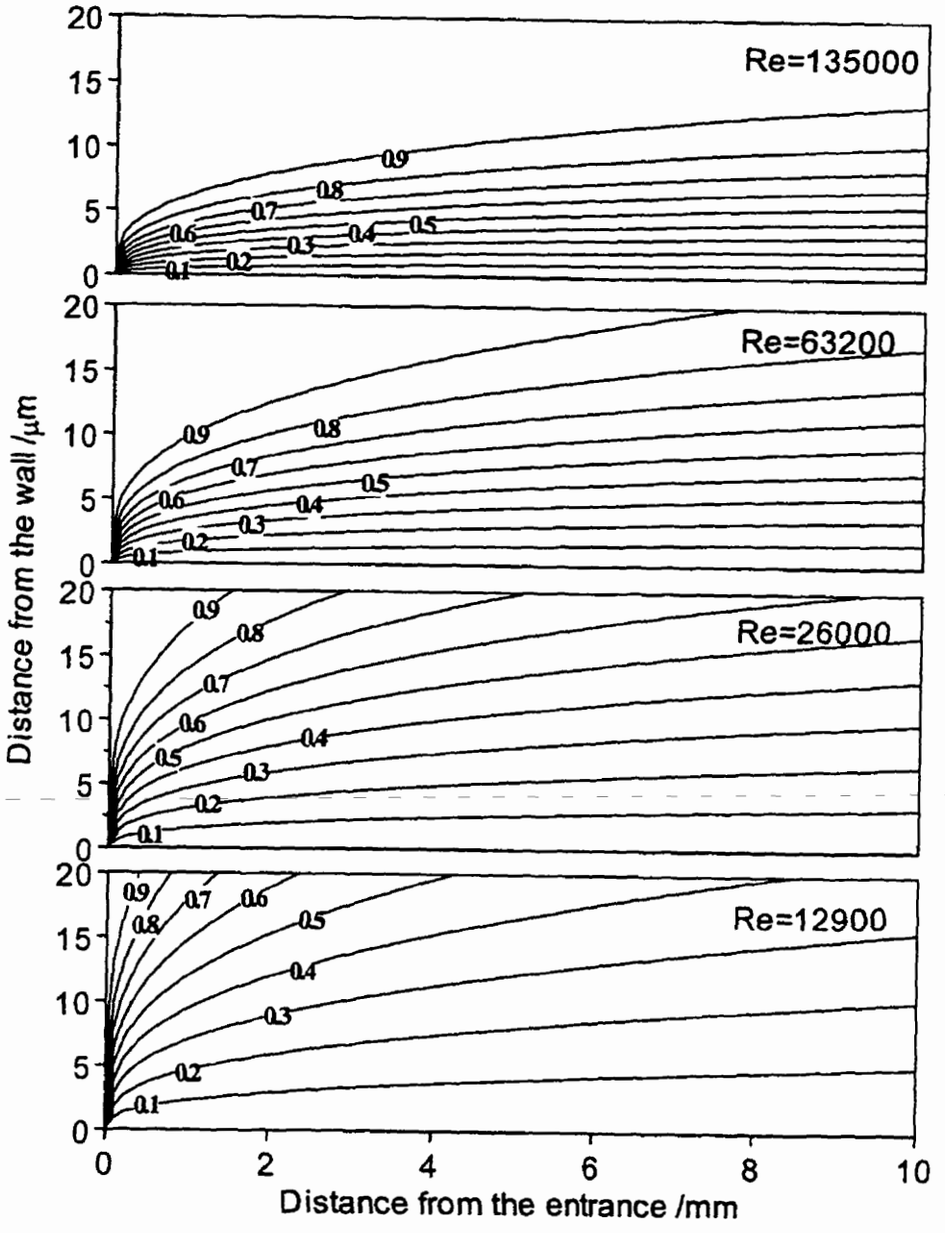

Fig. 6-6 Normalized concentration distribution of $Fe(CN)_6^{3-}$ in the developing concentration boundary layer region for four Reynolds numbers. Lines correspond to the normalized concentration contours.

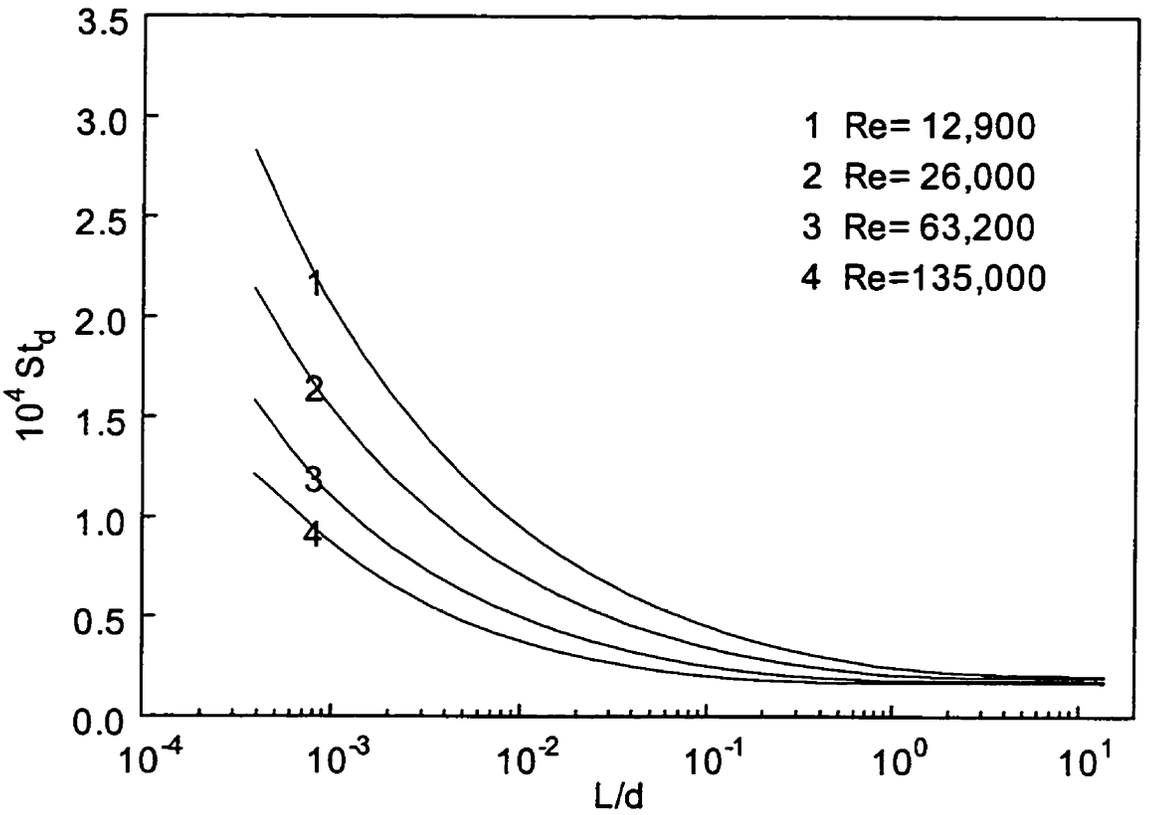

Fig. 6-7 Variation of local Stanton number with L/d; d=54.8 mm.

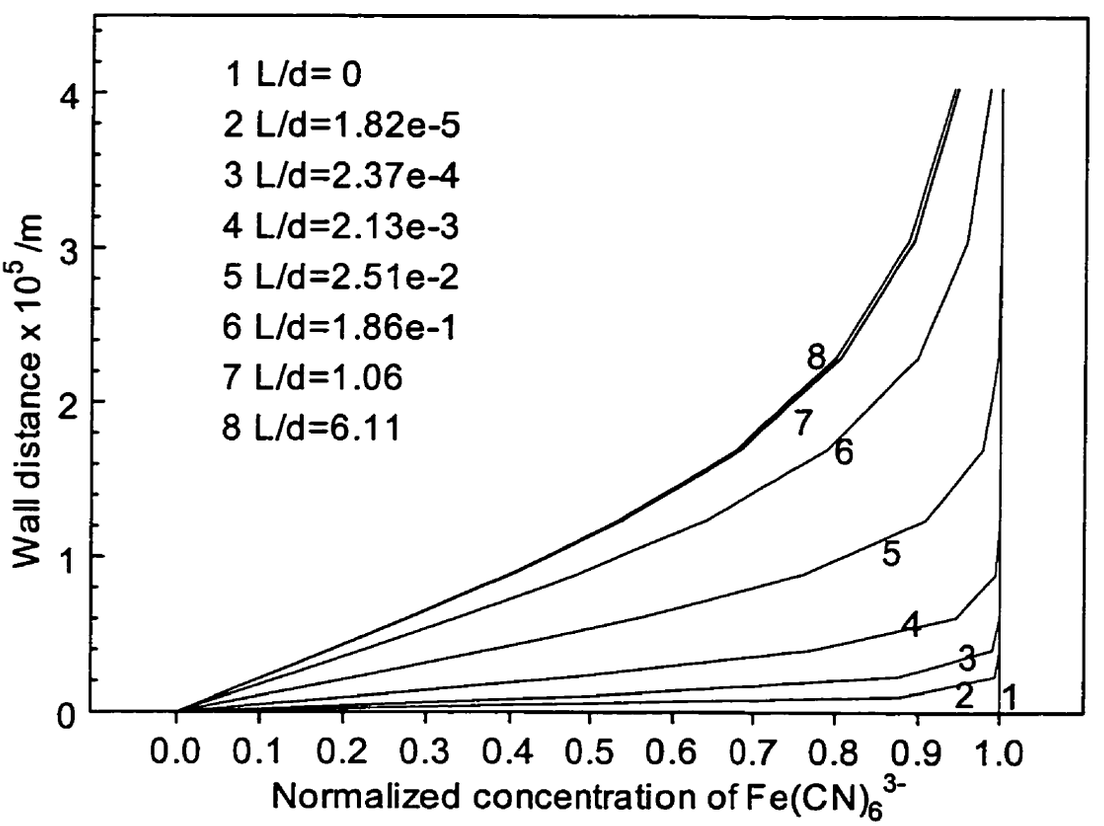

Fig. 6-8 Change of concentration profile with distance from the entrance in the near wall region; Re=63,200, d=54.8 mm, Sc=2244.

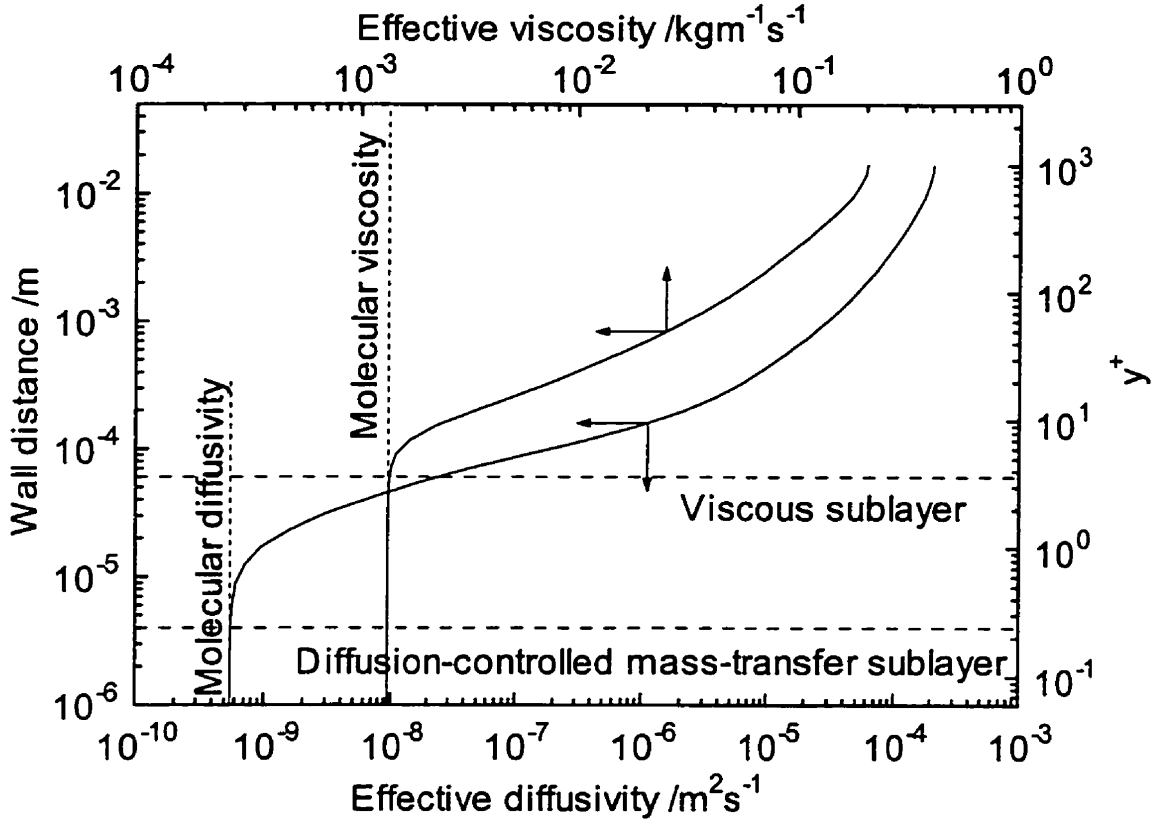

Fig. 6-9 Variation of transport coefficients with the distance from the wall;

Re=63,200, Sc=2244, d=54.8 mm.

6.2.4. Small Local Cathode

As mentioned in the literature review, Schutz (1964) applied the limiting diffusion current measurement technique to measure local mass transfer rates in the region of the developing concentration boundary layer, in a 40 mm diameter tube. Schutz's experimental study was numerically simulated in order to investigate the potential errors in the application of small electrodes to measure local mass transfer coefficients in mass transfer entrance regions. The turbulence model used in this study is a two-dimensionai model and as a first approach short tubular electrodes were used for the numerical simulations. In Schutz's experiment, 18 round local electrodes of 1 to 3 mm diameter were fitted into a large active cathode. The first local electrode was mounted 2 mm from the entrance. The small electrodes were electrically insulated from the large cathode by a 0.1 mm thick layer of epoxy resin.

6.2.4.1. Concentration Distribution around Small Cathode

The simulated profiles of mass transfer coefficient and surface species concentration in the mass transfer entrance region, with a 1 mm long tubular local electrode and 0.1 mm insulation, are shown in Fig. 6-10. The normalized simulated concentration distributions of $Fe(CN)_6^{3-}$ in the region around the small electrode are shown in Fig. 6-11. It can be seen from Fig. 6-10a that the largest change in the local mass transfer coefficient occurs in the leading edge region (<0.2 mm from the entrance). Thus, a much smaller electrode, say 10 μm in diameter with 1 μm insulation, would be

needed to discriminate the local mass transfer rate in this region which would impose severe practical difficulties. In the remaining entrance region and fully developed region, it is possible to use local electrodes to measure local mass transfer coefficients.

6.2.4.2.Predicted Measurement Error

We can also see from Fig. 6-10b and Fig. 6-11 that the concentration distributions are disturbed by the insulating junction. The normalized surface species concentration jumps from zero to about 0.35 because there is no mass transfer on the surface of the electrical insulation around the small electrode isolation, which results in the enhancement of the mass transfer coefficient at the leading edge of the local electrode (Fig. 6-10a) and causes the error in the measurement of local mass transfer rate. Fig. 6-12 shows the effect of electrode size on the measurement error. When a 1 mm wide local electrode with 0.1 mm insulation is used to measure the mass transfer coefficient, the measured value is 7.6% higher than the true value. When a 0.1 mm wide electrode with 0.1 mm insulation is used, the measured value is 45% higher than the true value. The influence of electrical insulation thickness on measurement error caused by the edge effect is shown in Fig. 6-13, where we can see that thicker insulation creates larger errors.

In the experiments done by Deslouis et al (1980, 1981), a microelectrode of 80 μm diameter with 10 μm insulation was used to measure local mass transfer coefficients. The present simulation (Fig. 6-14), with 10 μm insulation in a straight pipe shows that

when a local tubular electrode 80 μm electrode is used the measured value is predicted to be 8.6% higher than the true value, which would be acceptable.

The simulations in Fig. 6-12 and Fig. 6-14 were with a two-dimensional model and the results apply only to the center line for round local electrodes. It can be inferred from Fig. 6-12 and Fig. 6-14 that the round local electrodes, which were used by Schutz (1964) and Deslouis et al (1980, 1981) will produce larger errors than the tubular local electrodes simulated in the present study. Small rectangular local electrodes would give smaller errors than round electrodes with the same surface area.

The above calculations demonstrate the severe practical limitation in measuring local mass transfer coefficients in the leading edge area (<0.2 mm) of mass transfer entrance regions in pipes. In the remaining region of the entrance section and fully developed concentration region, use of local tubular electrodes would give values close to the true values providing the insulation is sufficiently thin. The application of numerical simulation conditions can assist in assessing the errors during the experimental design stage. Three-dimensional simulations would be preferred for small round local electrodes. Unfortunately the simulation time increases quadratically with the number of nodes. Three-dimensional fine mesh requirements for mass transfer simulations at the high Schmidt numbers encountered in aqueous solutions would require considerably more computing power than used in the present study, where the simulation times, with a SPARC station 20-612, are 50 minutes for the nodes of 91×40 and 224 minutes for the nodes of 121×60 for Re=63,200. Three dimensional

computational grids would require several orders of magnitude greater simulation times and would also lead to severe memory problem with the size of the arrays generated.

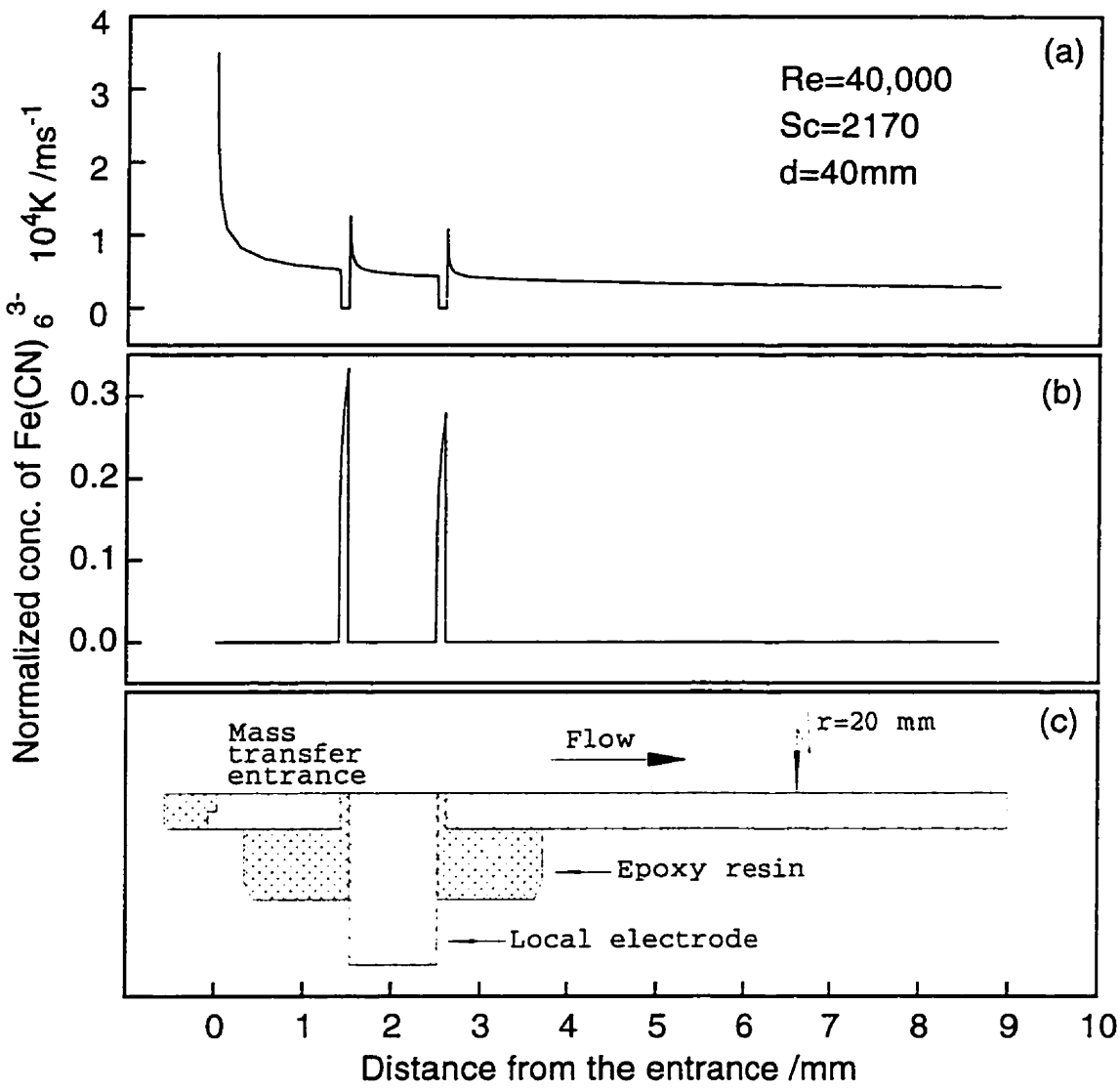

Fig. 6-10 Variation of the profile of mass transfer coefficient and surface species concentration in the mass transfer entrance region of a 40 mm diameter pipe. A 1 mm long tubular electrode with 0.1 mm insulation is fitted into a large active cathode.

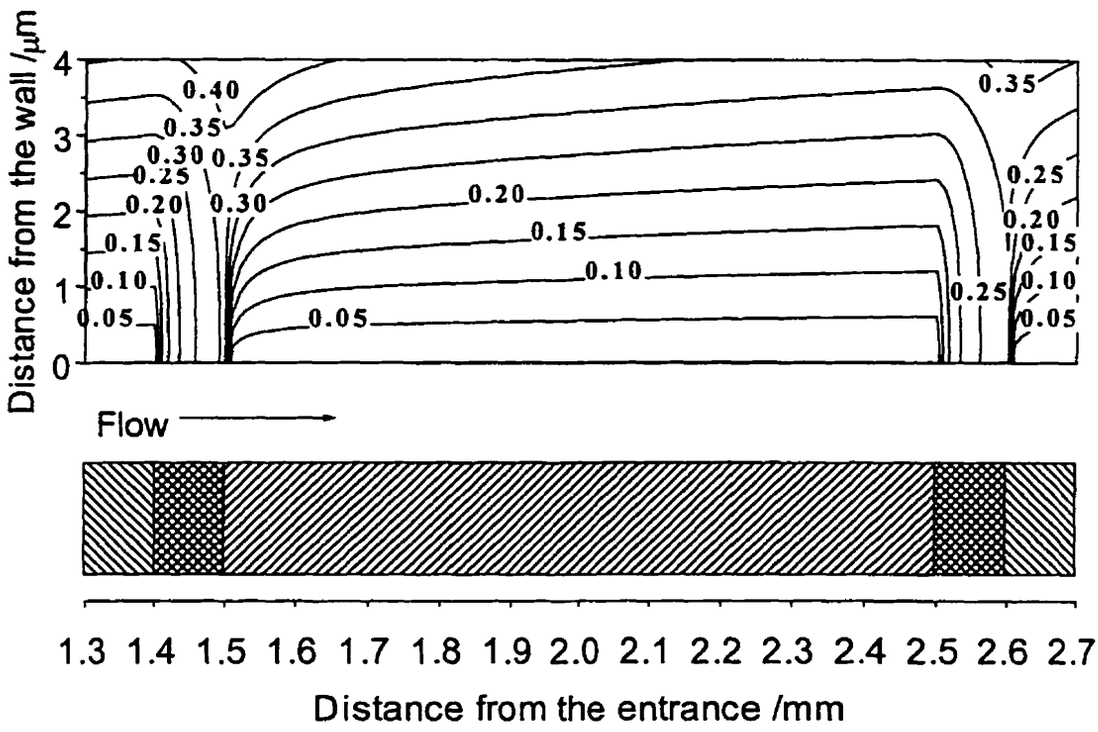

Fig. 6-11 Normalized concentration distribution of $Fe(CN)_6^{3-}$ in the small electrode region; Re=40,000, Sc=2170, d=40 mm. Lines correspond to the normalized concentration contours.

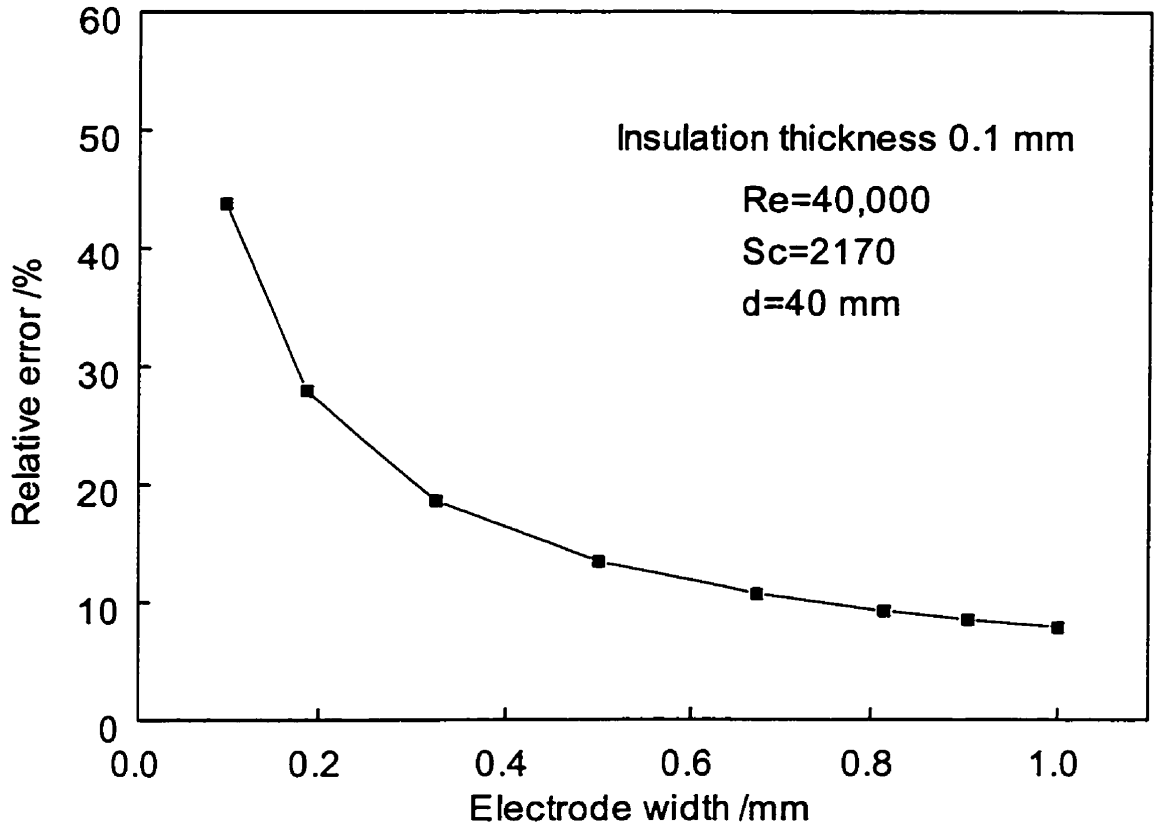

Fig. 6-12 Effect of local electrode width on measurement error. Insulation thickness: 0.1 mm; Re=40000; Sc=2170; d=40 mm.

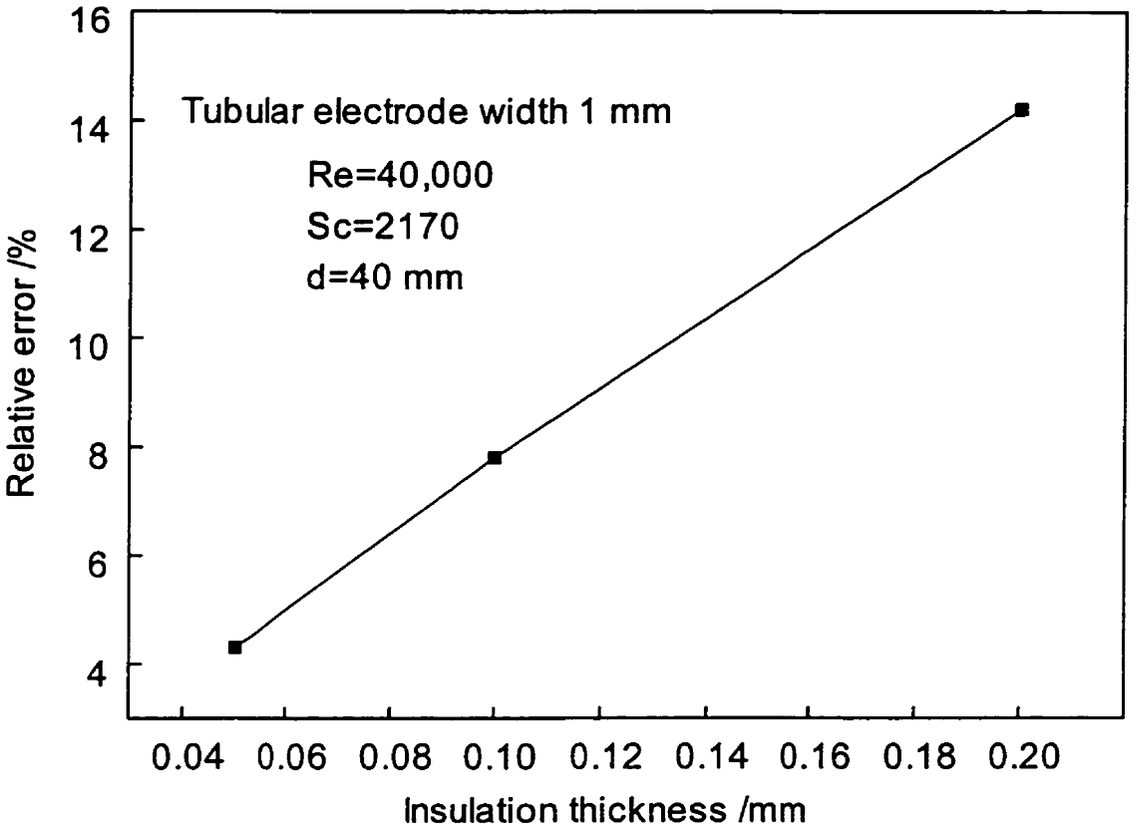

Fig. 6-13 Effect of insulation thickness on measurement error. Tubular electrode length: 1 mm; Re=40000; Sc=2170; d=40 mm.

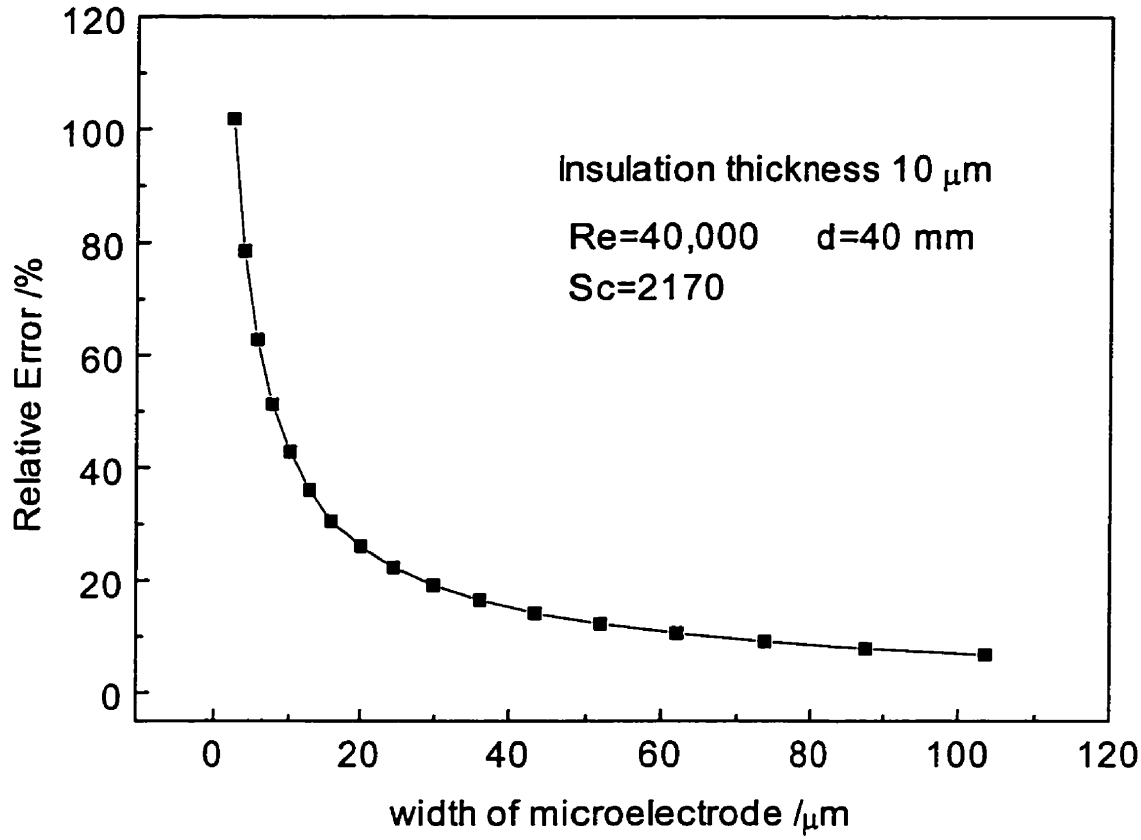

Fig. 6-14 Effect of local microelectrode width on measurement error.

Insulation thickness: 10 μm; Re=40000; Sc=2170; d=40 mm.

6.3. Application to Corrosion Modelling in Mass Transfer Entrance Region

6.3.1. Introduction

Flow sensitive corrosion rates will vary along the mass transfer entry length where the concentration boundary layer is developing and the local mass transfer rates are much higher than the fully developed values. Flow sensitivities of the corrosion rates relate to effects of flow on the anodic and cathodic reactions; including film formation following metal ion concentration and pH changes at the corroding surface.

The calculation of corrosion rates in the mass transfer entrance region has important technical applications. For example, the corrosion at a pipe wall where small patches of protective film have been removed will occur within a developing mass transfer boundary layer. Another application is the calculation of the entrance effect when using pipe wall electrodes to measure corrosion rates in pipes. In both these examples there will be a sharp decrease in the rates of mass transfer of corrosion products and reactants as the mass transfer boundary layers develop. The decrease in mass transfer rates will lead to a decrease in the corrosion rates with the magnitude determined by the extent to which mass transfer controls the overall corrosion reaction.

The average mass transfer coefficients, $<K>$, in the mass transfer entry region can be determined from the integrated turbulent Leveque equation (Berger and Hau, 1977)

$$\frac{<K>}{U_b} = 0.276\,\mathrm{Re}^{-0.417}\,Sc^{-2/3}\left(\frac{L}{d}\right)^{-1/3} \tag{6-5}$$

and local point values, K, from the differentiated form

$$\frac{K}{U_b} = 0.184\,\mathrm{Re}^{-0.417}\,Sc^{-2/3}\left(\frac{L}{d}\right)^{-1/3} \tag{6-6}$$

The mass transfer entry length can be defined as the distance from the entrance where local mass transfer rate attains the fully developed value (Berger and Hau, 1977). These equations have a very limited range of validity, depending on the Reynolds number. For example, the range of validity changes from $0< L/d < 0.5$ for $Re \leq 10^4$ to $0< L/d < 0.1$ for $Re > 10^5$ (Berger and Hau, 1977). In general, equations (6-5) and (6-6) only apply to less than 10% mass transfer entry length.

In the previous sections, the low Reynolds number k-ε turbulence models were used to successfully simulate the experimental mass transfer results of Son and Hanratty (1967) and Berger and Hau (1977) throughout the mass transfer entry length from the entrance to fully developed flow conditions (Wang, et al, 1996).

In this section the effects of the mass transfer on the corrosion of metals throughout the mass transfer entry lengths in turbulent flow in pipes were investigated. Kinetic corrosion diagrams (E-log i) were constructed to determine the local corrosion rates for metals with a wide range of electrochemical rate constants, k_s, corroding in neutral and acidic solutions. As mentioned in section 5.1, iron has been chosen as a representative of metals, with a low value of exchange current density, i_o, whose anodic dissolution is not affected by flow in the absence of film formation and copper to

represent metals with a relatively high exchange current density, i_o, whose anodic dissolution is flow sensitive. The cathodic reactions considered include oxygen, hydrogen ion and water reduction. In addition to corrosion rates the surface concentration of metal ions and pH along the entry length are established.

6.3.2. Iron

In the following sections the corrosion rates, surface ferrous ion concentration and pH are investigated. Two situations are considered: the corrosion is under charge transfer control; and the corrosion is under mass transfer control.

6.3.2.1.Charge Transfer Control

Fig. 6-15 shows the effects of Reynolds number on E/logi curves for the Reynolds number of 10^4 to 10^5 in the fully developed mass transfer region at pH=1. Fig. 6-16 shows the mass transfer entrance effect on the E/logi curves at Re=10^4 and pH=1. In both cases the solution is assumed to be deaerated and oxygen reduction is not taken into account. It is seen from Fig. 6-15 and Fig. 6-16 that E_{corr} is in the potential region where corrosion is solely under charge transfer control. The flow effects on the hydrogen evolution reaction occur outside the range of the corrosion potential. In Fig. 6-17 the Fe^{2+} concentration at the metal surface along the mass transfer entry length is shown at various flow rates. For each Reynolds number, the surface ferrous ion concentration increases along the length of the mass transfer section, approaching a stable value in fully developed conditions. The non-uniform surface ferrous ion concentration profiles can be explained by reviewing the calculation of the interfacial ferrous ion concentration

$$[Fe^{2+}]_s = \frac{i_{corr}}{zFK_{Fe^{2+}}} + [Fe^{2+}]_b \qquad (6\text{-}7)$$

where i_{corr} is constant for charge transfer controlled corrosion. Since the mass transfer coefficient for ferrous ions, $K_{Fe^{2+}}$, decreases along the mass transfer entry length and increases with rising Reynolds number, the resulting surface ferrous ion concentration will increase along the entry length and decrease with increasing Reynolds number.

The surface pH value is almost the same as bulk pH value because of high bulk H^+ concentration and high mass transfer coefficient for H^+ and film formation would not be possible under these conditions.

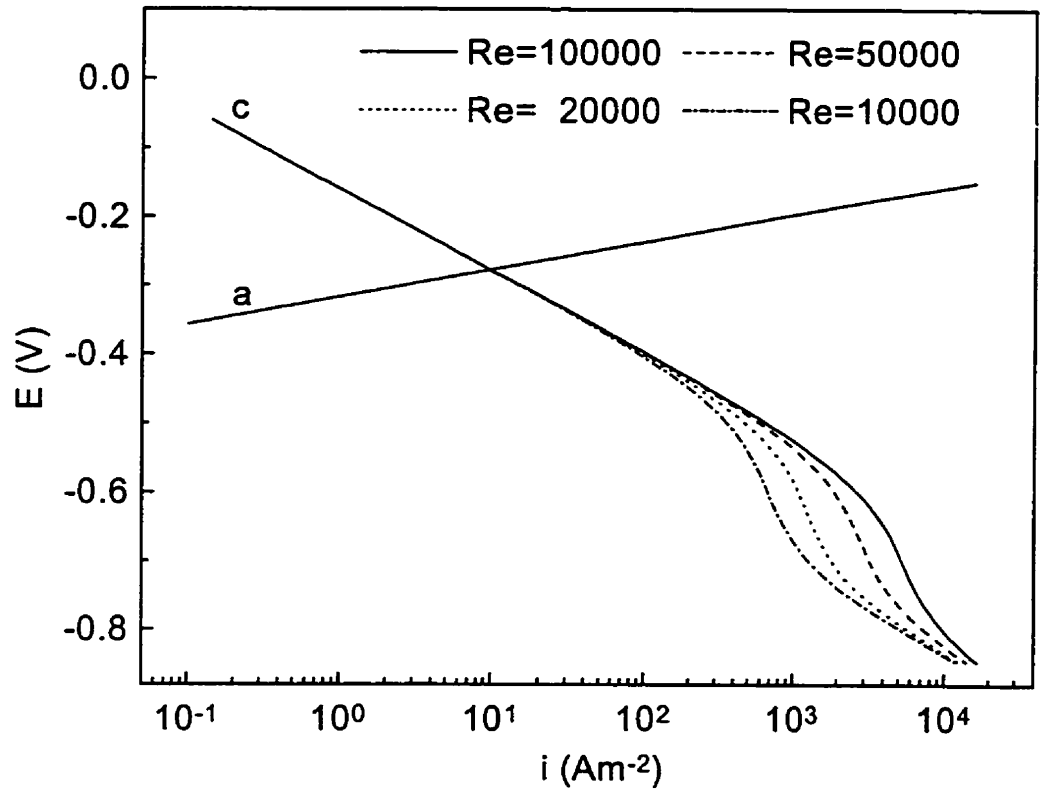

Fig. 6-15 Effect of Reynolds number on E/logi curves in fully developed region; a: anodic iron dissolution, c: hydrogen evolution; bulk pH=1, deaerated solution.

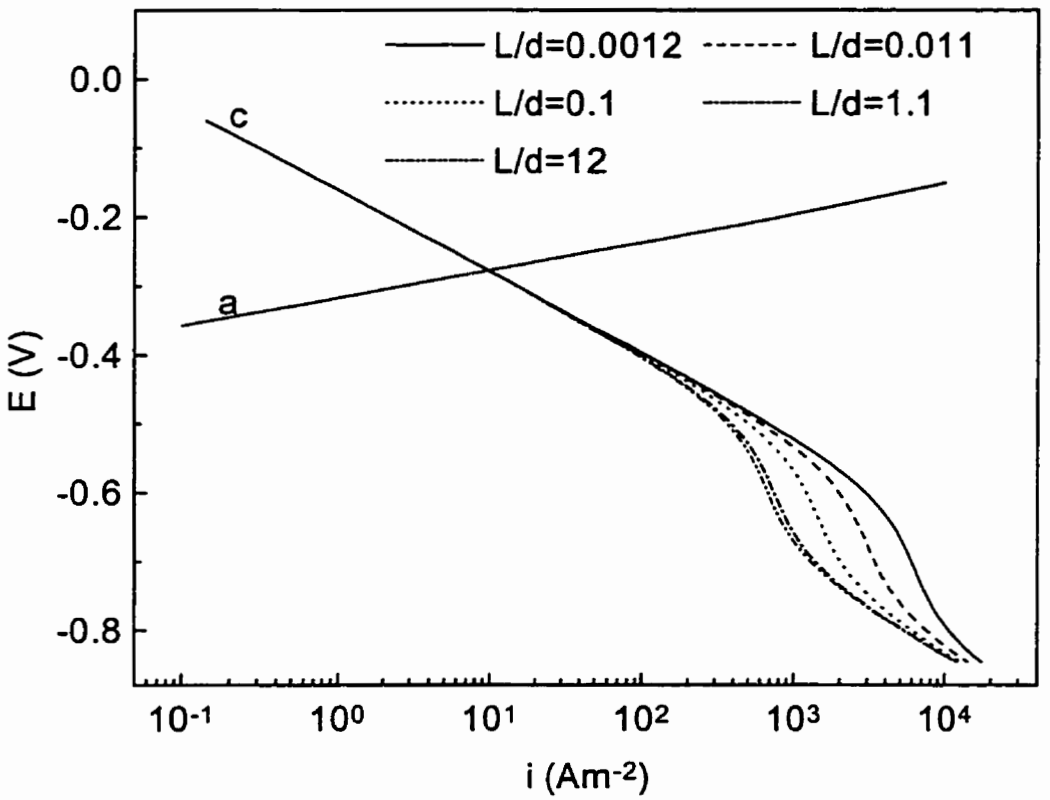

Fig. 6-16 Effect of the mass transfer entrance on E/logi curves; a: anodic iron dissolution, c: hydrogen evolution; Re=10^4, bulk pH=1, deaerated solution.

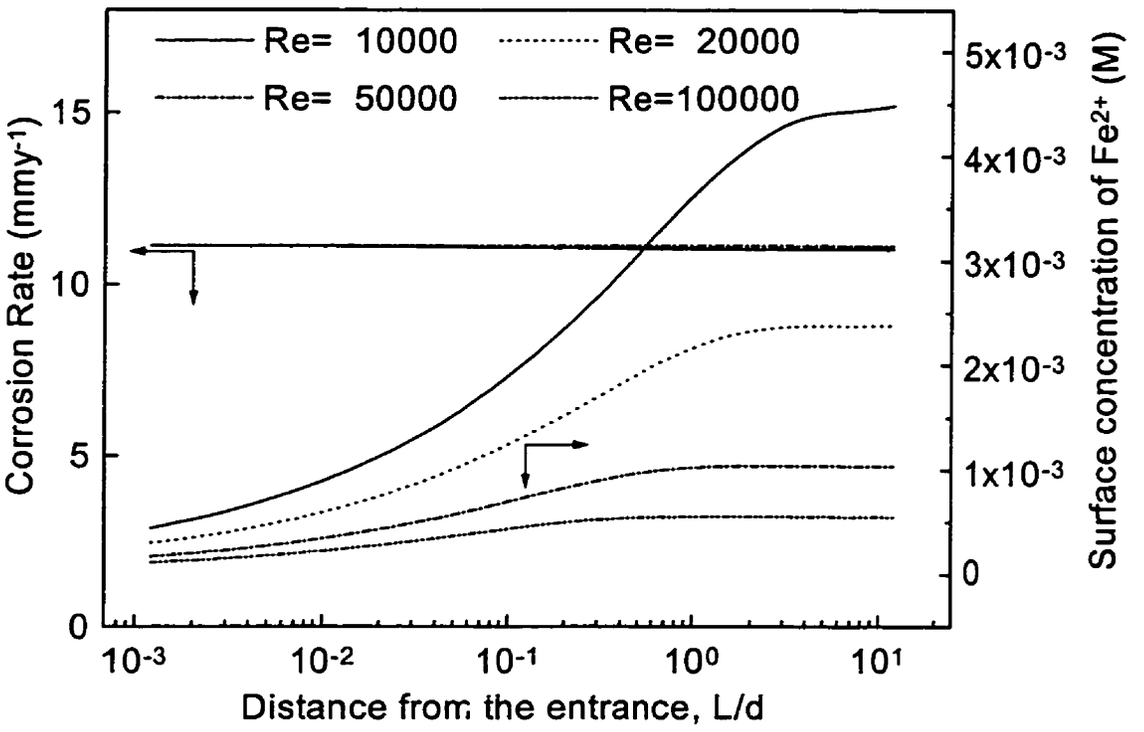

Fig. 6-17 Corrosion rate and surface concentration of dissolved Fe^{2+} ion as a function of the distance from the leading edge of the mass transfer entrance at various Reynolds numbers; bulk pH=1, deaerated solution.

Turgoose et al's studies (1995) showed that the ferrous ion concentration on metal/solution interface decreases as the leading edge of the electrode is approached with constant corrosion rate assumed. This corresponds to the above case in which the corrosion is under charge transfer control.

6.3.2.2.Mass Transfer Control

If the solution pH is greater than 4, the cathodic current for H^+ reduction is negligible compared to that for O_2 reduction. The E/logi curves are plotted in Fig. 6-18 as a function of Reynolds number in the fully developed mass transfer region and in Fig. 6-19 as a function of the distance from the entrance at $Re=10^4$. The solution pH is 6 and oxygen reduction is considered. From both Figures we can see that the corrosion potential is in the region where corrosion is solely controlled by the transport of O_2 from the bulk solution to the metal surface. Under this condition the corrosion rate decreases along the mass transfer entrance (Fig. 6-20), and increases with increasing Reynolds number. It is interesting to observe from Fig. 6-20 that although the corrosion rate increases by one order of magnitude when the Reynolds number increases from 10^4 to 10^5 and when the leading edge of mass transfer entrance region is approached, the surface Fe^{2+} varies very little with Reynolds number or the distance from the mass transfer entrance. This can be explained by reviewing the calculation of the interfacial ferrous ion concentration

$$[Fe^{2+}]_s = \frac{i_{corr}}{zFK_{Fe^{2+}}} + [Fe^{2+}]_b \qquad (6\text{-}8)$$

where,

$$i_{corr} = i_{\lim}^{d} = 4K_{O_2} F[O_2]_b \tag{6-9}$$

From equations (6-8) and (6-9):

$$[Fe^{2+}]_s = \frac{2K_{O_2}[O_2]_b}{K_{Fe^{2+}}} + [Fe^{2+}]_b \tag{6-10}$$

where the bulk oxygen concentration $[O_2]_b$ is constant. Based on the numerical simulation, the ratio of the mass transfer coefficient of O_2 to that of Fe^{2+}, ($K_{O_2}/K_{Fe^{2+}}$), is almost constant in the entrance and fully developed regions for the range of Reynolds numbers investigated. This characteristic can also be confirmed by reviewing turbulent Leveque equation (equation Fig. 6-5) for the mass transfer entrance region and straight pipe correlation of Berger and Hau (1977) for fully developed region:

$$\frac{K}{U_b} = 0.0165 \mathrm{Re}^{-0.14} Sc^{-2/3} \tag{6-11}$$

where it is seen that the ratio of mass transfer coefficients of two species is constant in both entrance and fully developed region:

$$\frac{K_{O_2}}{K_{Fe^{2+}}} = \left(\frac{D_{O_2}}{D_{Fe^{2+}}} \right)^{2/3} \tag{6-12}$$

where D_{O_2} and $D_{Fe^{2+}}$ are the diffusion coefficients of O_2 and Fe^{2+} ion. This is in agreement with our prediction.

The surface pH values for various Reynolds numbers are shown in Fig. 6-21 as a function of the distance from the leading edge of mass transfer entrance region where it

is seen that there is no entrance effect on surface pH value when the corrosion process is controlled by the transport of oxygen to the metal surface. The high surface pH value is caused by the high OH^- concentration which is produced by the oxygen reduction reaction:

$$O_2 + 2H_2O + 4e \rightarrow 4OH^- \tag{6-13}$$

The explanation for the lack of change of the surface Fe^{2+} concentration also applies to the surface pH value as well. The predictions (Fig. 6-21) indicate that solution flow has no effect on the surface pH value, which is further confirmed by the fact that the predicted surface pH value (pH_s=10.7) for the Reynolds number range investigated is very closed to the calculation (pH=10.9) of Engell and Forchhammer (1965) in stagnant solution.

In brief, the surface concentration of dissolved metal ion and surface pH (although substantially different to the bulk values) vary little with Reynolds number and the distance from the mass transfer entrance. This is a result of the fact that the *ratio* of the mass transfer coefficients for the various species remains constant throughout the mass transfer entry length and also maintains the same value with changing Reynolds numbers.

For laminar flow the differential form of Leveque equation (Shaw et al, 1963) is

$$\frac{K}{U_b} = 1.082\,\mathrm{Re}^{-2/3}\,Sc^{-2/3}\left(\frac{d}{L}\right)^{-1/3} \tag{6-14}$$

Comparison of equation (6-14) with equation (6-6) indicates that the ratio of the mass transfer coefficients of two species can also be expressed by equation (6-12) and is constant. Therefore, above conclusion also applies to laminar flow.

Knowledge of both surface metal ion and surface pH value can be helpful in the prediction of the precipitation of hydroxide and/or oxide. As nearly constant surface concentration of dissolved metal ions and surface pH value are predicted when corrosion is under oxygen mass transfer control, conditions for film formation are uniform throughout the mass transfer entrance region. The high surface Fe^{2+} ion concentration and pH that have been predicted in this study would cause the formation of film. For example, in the Fe-H_2O system, $Fe(OH)_2$ precipitation might occur:

$$Fe^{2+} + 2OH^- \Leftrightarrow Fe(OH)_2 \downarrow \qquad (6\text{-}15)$$

The Pourbaix potential-pH diagram (Pourbaix, 1966) for Fe-H_2O system shows that in the predicted corrosion potential ranged from -0.39 V to -0.44 V the point with the predicted surface pH=10.7 is in the stable zone of solid $Fe(OH)_2$ while the point with bulk pH=6 falls in the stable zone of Fe^{2+}. The formation of the surface film will complicate the determination of the surface Fe^{2+} concentration and pH value which will depend on the properties of the film (thickness, compactness, and film diffusion coefficient).

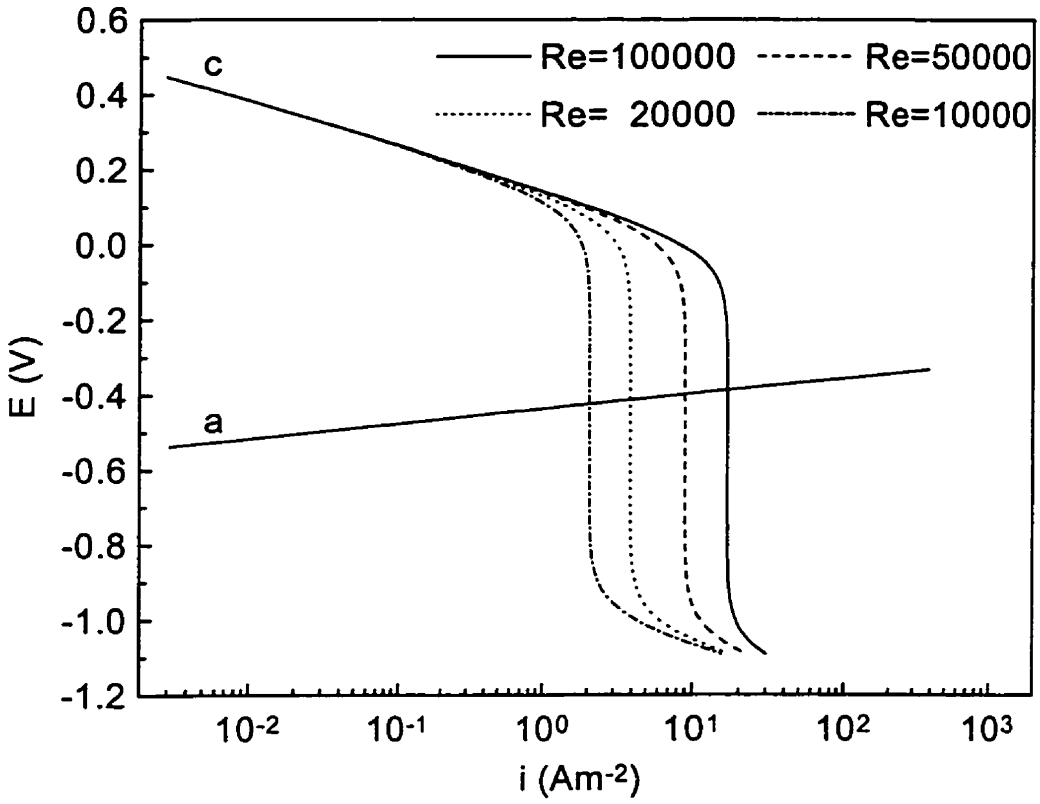

Fig. 6-18 Effect of Reynolds number on E/logi curves in fully developed region; a: anodic iron dissolution, c: oxygen reduction with water reduction included at more negative potential (E<-0.9 V); bulk pH=6, bulk $[O_2]$=8 PPM.

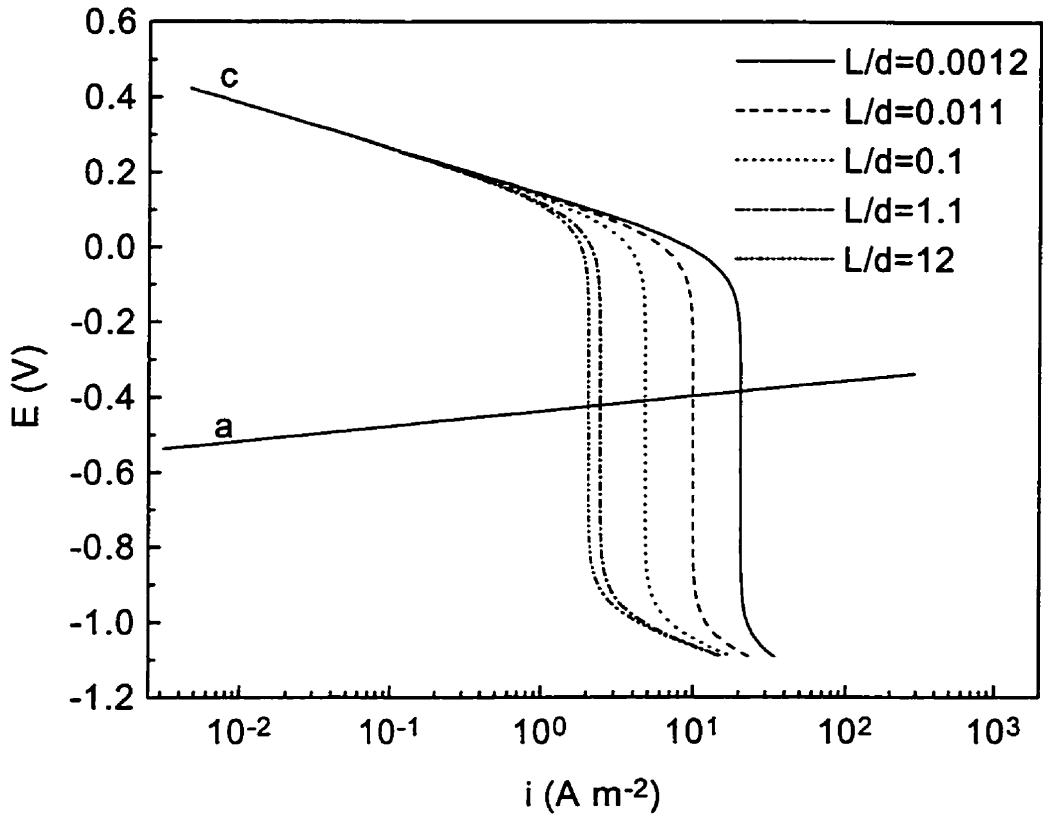

Fig. 6-19 Effect of the mass transfer entrance on E/logi curves; a: anodic iron dissolution, c: oxygen reduction with water reduction included at more negative potential (E<-0.9 V); Re=10^4, bulk pH=6, bulk [O_2]=8 PPM.

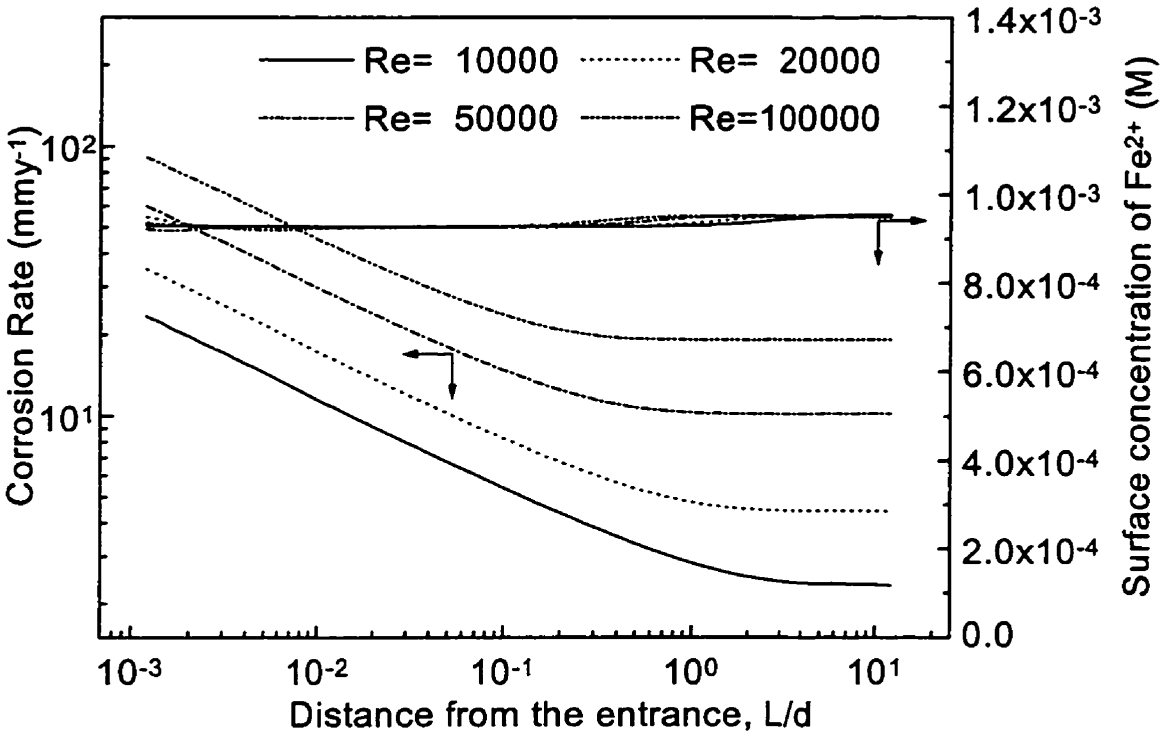

Fig. 6-20 Corrosion rate and surface concentration of dissolved Fe^{2+} ion as a function of the distance from the leading edge of the mass transfer entrance at various Reynolds numbers; bulk pH=6, bulk $[O_2]$=8 PPM.

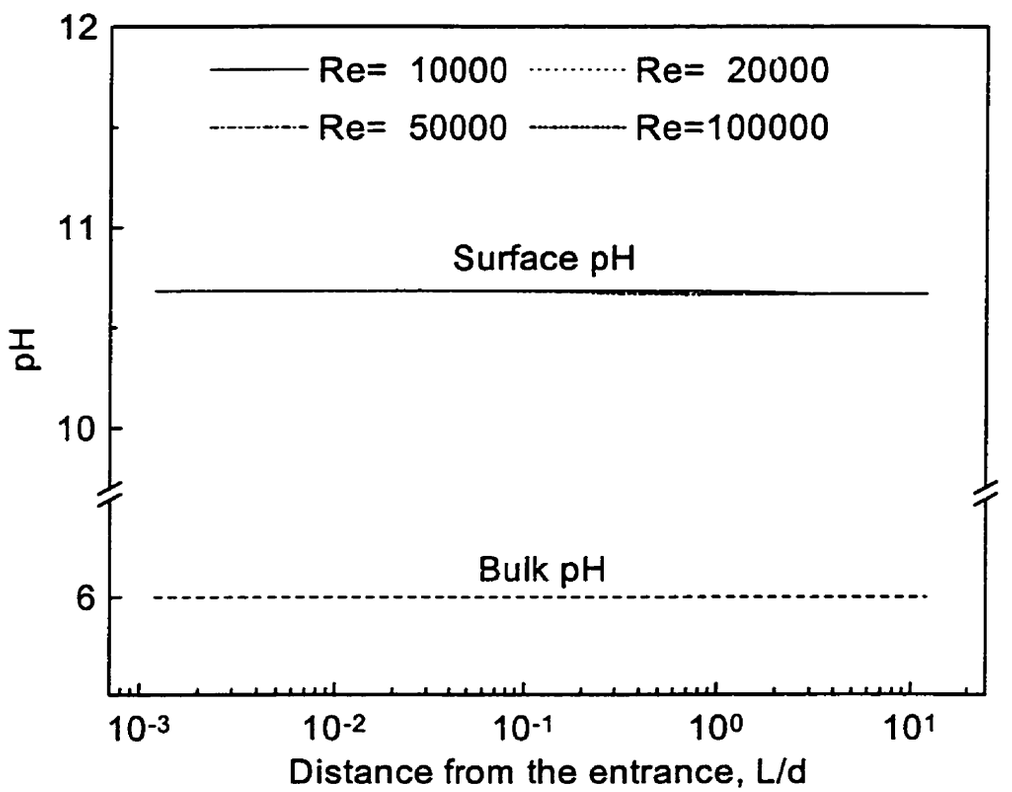

Fig. 6-21 Surface pH as a function of the distance from the mass transfer entrance at various Reynolds numbers; bulk pH=6, bulk $[O_2]$=8 PPM.

:r

:ed Charge/Mass Transfer Control

es have shown that the corrosion of copper [illegible] f dissolved metal ions or complex ions from [illegible] lling in the range where oxygen reduction i[illegible] 1975). Fig. 6-22 and Fig. 6-23 illustrate [illegible] showing the anodic dissolution under mi[illegible] ie oxygen reduction under charge transfer co[illegible]

's the corrosion rate and surface cupric io[illegible] e from the leading edge of mass transfer ent[illegible] The corrosion rate increases with rising l[illegible] ass transfer entrance length. The influence [illegible] small with the corrosion rate increasing [illegible] lds number. This can be contrasted with [illegible] n mass transfer control (Fig. 6-20) where t[illegible] $e^{0.9}$ in fully developed conditions.

l ion concentration decreases with increasi[illegible] e entrance length. This contrasts the mas[illegible] on (Fig. 6-20) where $[Fe^{2+}]_s - [Fe^{2+}]_b$ was [illegible] id the position in the entrance length. It is [illegible]

6.3.3. Copper

6.3.3.1.Mixed Charge/Mass Transfer Control

Previous studies have shown that the corrosion of copper is partially controlled by the mass transport of dissolved metal ions or complex ions from the surface to the bulk solution with E_{corr} falling in the range where oxygen reduction is under charge transfer control (Faita et al, 1975). Fig. 6-22 and Fig. 6-23 illustrate this situation with the corrosion diagrams showing the anodic dissolution under mixed charge and mass transfer control and the oxygen reduction under charge transfer control at E_{corr}.

Fig. 6-24 shows the corrosion rate and surface cupric ion concentration as a function of the distance from the leading edge of mass transfer entrance region at various Reynolds numbers. The corrosion rate increases with rising Reynolds number and decreases along the mass transfer entrance length. The influence of mass transfer on the corrosion rates is only small with the corrosion rate increasing by 1.22 for a tenfold increase in the Reynolds number. This can be contrasted with the behavior of iron corroding under oxygen mass transfer control (Fig. 6-20) where the corrosion rate was proportional to about $Re^{0.9}$ in fully developed conditions.

The surface metal ion concentration decreases with increasing Reynolds number and increases along the entrance length. This contrasts the mass transfer controlled behavior of iron corrosion (Fig. 6-20) where $[Fe^{2+}]_s - [Fe^{2+}]_b$ was independent of both the Reynolds number and the position in the entrance length. It is noted from equation

(6-8) that the metal/solution interface concentration depends on both corrosion rate and the mass transport rate of dissolved metal ion. However unlike the case with iron discussed above the corrosion rate is much less sensitive to the Reynolds number than the rate of transfer of dissolved metal ions to the bulk solution and $[Cu^{2+}]_s - [Cu^{2+}]_b \propto 1/\mathrm{Re}^{0.9}$ for fully developed mass transfer.

The predicted surface pH in the mass transfer entrance and fully developed regions for various Reynolds numbers are shown in Fig. 6-25. For each Reynolds number, the pH value is the lowest at the leading edge and increases along the mass transfer entrance length, approaching a stable value in fully developed region. The surface pH decreases with rising Reynolds number in both the entrance and fully developed region. Again the reason for the different behavior to that shown for iron in Fig. 6-21 lies in the fact that the corrosion rate is relatively insensitive to mass transfer.

From Fig. 6-24 and Fig. 6-25 we can see that the surface metal ion concentration and surface pH at the leading edge are much lower than that in the remaining region. Therefore film formation will be less likely at the leading edge than in the remaining region.

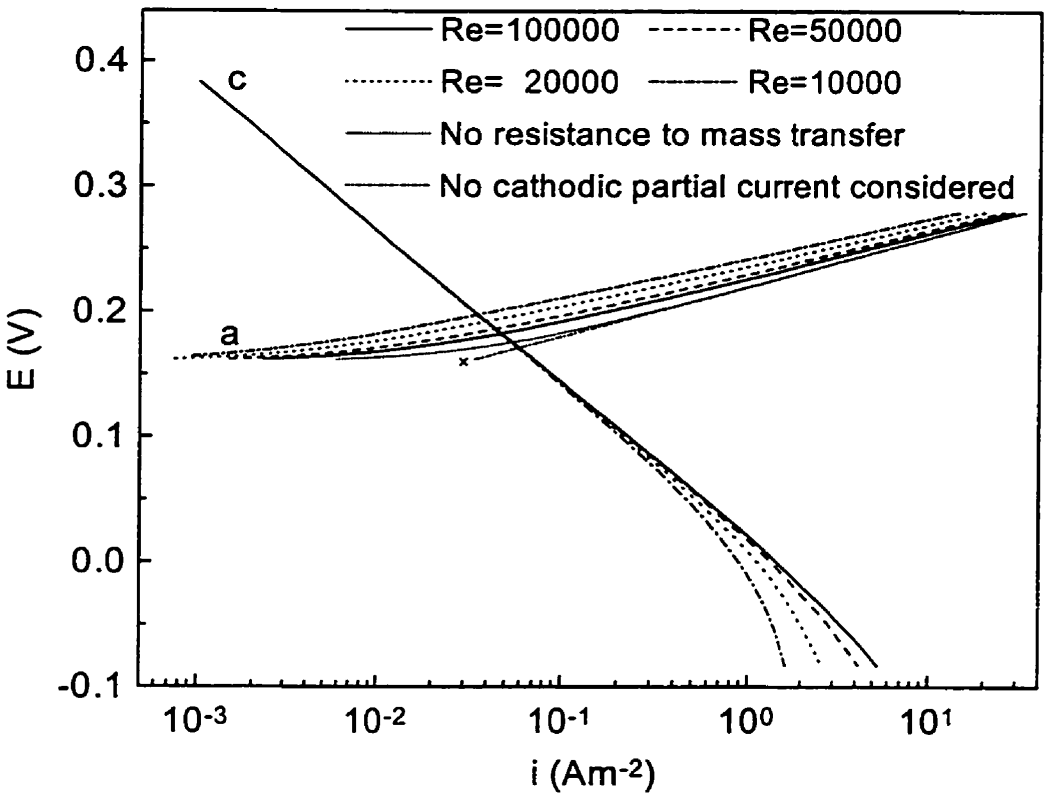

Fig. 6-22 Effect of Reynolds number on E/logi curves in fully developed region; a: anodic copper dissolution, c: oxygen reduction; bulk pH=6, bulk $[O_2]$=8 PPM.

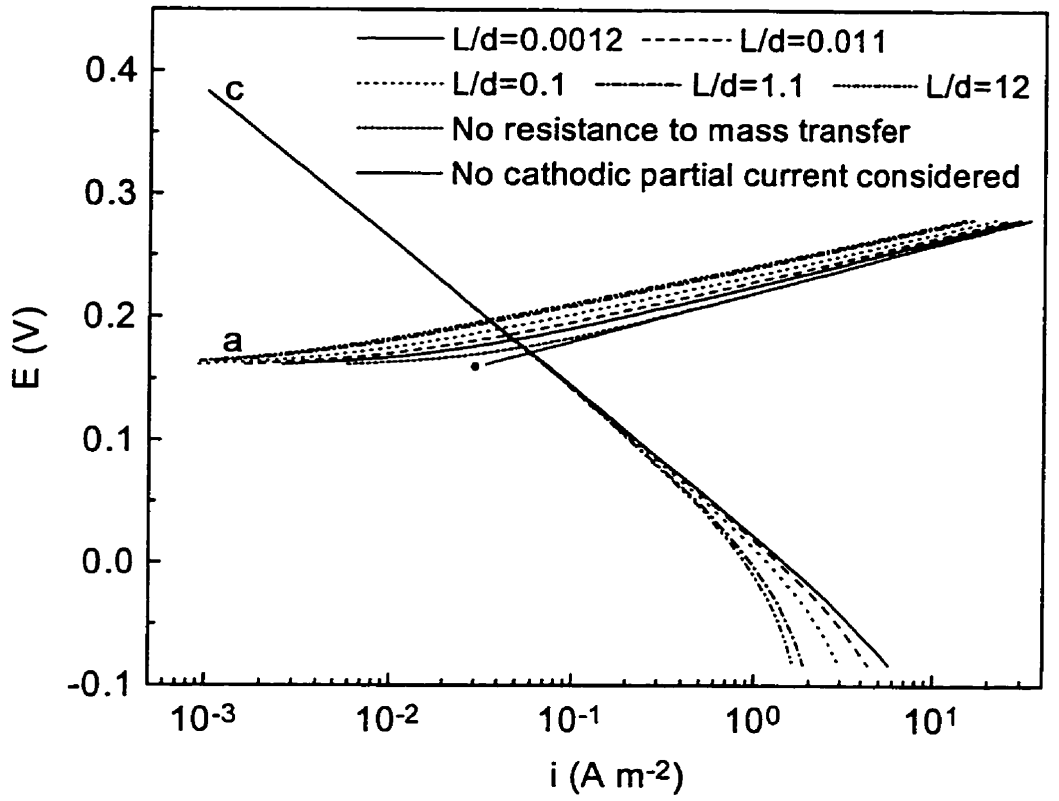

Fig. 6-23 Effect of the mass transfer entrance on E/logi curves; a: anodic copper dissolution, c: oxygen reduction; Re=10^4, bulk pH=6, bulk [O_2]=8 PPM.

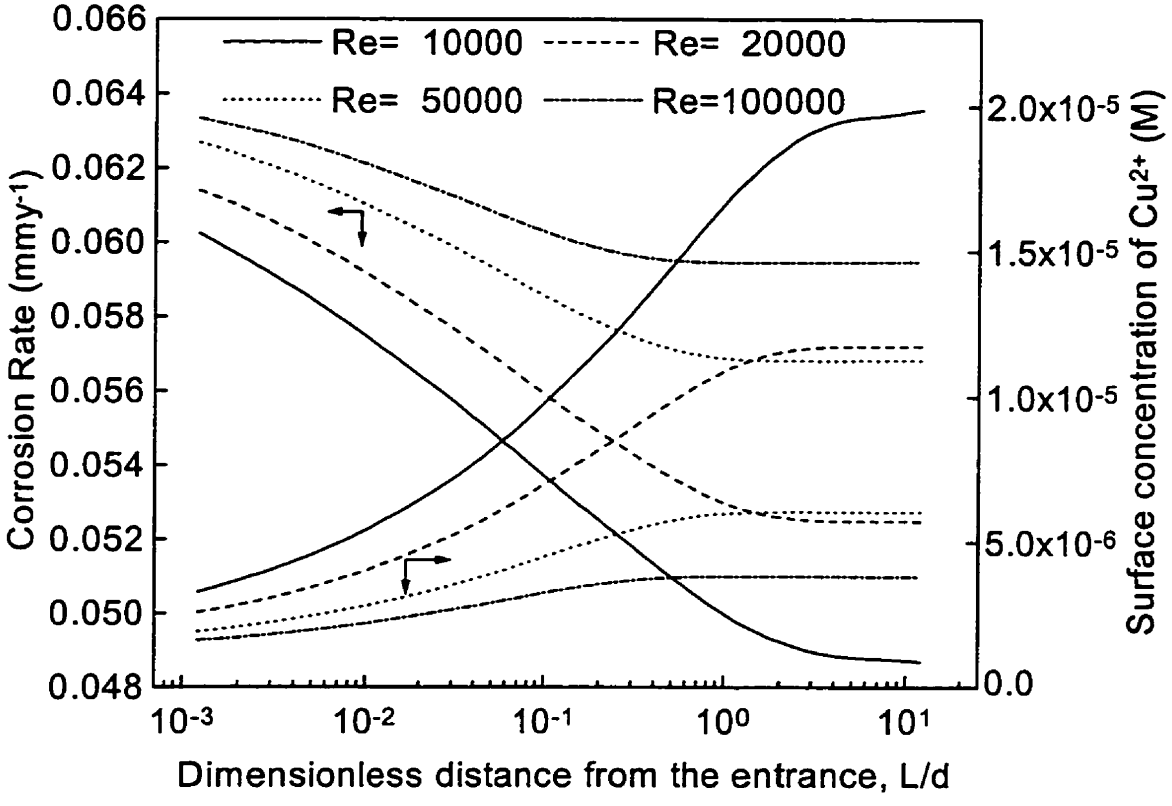

Fig. 6-24 Corrosion rate and surface concentration of dissolved Cu^{2+} ion as a function of the distance from the leading edge of the mass transfer entrance region at various Reynolds numbers; bulk pH=6, bulk $[O_2]$=8 PPM.

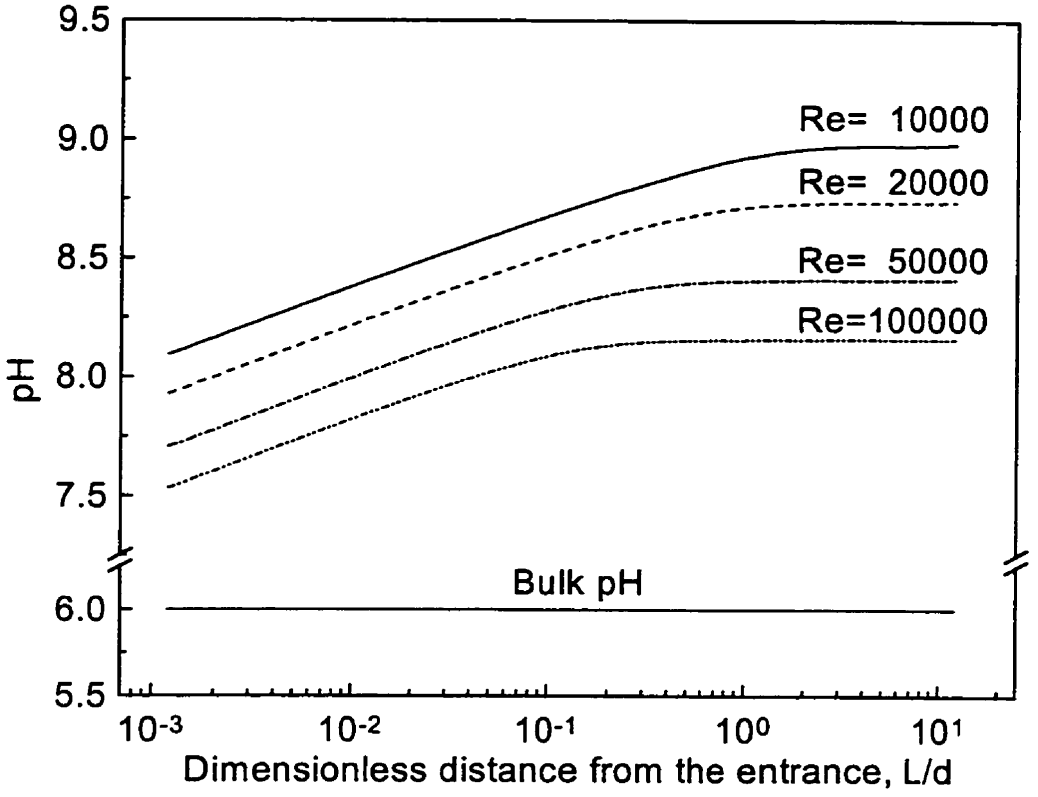

Fig. 6-25 Surface pH as a function of the distance from the mass transfer entrance at various Reynolds numbers; bulk pH=6, bulk $[O_2]$=8 PPM.

6.4. Application to the Prediction of Electrode Misalignment Effect on Electrochemical Corrosion Rate Measurement

6.4.1. Introduction

Corrosion rate measurements are often accomplished by the application of electrochemical techniques with tubular or other shape of working electrode installed into an experimental or operating pipeline. Two problems arise relating to mass transfer effects at the working electrode. Despite attempts to make the working electrode flush with the pipe wall, a small misalignment often occurs during installation with the electrode protruding or lying slightly below the pipe wall. Even if initially perfectly flush, corrosion may lead to non-flush conditions. However caused, the electrode misalignment leads to flow disturbances which affect the rate of mass transfer of reactants and corrosion products between the corroding surface and the bulk solution.

The second problem relates to the mass transfer entrance effect. Even if the working electrode is completely flush with the pipe wall there will be enhanced rates of mass transfer at the leading section of electrode where the mass transfer boundary layer is developing. In turbulent-pipe-flow corrosion experiments hydrodynamic entry lengths of the order of 60~100 pipe diameters (Postlethwaite et al, 1986; Berger and Hau, 1977) ensure that a fully developed hydrodynamic boundary layers is established upstream of the working electrode. The mass transfer boundary layer at the working electrode develops within a fully developed hydrodynamic boundary layer. Working electrodes l

mm to 20 mm in length have been used (Efird et al, 1993; Eriksrud and Sontvedt, 1983; Nesic et al, 1995), which would give overall mass transfer rates that are higher than the fully developed rates. In some studies working electrodes of an appropriate length to minimize the entrance effect have been used (Postlethwaite et al, 1986; Postlethwaite, 1979; Postlethwaite and Lotz, 1988; Postlethwaite et al, 1978).

In this part of the study, the low Reynolds number k-ε turbulence model has been used to determine the simultaneous electrode-misalignment and mass-transfer-entry-length effects on the local and overall mass transfer rates at the working electrode. The predicted deviation or "error" is the difference between the calculated corrosion rate that includes electrode-misalignment and mass-transfer-entrance-length effects, and that calculated for fully developed mass transfer conditions with a perfectly flush electrode. Since the predicted measurement error depends on the extent to which the corrosion rate is controlled by the mass transfer component, three situations are considered: the corrosion is under mass transfer control; the corrosion is under charge transfer control; and the corrosion is under mixed charge transfer and mass transfer control. The corrosion rate under charge transfer control would not be expected to be affected directly by mass transfer but could be affected by film formation which is directly related to the surface conditions.

The surface concentration profiles of metal ions and surface pH profiles along the working electrode are discussed in terms of their possible effect on film formation at the working electrode surface for all three cases.

6.4.2. Computational Domain

The schematic flow cell and computational domain of 360 mm × 12.5 mm** are shown in Fig. 6-26. Tubular electrodes 5 to 60 mm in axial length were assumed to be installed in a pipe with internal diameter of 25 mm. The electrodes are either protruding or recessed 10 to 500 μm from the pipe wall respectively. The Reynolds number used is 5×10^4 and solution pH is assumed to be 6. Since the mass transfer boundary layer is very thin the side edge effect is very small and the results would apply to rectangular electrodes (cut from pipe) which have certain advantages: they can be readily smoothed after installation to give a very flush fit; the counter electrode can be positioned on the opposite side of the cell giving a more symmetrical electrode arrangement (Postlethwaite et al, 1986; Berger and Hau, 1977).

Again in this part of the study, iron was chosen to represent metals with a low exchange current density and copper those whose anodic dissolution is more reversible. Non-uniform staggered grids ((100~140)×(40~70)) were used in the computational domain, with the majority of nodes concentrated in the near-wall region and in both end regions of working electrode. The first near-wall node was placed at y=1μm so that $y^+ \leq$ 0.1, and the first node close to the leading edge of the working electrode was placed at x=2 μm. In the present studies changes in electrode thickness following corrosion are ignored.

** In the case of electrode lying 10 to 500 μm below the pipewall, the computational domain of 360 mm × (12.51 to 13.0) mm were used.

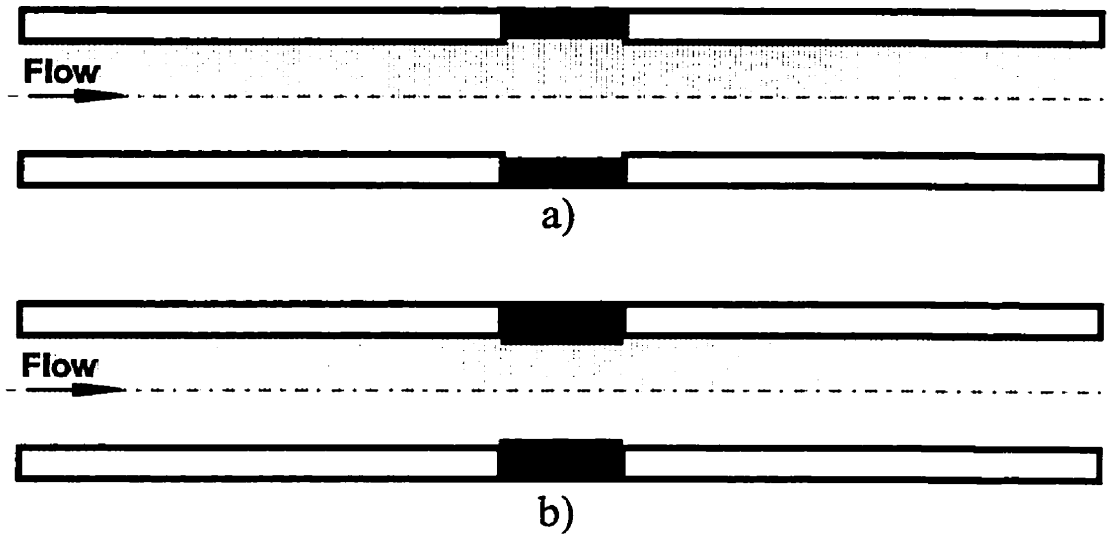

Fig. 6-26 Computational domain (360 mm × 12.5 mm). a) working electrode recessed from pipewall; b) working electrode protruding from pipewall; fully developed flow at inlet; pipe diameter: 25 mm; electrode length 5 to 60 mm.

(pipe wall working electrode computational domain)

6.4.3. Corrosion under Mass Transfer Control

6.4.3.1.Mass Transfer Rate Profiles

In most corrosion rate measurements in pipe flow the electrodes are fitted into either non-metallic or non-corroding metallic pipes, giving a mass-transfer-entry-length, with high rates of mass transfer, on the working electrode where the reactant (e.g. O_2) and product (e.g. Fe^{2+}) concentration boundary layers are developing. In addition any electrode misalignment will cause disturbed flow conditions at electrode surface which will also affect the mass transfer rates.

The predicted oxygen mass transfer rate profiles, for oxygen, for recessed (Fig. 6-27) and protruding electrodes (Fig. 6-28), take into account both entrance and misalignment effects. In both cases the mass transfer rate profiles are similar over the greater length of the electrodes. The results are for step sizes up to 50 μm which exceeds the tolerance which can be readily achieved in practice. The results deviate substantially for very short distances at the steps at the leading edge of the electrodes; with small deviations at the steps at the downstream edge of the electrodes. The step at the leading edge of the recessed electrode, (Fig. 6-27) results in a substantial reduction in the mass transfer rates at $x < 0.2$ mm. This is a region where the concentration boundary layer normally develops very rapidly as seen by the mass transfer rates with the flush electrode. The dead zone associated with the leading edge of the recessed electrode is responsible for the reduction in the mass transfer rates. In contrast the step at the protruding electrode results in a flow disturbance that enhances the mass transfer at the

leading edge. It should be mentioned here that the mass transfer to both forward facing and backward facing sides was not included in the case of protruding electrode (Fig. 6-26b). Since the area on both sides are extremely small compared to electrode area, such a treatment would not pose significant error.

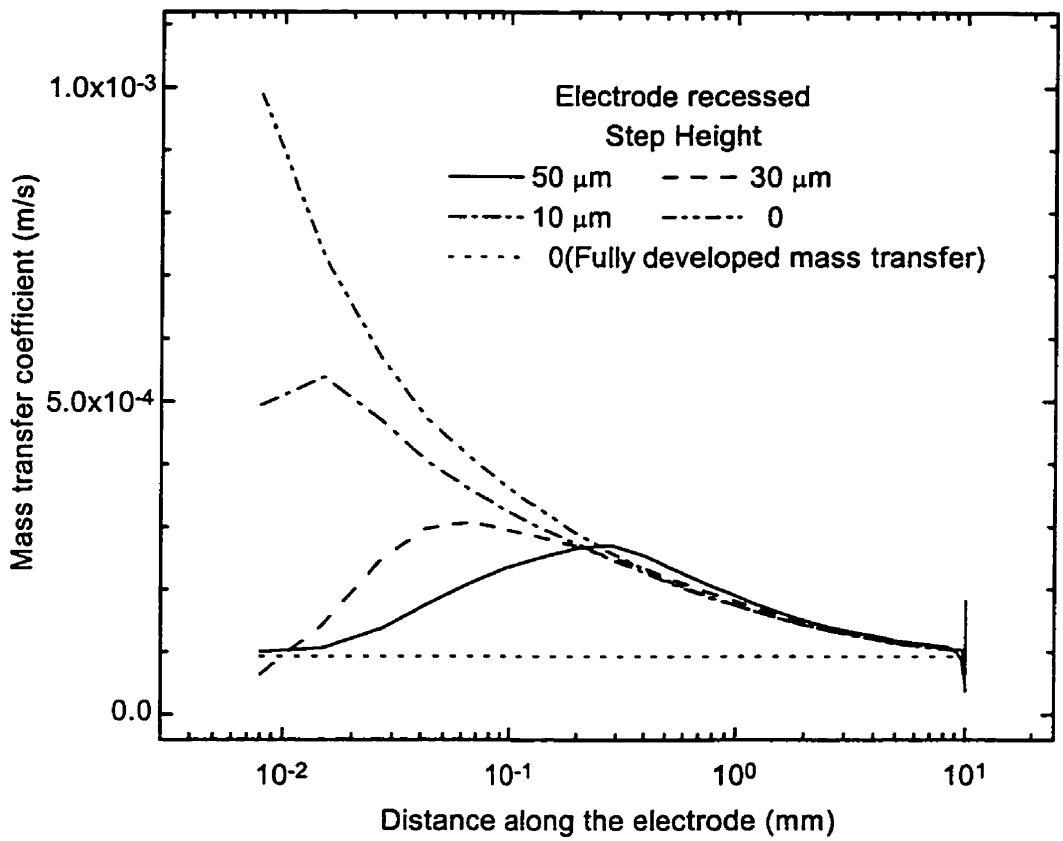

Fig. 6-27 Mass transfer rate profiles for oxygen along the pipewall working electrode for recessed electrodes; entrance effect considered, d=25 mm, electrode length 10 mm, $Re=5\times10^4$.

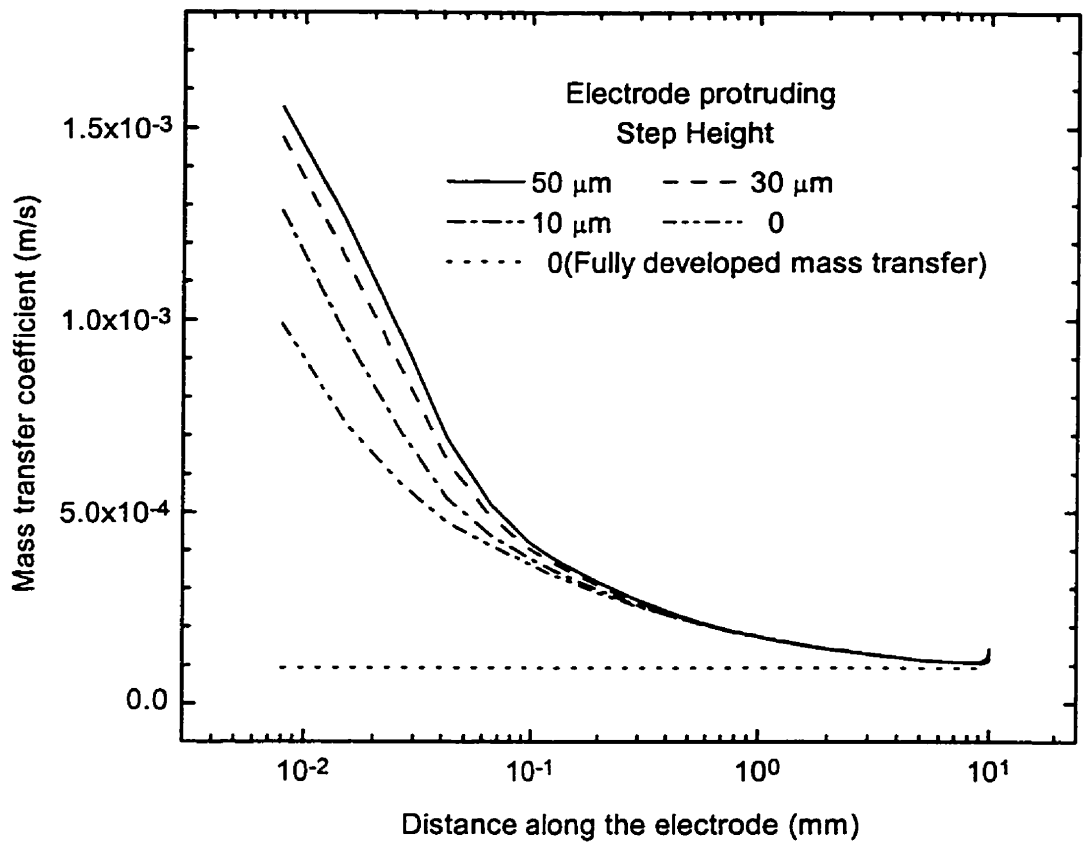

Fig. 6-28 Mass transfer rate profiles for oxygen along the working electrode for electrodes protruding from the pipewall; entrance effect considered, d=25 mm, electrode length 10 mm, Re=5×10^4.

6.4.3.2.Predicted Measurement Error

The predicted measurement errors caused by the superposition of both misalignment and mass transfer entrance effects are given in Fig. 6-29 as a function of step height. The measurement error is the error that would be obtained in a mass transfer measurement using the limiting diffusion current technique. The same error would be obtained in a corrosion rate measurement using the polarization resistance method, if the corrosion were under oxygen mass transfer control. Also shown in Fig. 6-29 are the measurement errors caused by electrode misalignment in the absence of an entry effect. In the latter case fully developed mass transfer was assumed at the beginning of the computational zone. It is implied from Fig. 6-29 that if a maximum 10% measurement error caused by electrode misalignment is permissible in electrochemical measurements, the step size for either electrode protrusion or recession should be less than 20 μm.

The results in Fig. 6-29 are for a 10 mm long electrode with step sizes up to 500 μm in order to illustrate the effects of much larger misalignments than the much smaller values readily achievable in practice. For protruding electrodes, with the entry length taken into account, the predicted measurement error varies from 43% for a flush electrode to 86% at a step height of 500 μm. The predicted misalignment error reached 83% for protruding electrodes at the 500μm step height. The predicted measurement errors reached maximum values, 60% and 57%, for recessed electrodes at the step height of 350 μm, with and without the entry length taken into account respectively. The

reduction of the entrance effect on the overall corrosion rates by the use of longer electrodes is discussed later.

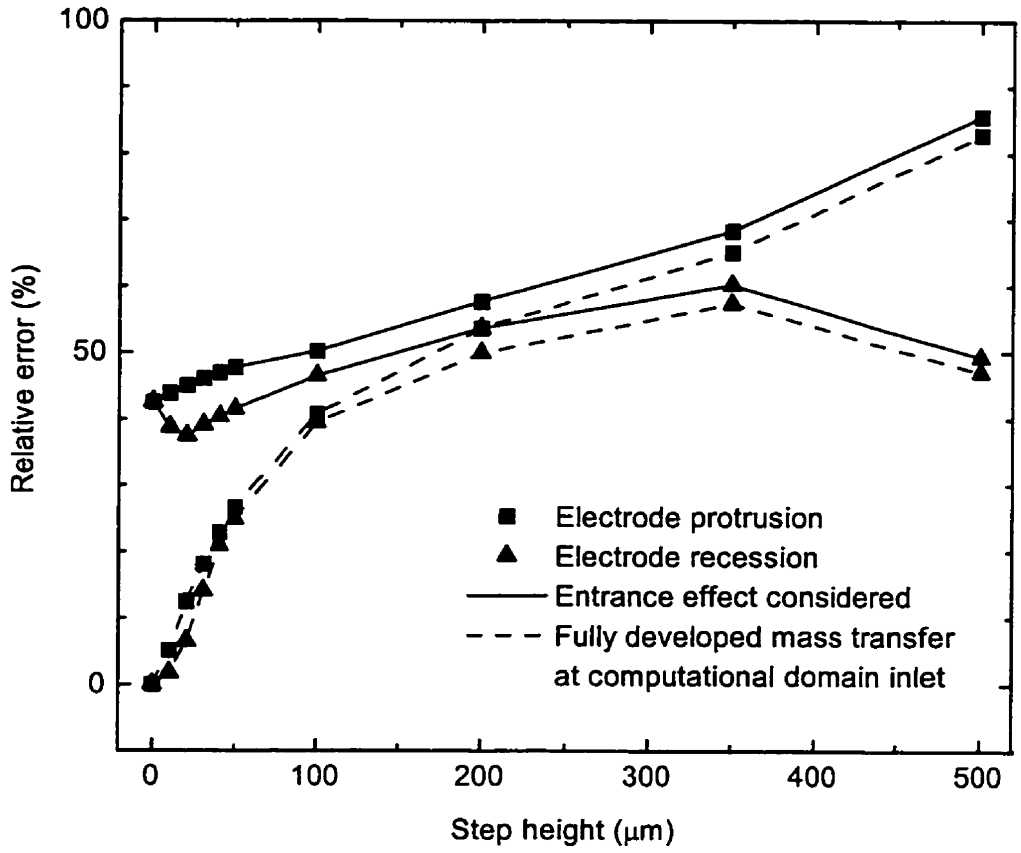

Fig. 6-29 Predicted measurement error as a function of step height for recessed and protruding electrodes; d=25 mm, electrode length 10 mm, Re=5×10^4.

6.4.3.3.Surface Metal Ion Concentration and pH Value

The simulation results in section 6.3 have shown that if the corrosion is controlled by the mass transport of O_2 to the metal surface, the surface concentration of dissolved metal ion does not vary with the distance from the mass transfer entrance and the Reynolds number.

The predicted corrosion rate and surface Fe^{2+} ion concentration for oxygen mass transfer controlled corrosion along the surface of iron electrodes recessed or protruding 50 μm from pipe wall are shown in Fig. 6-30. Although the corrosion rates are non-uniform on the working electrode surface, the surface Fe^{2+} ion varies very little along the working electrodes compared to the several orders of magnitude difference between surface and bulk Fe^{2+} ion concentration. Recall that when corrosion is under O_2 mass transfer control, the interfacial ferrous ion concentration can be calculated by the following equation:

$$[Fe^{2+}]_s = \frac{i_{corr}}{zFK_{Fe^{2+}}} + [Fe^{2+}]_b \qquad (6\text{-}10)$$

where the bulk oxygen concentration $[O_2]_b$ is constant (8 PPM). It has been confirmed that the ratio of the mass transfer coefficient of O_2 to that of Fe^{2+}, ($K_{O_2}/K_{Fe^{2+}}$), is constant in the entrance and fully developed regions (see 6.3.2.2). Based on present numerical predictions, this ratio ($K_{O_2}/K_{Fe^{2+}}$) is also almost constant across the working electrodes, whether recessed or protruding from the pipe wall.

The predicted surface pH profiles, (Fig. 6-31), show that there is no effect of the electrode-misalignment and the mass-transfer-entry-length on surface pH values when the corrosion process is controlled by the transport of oxygen to the metal surface. The explanation for the lack of change of the surface concentration for dissolved metal ions also applies to the surface pH value.

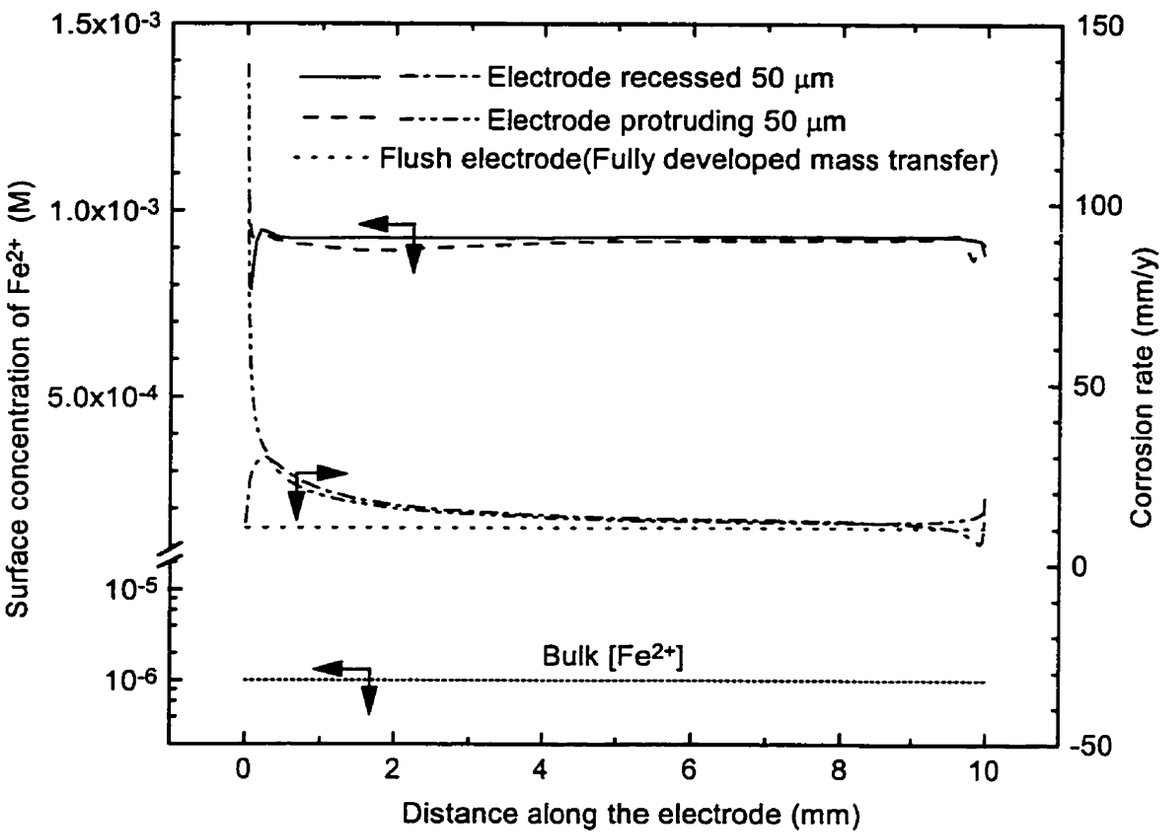

Fig. 6-30 Predicted surface Fe^{2+} concentration and corrosion rate profiles along the surface of working electrodes recessed and protruding 50 μm from pipewall; d=25 mm, electrode length 10 mm, $Re=5\times10^4$.

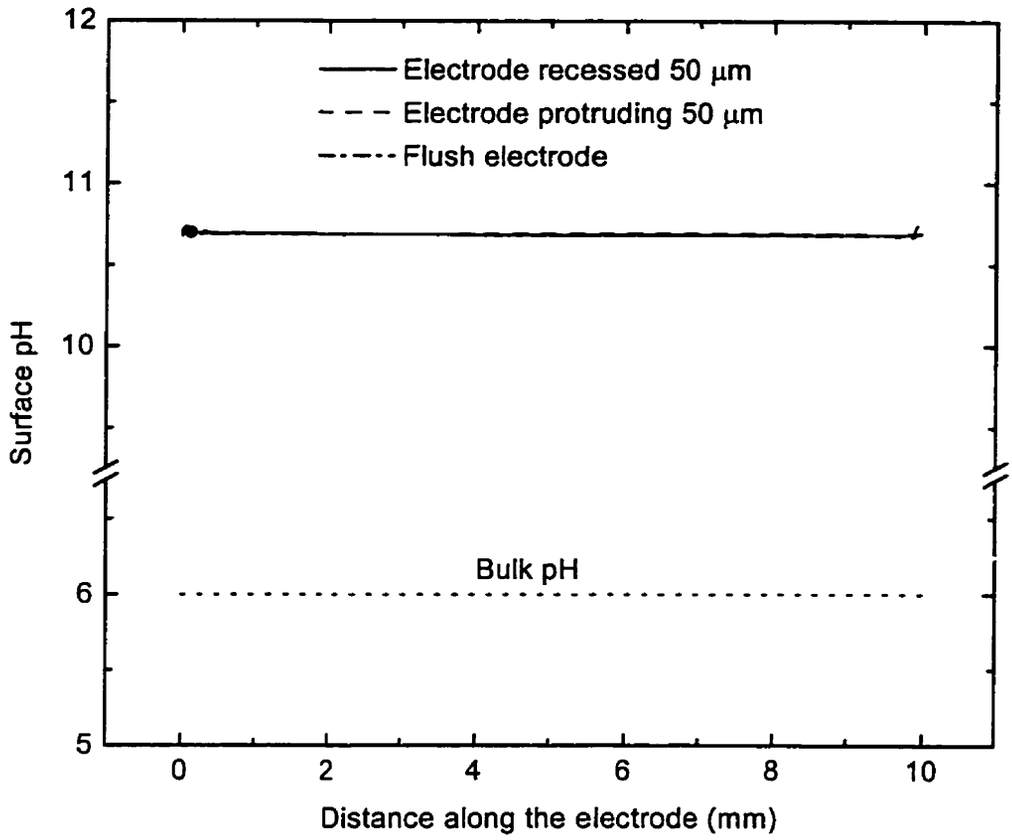

Fig. 6-31 Predicted surface pH profiles along the surface of working electrodes recessed and protruding 50 μm from pipewall; d=25 mm, electrode length 10 mm, Re=5×10^4.

6.4.4. Corrosion under Charge Transfer Control

In the case when corrosion is under charge transfer control, the corrosion rate is constant along the working electrode. As expected in the mass transfer entry length, the surface Fe^{2+} ion concentration increases along the length of the mass transfer section, approaching a stable value in fully developed conditions (Fig. 6-32). The behaviour with misaligned electrodes (Fig. 6-32) is similar to that for the mass-transfer-entry-length over most of the electrode; with the concentration rising along the electrode length. There are major differences relating to the steps at the beginning and end of the electrode, which can be explained by the mass transfer coefficient variations shown in Fig. 6-27 and Fig. 6-28. For the protruding electrode, the surface concentration for Fe^{2+} ion is the lowest at the leading edge of the working electrode, increasing and approaching the fully developed value along the electrode until the region close to the end of the electrode where the surface Fe^{2+} ion concentration decreases with the rise in the mass transfer coefficient. The dead zones with the recessed electrode result in high Fe^{2+} ion concentrations over short distances at the beginning and end of the electrode.

There will be no measurement error caused by the electrode-misalignment and/or the mass-transfer-entry-length since the corrosion is wholly under charge transfer control. However, the non-uniform surface concentration profile for dissolved metal ion at the electrode surface will produce non-uniform film formation conditions when film formation is possible and could effect the corrosion rates.

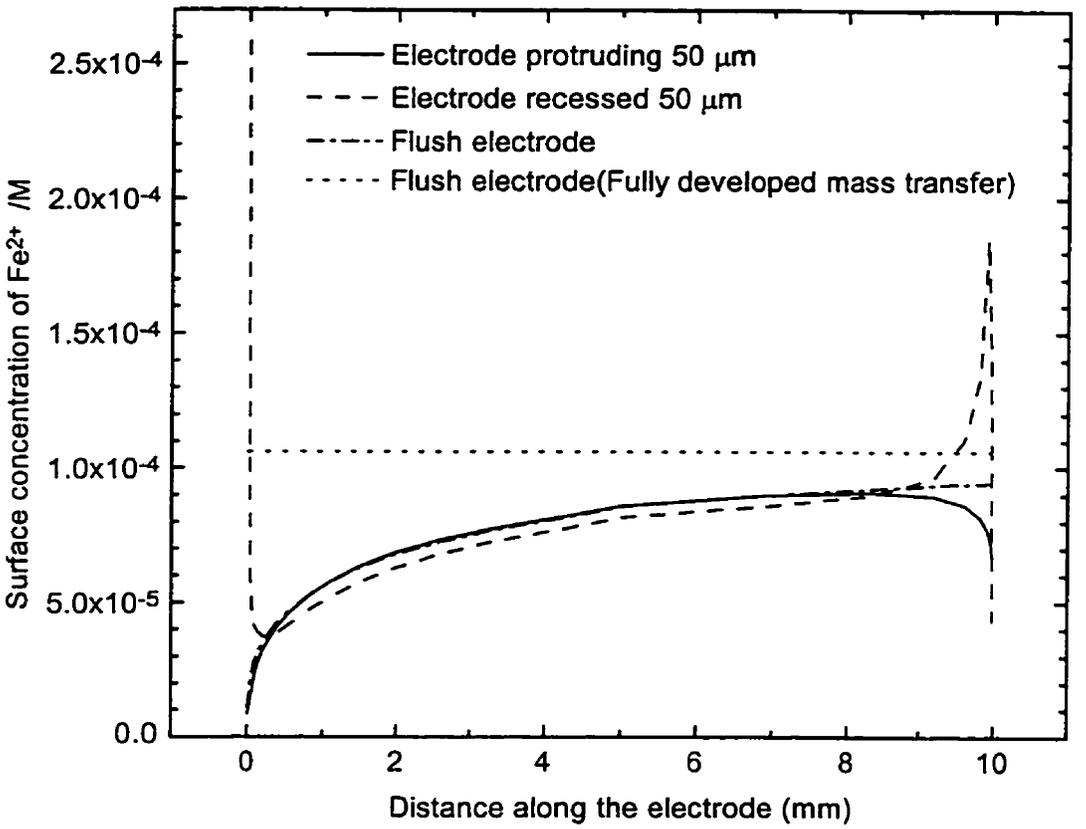

Fig. 6-32 Predicted surface Fe^{2+} concentration profiles along the surface of working electrodes recessed and protruding 50 μm from pipewall; corrosion under charge transfer control; corrosion rate 1 A/m^2; d=25 mm, electrode length 10 mm, $Re=5\times10^4$.

6.4.5. Corrosion under Mixed Control

Copper corrosion with oxygen reduction in neutral solutions has been selected as an example of corrosion under mixed charge and mass transfer control, since previous studies have shown that the corrosion of copper is partially controlled by the mass transport of dissolved metal ions or complex ions from the surface to the bulk solution with E_{corr} falling in the range where oxygen reduction is under charge transfer control (Faita et al, 1975). The rate equation (5-8) for the anodic dissolution of copper taking into account the effect of mass transfer was based on the mechanism proposed by Mattsson and Bockris (1959). The predicted corrosion rates for recessed and protruding electrodes are shown in Fig. 6-33 and Fig. 6-34. Corrosion rates were determined from kinetic corrosion diagrams constructed on the basis of the rate equations for oxygen reduction (5-13) and copper dissolution (5-10) with i_0 values of 10^{-9} and 0.03 A/m^2 respectively. The predictions show that the influence of mass transfer on the corrosion rate, for the particular case under study, is small. Over most of the electrode length very small differences are observed with differences due to the electrode-misalignment and mass transfer entry length of < 15% observed at the electrode ends. The difference in mean corrosion rate between the electrode protruding 50 μm from pipewall and one under fully developed mass transfer conditions is less than 3% for the 10 mm long electrode. This can be contrasted with the behaviour of iron corroding under oxygen mass transfer control (Fig. 6-29) where the measurement error was about 48% for a 10 mm long electrode.

The surface Cu^{2+} ion concentration profiles along the working electrode recessed and protruding 50 μm from pipe wall are shown in Fig. 6-35 along with the profile for a flush electrode and one under fully developed mass transfer. The concentrations are similar for most of the electrode length with differences relating to the misalignment and disturbed flow at the electrode ends. This contrasts the mass transfer controlled behaviour of iron corrosion (Fig. 6-30) where the surface Fe^{2+} concentration was independent of the position on working electrode for both flush and misaligned electrodes. It is noted from equation (6-8) that the surface concentration for dissolved metal ion depends on both the corrosion rate and the mass transport rate of dissolved metal ion. The corrosion rate in the case of the partial mass transfer control of copper corrosion is much less sensitive to mass transfer effects than the transport rate of dissolved metal ions to the bulk solution.

The predicted surface pH values along the working electrode recessed, protruding 50 μm from pipe wall are shown in Fig. 6-36. There is a small effect of mass transfer, which increases at the electrode ends. The small variations in pH again reflects the relative lack of sensitivity of the corrosion in the chosen case to mass transfer.

From Fig. 6-35 and Fig. 6-36 it can be seen that for protruding electrode, the surface metal ion concentration and surface pH are lower at both ends of the electrode, making film formation less likely. For the recessed electrode, the surface metal ion concentrations and surface pH in the dead water zones close to the steps are higher than that in the remaining region, and film formation will be more likely at these locations.

The important thing to note is that the mass transfer effects relating to mass-transfer-entry-length and electrode-misalignment with partial mass transfer control can be simulated enabling improved design of the flow cells for the determination of corrosion rates.

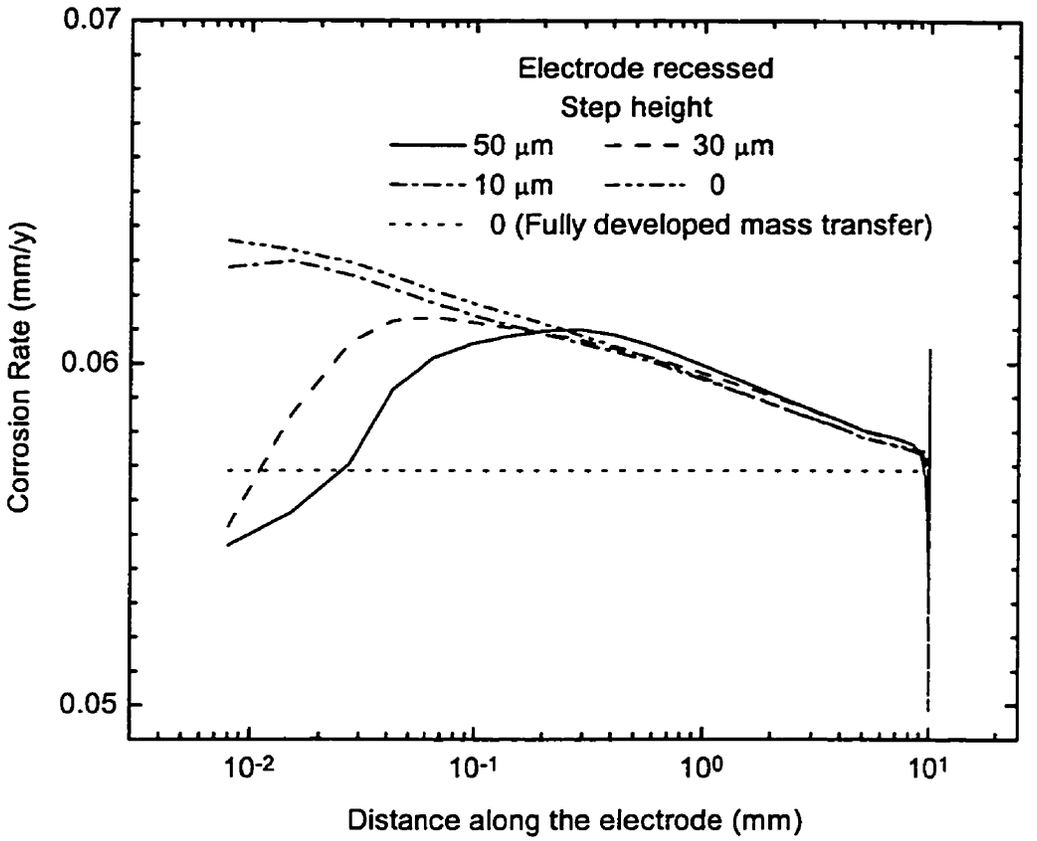

Fig. 6-33 Predicted corrosion rate profiles for copper along the working electrode for electrodes lying below the pipewall; entrance effect considered, d=25 mm, electrode length 10 mm, Re=5×10^4.

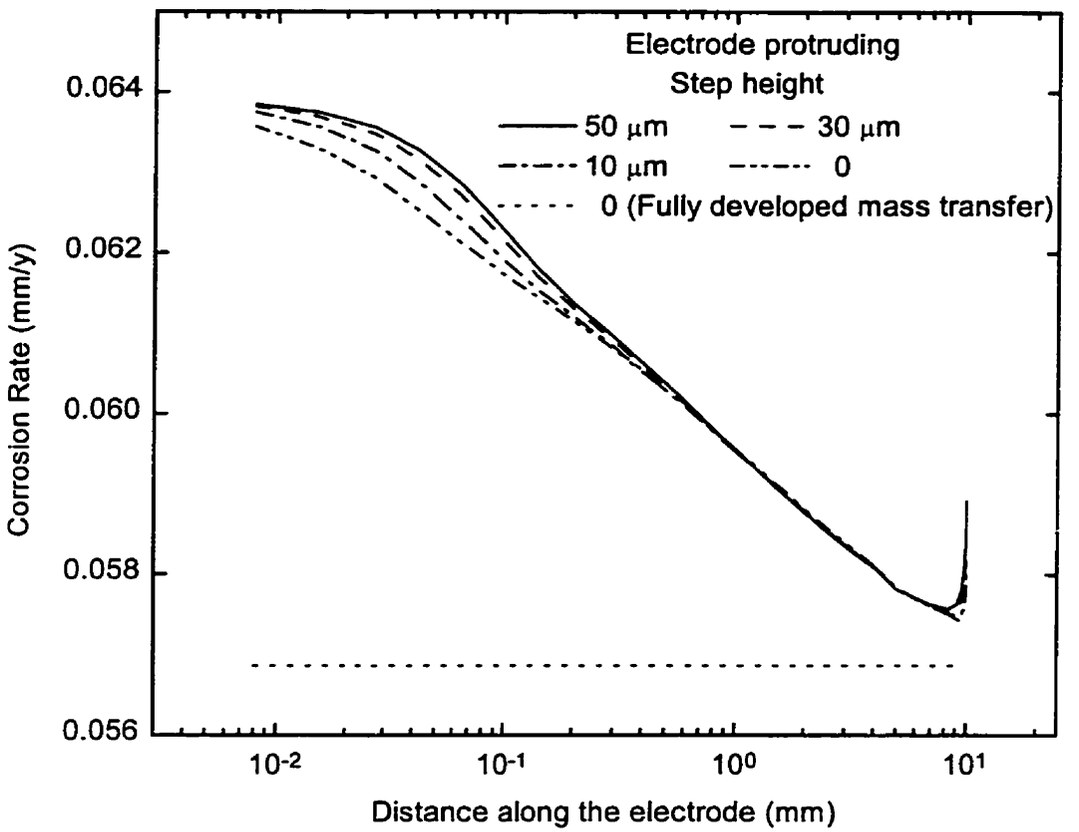

Fig. 6-34 Predicted corrosion rate profiles for copper along the working electrode for electrodes protruding from the pipewall; entrance effect considered, d=25 mm, electrode length 10 mm, Re=5×10^4.

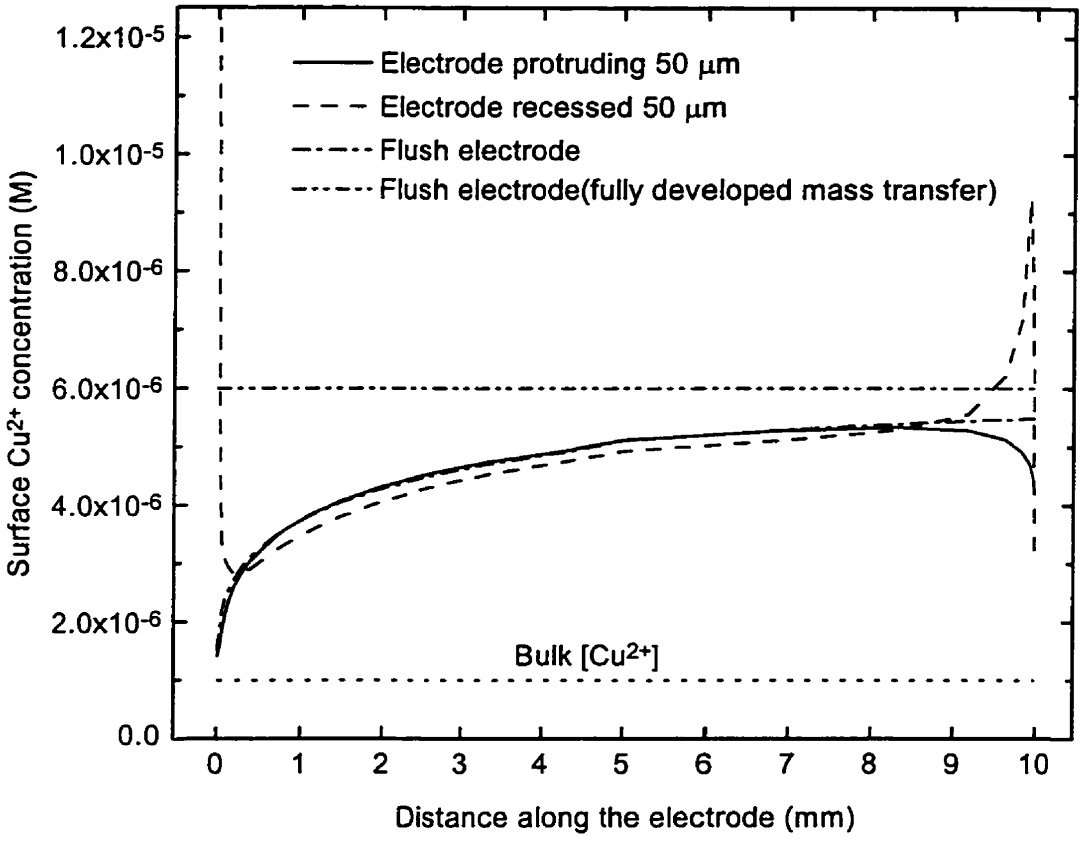

Fig. 6-35 Predicted surface Cu^{2+} concentration profiles along the surface of working electrodes recessed and protruding 50 μm from the pipewall; corrosion under mixed control; d=25 mm, electrode length 10 mm, $Re=5\times10^4$.

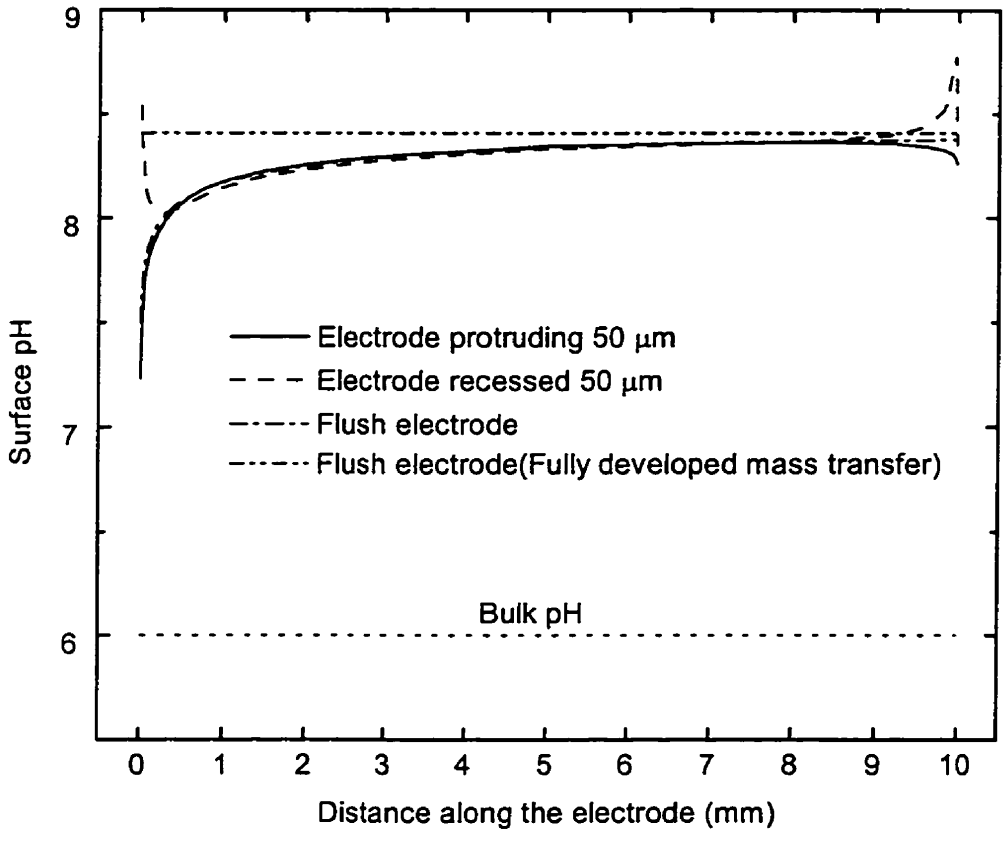

Fig. 6-36 Predicted surface pH profiles along the surface of working electrodes recessed and protruding 50 μm from the pipewall; corrosion under mixed control, d=25 mm, electrode length 10 mm, $Re=5\times10^4$.

6.4.6. Reduction of Measurement Error

6.4.6.1. Using Longer Electrode

The effect of electrode length on the measurement error for oxygen mass transfer controlled corrosion with misalignments <50 μm are given in Fig. 6-37. Errors <10% can be achieved with an L/d ratio of 2.4 for a perfectly flush electrode and an additional 2 and 5% errors for the protruding and recessed electrodes respectively. Studies of the effect of electrode length on mass transfer measurements for flush electrodes were reported previously (Wang, et al, 1996). The electrode area can be of concern when it is wished to minimize the contamination of the solution with metal ions (Turgoose et al, 1995). In that case rectangular segmental electrodes, cut from pipe with the same diameter as the flow cell, could be used as described elsewhere (Postlethwaite et al, 1986; Postlethwaite, 1979; Postlethwaite and Lotz, 1988, Postlethwaite et al, 1978). It is also easier to avoid misalignments with such electrodes which can be polished to a perfect flushness following installation in a plastic tubular cell or electrode holder. The working electrode length for other conditions can be calculated using the methods described above or taken from the experimental data of Berger and Hau (1977).

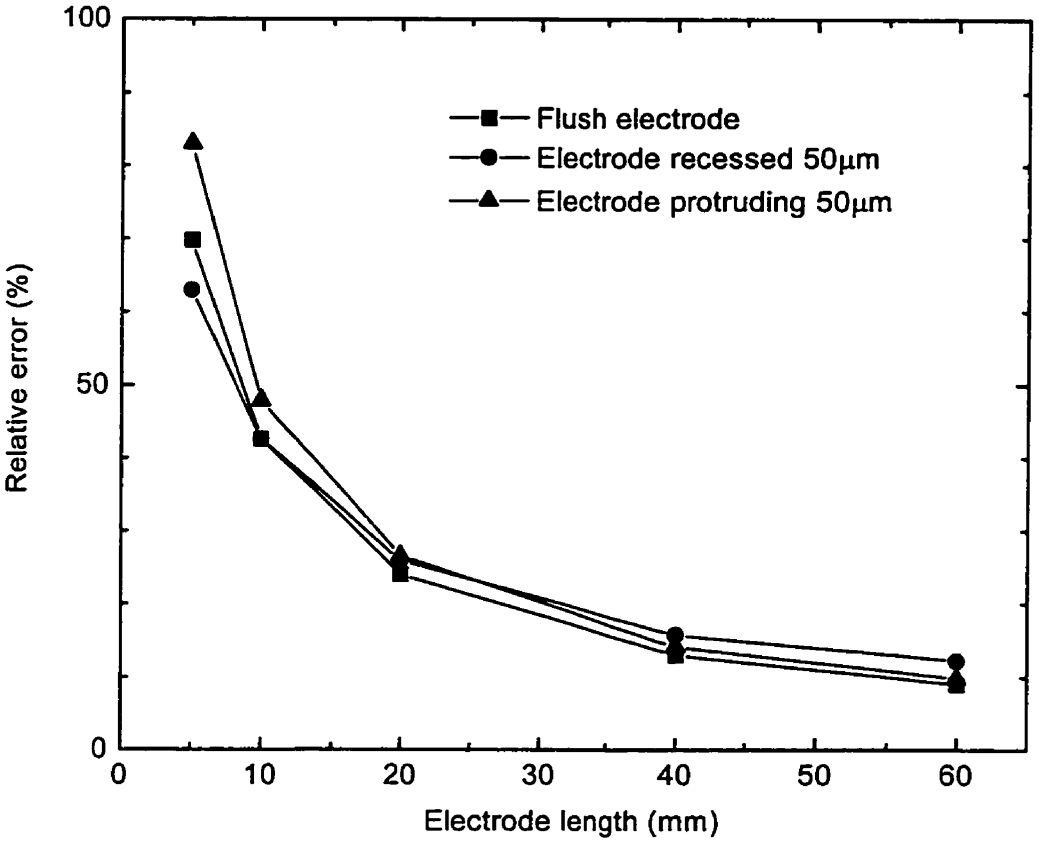

Fig. 6-37 Variation of predicted measurement error as a function of electrode length; entrance effect considered, d=25 mm, electrode length 10 mm, $Re=5\times10^4$.

6.4.6.2. Using Another Electrode Prior to the Working Electrode

The mass-transfer-entry-length is the region where the species (i.e., O_2, Fe^{2+}) concentration boundary layers are developing (see Fig. 6-38a). The concentration profile undergoes a rapid change after reaching the mass transfer section (working electrode) from a non-mass transfer section (preceding non-metallic pipe or inert alloy pipe). The original uniform profile changes to one exhibiting a large gradient of concentration near the wall which causes enhanced mass transfer rate in the leading edge region of the working electrode. Therefore, to reduce mass-transfer-entry-length induced measurement error, one must somehow alter the concentration boundary layer before entering the working electrode so that the developing concentration boundary layer will develop more quickly at the working electrode. One way to do it is to place another electrode with the same material as the working electrode immediately before the working electrode and with very thin non-metallic spacer (say 0.2 to 0.5 mm). A schematic diagram for such an electrode arrangement is shown in Fig. 6-38b. The concentration boundary layer (and concentration profile) will first develop at the preceding electrode. With very thin non-metallic spacer between the two electrodes, this will cause the concentration boundary layer (and concentration profile) to become fully developed more quickly and in this way smaller measurement error can be achieved. Several studies have been made of the use of small insulated electrodes, situated in a larger electrode for mass transfer measurements with single electrode reaction (Schutz, 1964; Sprague, 1984; Deslouis et al, 1980; Deslouis et al, 1981; Wein and Wichterle, 1989; Furuta et al, 1974). In this case an active pre-electrode is required. For corrosion studies

the pre-electrode can be left to corrode freely whilst the working electrode is polarized a few mV required to determine the polarization resistance since the small net current generated will not significantly alter the concentration gradients of reactants and products.

Fig. 6-39 shows the effect of the length of the preceding electrode on the predicted measurement error for a 10 mm long working electrode with the spacer thickness of 0.2 and 0.5 mm respectively. From Fig. 6-39 it is seen that if <10% measurement error is required, a 10 mm preceding electrode is needed in the case when a 0.5 mm non-metallic spacer is used. If <5% measurement error is required, the preceding electrode must be 30 mm or longer. If a pre-electrode was used the accuracy of the corrosion measurement would be increased for a given total length of metal corroding and the surface concentrations at the working electrode surface would correspond more closely to those of fully developed flow.

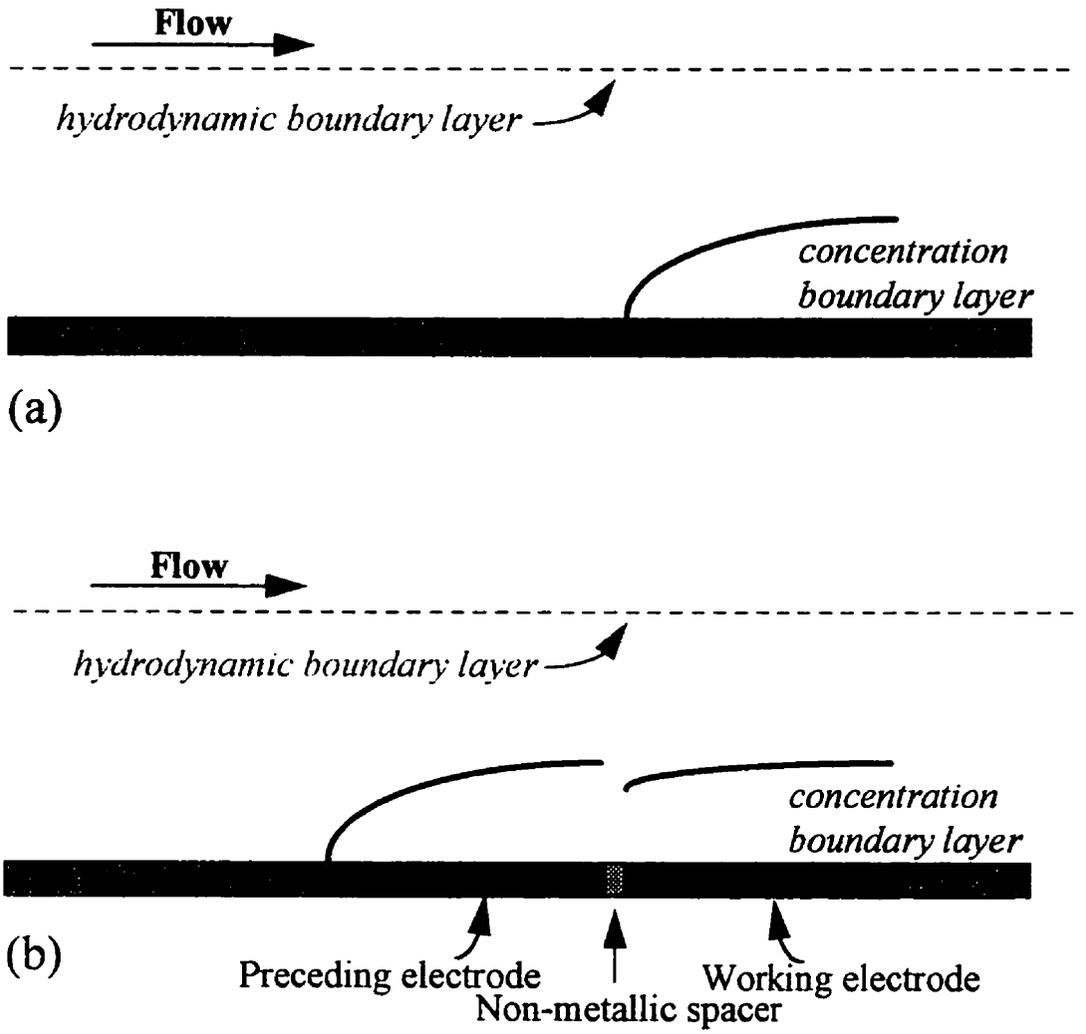

Fig. 6-38 Schematic diagram of development of concentration boundary layer in the leading section of working electrode with (b) or without (a) preceding electrode.

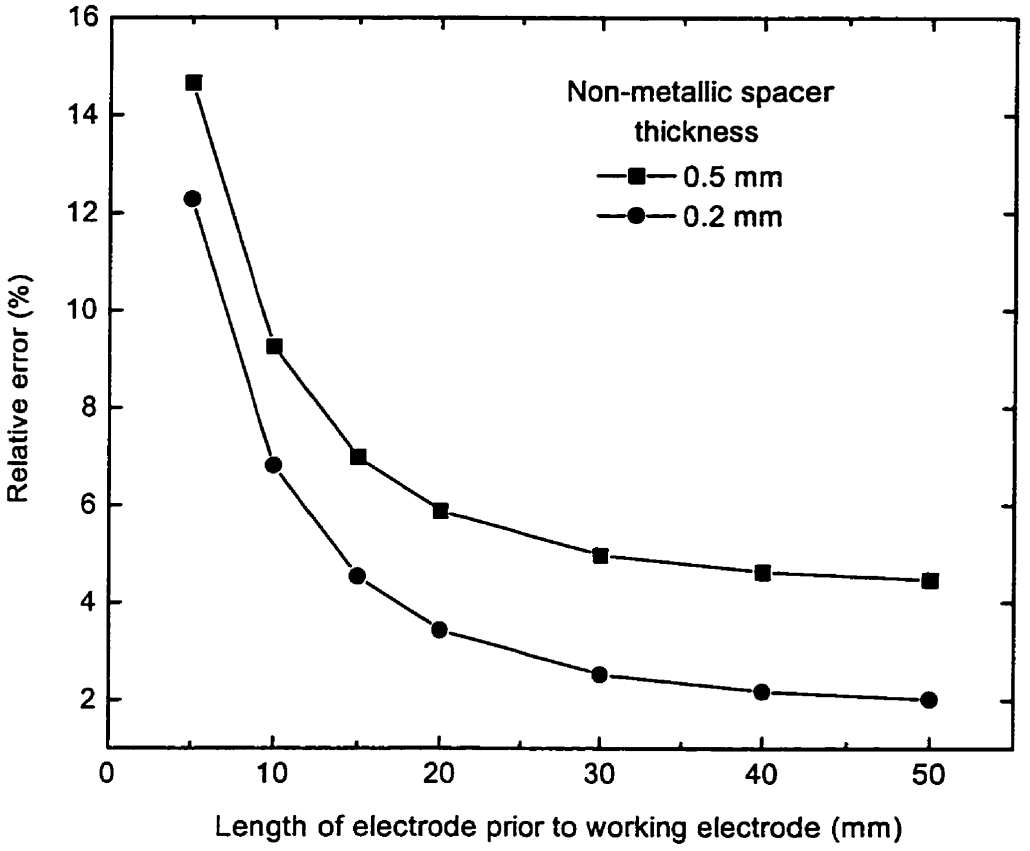

Fig. 6-39 Variation of predicted measurement error caused by mass transfer entrance as a function of preceding electrode length; d=25 mm, electrode length 10 mm, Re=5×10^4.

6.5. Relationship between Modelled Turbulence Parameters and Corrosion Product Film Stability

6.5.1. Introduction

The effect of single-phase aqueous fluid flow on the stability of corrosion product films is a very important factor in determining the utility of many alloys for applications in process piping system, resulting in velocity limits and restricted throughputs. However, the disruption of corrosion product film by single phase turbulent flow is still a serious problem that has proven difficult to quantify. Present industrial practices involve design rules based on bulk flow properties such as bulk velocities, Reynolds number (e.g. the design velocity for copper pipe in recirculating hot-water system is 0.9 to 1.5 m/s (Crooks, 1993)). The majority of failures however occur under conditions of disturbed flow at elbows, weld beads, various fittings and other sudden changes in flow geometry. Under such conditions the application of the bulk flow parameters, velocity, Reynolds number and wall shear stress (based on the bulk velocity) as the criterion for films disruption is not appropriate. Turbulence models have been used to calculate both the local levels of turbulence and the rates of mass transfer under disturbed flow conditions, providing the local parameters appropriate for the development of film disruption.

This part of the study describes the attempt for the application of the LRN, k-ε turbulence model to calculate the local near-wall turbulence profile, the local wall shear

stress profiles and the local mass transfer-rate profile along the length of a copper specimen corroding under disturbed flow conditions and to relate the profiles to the observed film disruption. An electrochemical model which can account for anodic dissolution of copper in aerated 3% NaCl solution was used to illustrate the thermodynamic conditions for film formation on copper surface in the present flow system.

6.5.2. Experimental Setup

The flow system (Fig. 6-40) used for the experiments includes aeration/deaeration column, rubber centrifugal pump, acrylic rectangular duct and flow cell, double pipe heat exchanger and orifice flow meter. While the whole flow system was available from the existing experimental device, both the acrylic rectangular duct and flow cell were redesigned for the current study. The flow cell and computational domain are shown in Fig. 6-41. The acrylic flow cell had a rectangular cross section with a flow channel 50.8 mm wide × 15 mm deep, with equivalent diameter, d_e=23.2 mm. The copper deck and the symmetrical acrylic cell cover had backward and forward facing 2 mm steps to form a constriction with d_e=18.1mm. The flow cell was located horizontally in the above flow system (Fig. 6-40). The length of the straight acrylic duct before entering the flow cell was 40 d_e and the exit length was 20 d_e. The copper deck was machined from 99.99% purity electrolytic copper plate. The test solution was 3% NaCl with the solution pH between 7.9 and 8.3 during the experiment at 25°C which is close to the typical pH value

of sea water, pH=8.3 (Faita et al, 1975). The bulk velocity, U_b, based on the unconstricted cross section, was in the range 0.3~1.49 m/s. The development and destruction of the corrosion product films were observed through the transparent flow cell.

It should be noted here that due to the requirement of the seal between the copper deck and acrylic duct, the forward facing step forming constriction section was not exactly perpendicular to the acrylic duct wall. In fact, the forward facing step was at 95 degree to the duct wall which might contribute some discrepancy between the experimental observation and modelled near wall turbulence parameters.

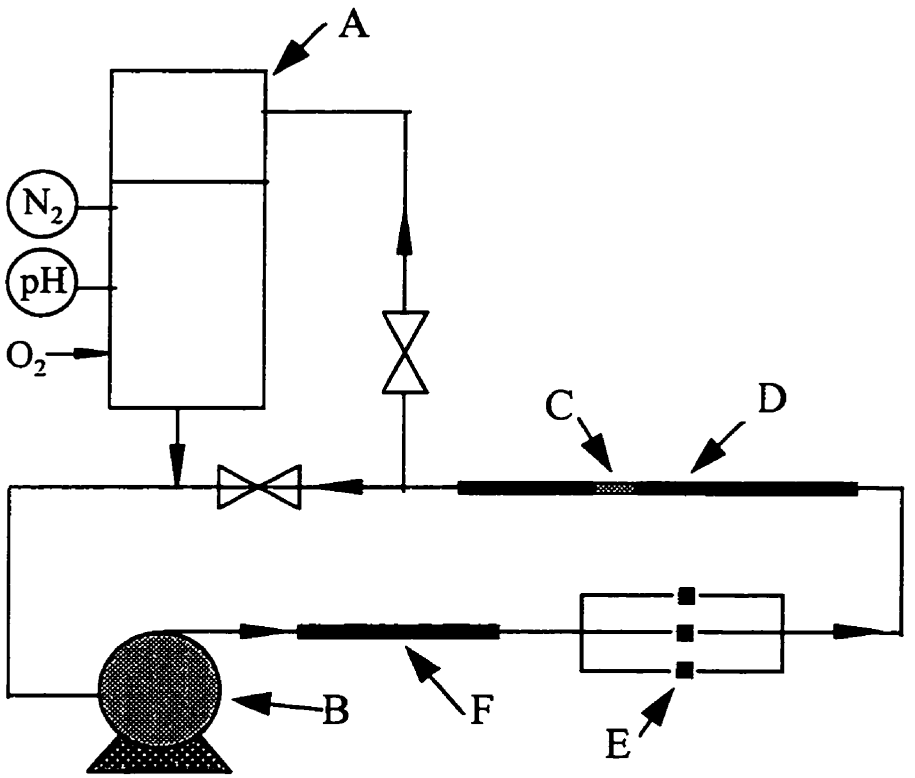

Fig. 6-40 Flow system; A----Aeration/deaeration column; B----Rubber centrifugal pump; C----Flow cell; D----Acrylic rectangular duct; E----Orifice flow meter; F----Double pipe heat exchanger.

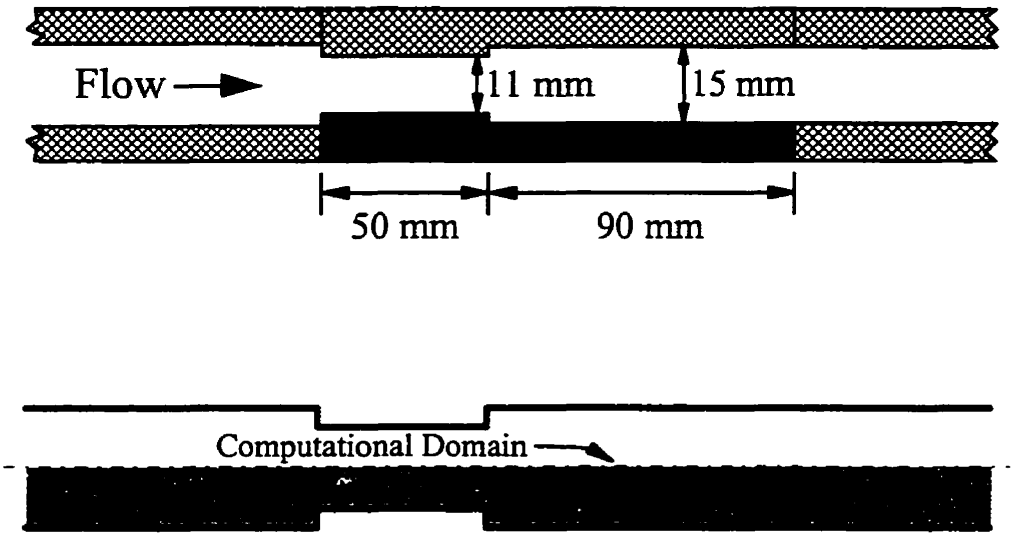

Fig. 6-41 Flow cell and computational domain.

6.5.3. Electrochemical Model

6.5.3.1.Anodic Dissolution of Copper

Many experimental studies (e.g. Bianchi et al, 1978; Smyrl, 1985) done previously on copper dissolution in chloride solution have shown that copper dissolves as cuprous ions which are stabilized by chloride ions in the form $CuCl_x^{(x-1)-}$. The predominant complex species is $CuCl_2^-$ (King and Litke, 1989). Various mechanisms have been proposed to describe the dissolution process of copper in chloride solution (Deslouis, et al, 1988). These mechanisms differ in the dependence of the charge transfer rate at the metal surface on electrode potential and chloride activity. The common point of these mechanisms is that the dissolution rate of copper is partially controlled by the rate of transport of $CuCl_2^-$ away from the metal/solution interface.

Among these mechanisms for copper dissolution in chloride solution, the one proposed by Bacarella and Griess (1973), and Tribollet and Newman (1984) was used:

$$Cu + 2Cl^- \Leftrightarrow CuCl_2^- + e \tag{6-16}$$

$$CuCl_2^-(surface) \xrightarrow{r.d.s} CuCl_2^-(bulk) \tag{6-17}$$

The equilibrium potential for copper dissolution (6-16) is expressed as

$$E_e = 0.205 + \frac{2.303RT}{F} \lg \frac{[CuCl_2^-]}{[Cl^-]^2}, \quad V \text{ vs } SHE \tag{6-18}$$

The rate equation based on this mechanism is as follows:

$$i = \vec{i} - \overleftarrow{i} = i_0\left[\exp\left(\frac{\alpha_a F\eta}{RT}\right) - \frac{[CuCl_2^-]_s}{[CuCl_2^-]_b}\exp\left(-\frac{\alpha_c F\eta}{RT}\right)\right] \tag{6-19}$$

The mass transport rate equation for $CuCl_2^-$ is

$$i = \frac{zK_{CuCl_2^-}F}{(1-t_{CuCl_2^-})}([\mathrm{Cu}Cl_2^-]_s - [\mathrm{Cu}Cl_2^-]_b) \tag{6-20}$$

Again, as mentioned before, since uniform corrosion with microscopic corrosion cells was being modelled, ionic transport was not a factor and $t_{CuCl_2^-} = 0$. After eliminating $[CuCl_2^-]_s$ from equations (6-19) and (6-20), the following kinetic equation for copper dissolution was obtained:

$$i = \frac{i_0\left(10^{\frac{\eta}{b_a}} - 10^{-\frac{\eta}{b_c}}\right)}{1 + \frac{i_0}{zK_{CuCl_2^-}F[CuCl_2^-]_b}10^{-\frac{\eta}{b_c}}} \tag{6-21}$$

where $b_a = \frac{2.303RT}{\alpha_a F}$ and $b_c = \frac{2.303RT}{\alpha_c F}$. According to Bacarella and Griess (1973) α_a=1.0, and α_c=0.5 was assumed giving b_a=0.06 V and b_c=0.12 V at 25°C. Since the exchange current density, i_0, for copper dissolution in chloride solution is not available, it was assumed that i_0=10^{-3} A/m^2 at $[CuCl_2^-]_b$=10^{-6} mol/dm^3.

The mass transfer coefficient of $CuCl_2^-$ ion, $K_{CuCl_2^-}$, can be calculated using LRN k-ε turbulence model. The diffusion coefficient of $CuCl_2^-$ ion was assumed to be 10^{-9} m^2/s (Bacarella and Griess, 1973).

6.5.3.2.Oxygen Reduction

Oxygen reduction is the only cathodic reduction reaction taken into account in copper corrosion in chloride solution in the present study. The rate equation for oxygen reduction is

$$\frac{1}{i} = \left(\frac{1}{i_0 10^{\frac{\eta}{b_c}}} \right) + \left(\frac{1}{i_{\lim}^d} \right) \tag{6-22}$$

where $i_0=10^{-8}$ A/m^2 and b_c=0.12 V at 25°C was assumed. The limiting current density for O_2 reduction is

$$i_{\lim}^d = 4K_{O_2} F[O_2]_b \tag{6-23}$$

where $[O_2]_b$=6 ppm was assumed based on the measurement.

6.5.3.3.Implementation of the Electrochemical Model

The corrosion potential, E_{corr}, and the corrosion current densities, i_{corr}, were determined by solving the set of equations (6-21) and (6-22). The surface $CuCl_2^-$ concentration was calculated as follows:

$$[CuCl_2^-]_s = \frac{i_{corr}}{zFK_{CuCl_2^-}} + [CuCl_2^-]_b \tag{6-24}$$

The surface OH^- ion concentration was determined as follows:

$$[OH^-]_s = \frac{i_{corr}}{FK_{OH^-}} + [OH^-]_b \tag{6-25}$$

To judge the possibility of the formation of Cu_2O on copper surface, the knowledge of cuprous ion concentration is necessary. Since for the reaction

$$Cu^+ + 2Cl^- \Leftrightarrow CuCl_2^- \tag{6-26}$$

the stability constant of the complex ion $CuCl_2^-$ is

$$K_{CuCl_2^-} = \frac{[CuCl_2^-]}{[Cu^+][Cl^-]^2} = 8.71 \times 10^4 \text{ (Sillen and Martell, 1964)} \tag{6-27}$$

The surface cuprous ion concentration can be determined from

$$[Cu^+]_s = \frac{[CuCl_2^-]_s}{[Cl^-]^2 \times 8.71 \times 10^4} \tag{6-28}$$

6.5.4. Results

6.5.4.1. Preliminary Observation of Film Formation Conditions

The highest flow velocity, U_b=1.49 m/s based on the unconstricted section, of this system at 25°C was used to see what would happen on a corroding copper surface. The observation for a period of 16 days indicated that the corroded copper surface is metallic pink in color and there was no corrosion product film formed on copper (confirmed by later surface analysis) in 3% NaCl solution when flow velocity is 1.49 m/s. A lower flow velocity should be used in order to grow films.

6.5.4.2. Film Formation and Removal

Film growth and removal Fig. 6-42 shows the surface appearances of copper deck at different stages of the experiment lasting 1247 hours (52 days). It was observed during the experiment that when bulk velocity was set to 0.5 m/s and left for 11 days (Fig. 6-42a), the film grew unevenly on the copper surface with light brown film grown on the further downstream regions of both sudden constriction and sudden expansion. The immediate sudden constriction downstream region and the downstream region of sudden expansion (5 to 25 mm from the backward facing step) were metallic pink in color suggesting no-film formed in these regions which was followed by a 10 mm band which was partially covered by brown film. The brown film grown on copper surface is believed to be Cu_2O (Wood et al, 1990). There was a 5 mm dark brown band in the immediate downstream region of the sudden expansion suggesting a thicker film formed in this dead water zone. There was a small amount of green corrosion product in the sudden constriction section.

When the bulk velocity was decreased to 0.3 m/s, for 17 days (Fig. 6-42b), the originally light brown film became darker suggesting thicker films formed and both brown regions expanded leaving a 4 mm lighter colored band starting 2 mm from the sudden constriction, and a 8 mm wide lighter colored band starting 5 mm from the sudden expansion. Also, green corrosion products started to form on the brown film surface.

When the bulk velocity was set to 0.5 m/s again and left for 10 days (Fig. 6-42c), the lighter colored 4 mm wide band in the constriction section gradually became metallic pink and expanded to 7 mm in width. Also the lighter colored band in the expansion section gradually became metallic pink in color and the width expanded to 10 mm. But this metallic pink band was not recovered to the original 20 mm in width as the bulk velocity was first set to 0.5 m/s and maintained for 11 days. More green corrosion products formed on the brown film surface.

When the bulk flow velocity was increased to 1.0 m/s and maintained at this velocity for 14 days (Fig. 6-42d), both downstream regions stayed metallic pink in color and no obvious thinning of the film was observed. The film remained intact in a 5 mm band immediately downstream of the sudden expansion until the end of the experiment on day 52. During this time, more green corrosion products formed on the brown film.

The above experimental observations indicate that the corrosion film can grow on copper surface at flow velocity U_b=0.5 m/s ($Re=1.26\times10^4$) in a straight duct (50 × 15 mm) without constriction. With the constriction section (step height 2 mm in this experiment), the film will not grow in the regions downstream of both the (Fig. 6-42a) sudden constriction and sudden expansion. It is the disturbed flow caused by sudden constriction and sudden expansion that leads to enhanced turbulence fluctuation and mass transfer rate in the near wall region which may contribute to the uneven film formation condition. This will be discussed in subsequent sections.

The experimental observations also show that a lower flow velocity (U_b=0.3 m/s in this case) favored the formation of corrosion film. The film grown at lower flow velocity (e.g. U_b=0.3 m/s) can not be completely removed at higher flow velocity (U_b=0.5~1.0 m/s) though these films would not grow at these higher velocities.

It was also observed that during the course of the experiments green corrosion products formed gradually on the brown film surface. The solution pH during experiment was between 8.0 to 8.25 at 25°C (close to typical pH value of sea water, pH=8.3 (Faita et al, 1975)). The corrosion potential of the copper in 3% NaCl solution was measured as -0.21 to -0.20 V (SCE) in a similar experiment. The Pourbaix potential-pH diagram for copper-sea water system (Bianchi and Longhi, 1973) shows that in the corrosion potential range from -0.21 to -0.20 V (SCE) (or 0.03 to 0.04 V, SHE), the points with bulk pH ranging from 8.0 to 8.25 are in the stable zone of Cu_2O. So the initially formed film should be mainly composed of Cu_2O. Since the surface concentration of dissolved species and surface pH are higher than the bulk ones due to the anodic dissolution of copper and oxygen reduction on copper surface, it is possible that Cu_2O and Cu^+ at the surface will be oxidized to form higher valence of copper compound or complex. The green corrosion products formed on the brown film surface in this experimental observation are probably attributed to the higher concentration of dissolved metal ions which may form complex with Cl^- (e.g. $Cu_2(OH)_3Cl$). The test solution, although completely changed every three or four days, will become more concentrated between the changes. This would also speed up the formation of the green corrosion product.

Surface appearances The scanning electron photomicrographs of the surface appearances at different sites of the copper deck (see also Fig. 6-42d) are shown in Fig. 6-43. It can be seen from Fig. 6-43a and Fig. 6-43b that in the sites within area ① (immediate downstream zone of sudden constriction) and within area ④ (recirculation zone downstream of sudden expansion), there is no film formed on the corroded copper surface. The films formed on copper surface in areas ② and ⑤ contain numerous pits, while the films on copper surface in area ③ (dead water zone) seems more compact with a few pits which might be attributed to the unique hydrodynamic condition in this region. It is believed that the green film is a copper hydroxychloride (e.g. $Cu_2(OH)_3Cl$) based on the Potential-pH diagram of Copper-sea water system (Bianchi and Longhi, 1973) and similar experiments done by other researchers (e. g. Melton, 1991; MacDonald et al, 1978).

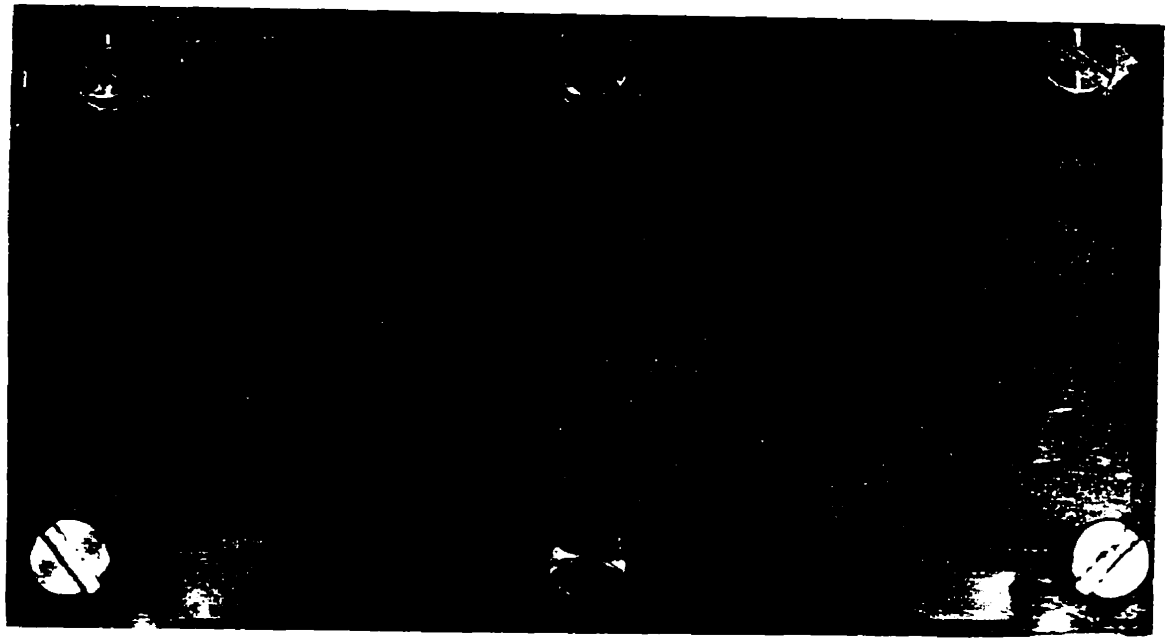

a)

Flow

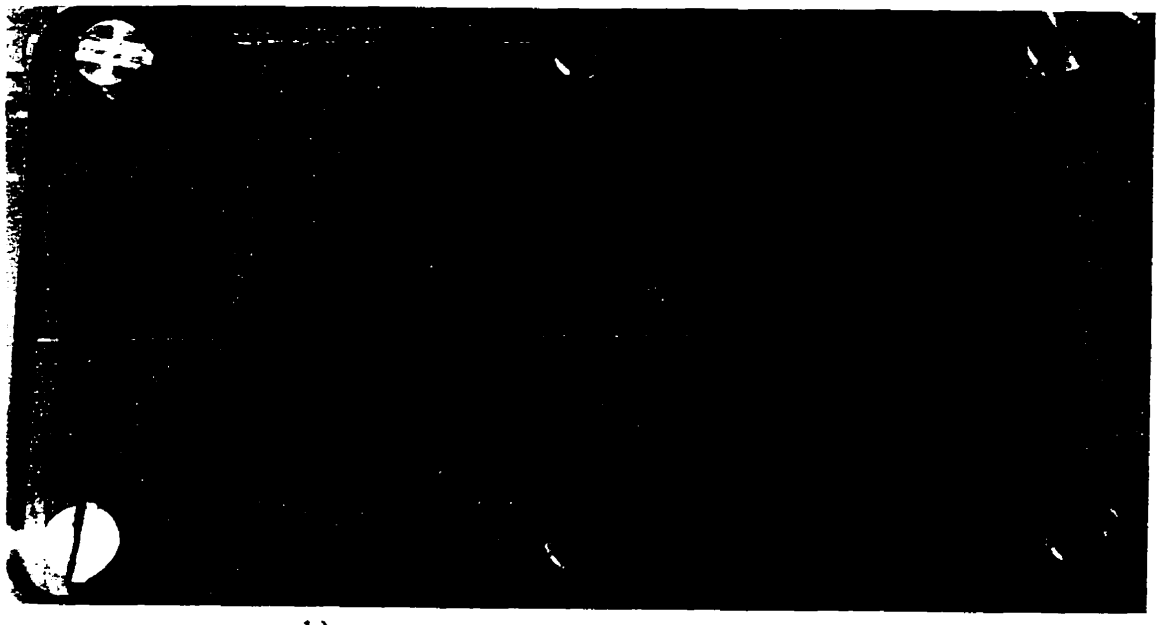

b)

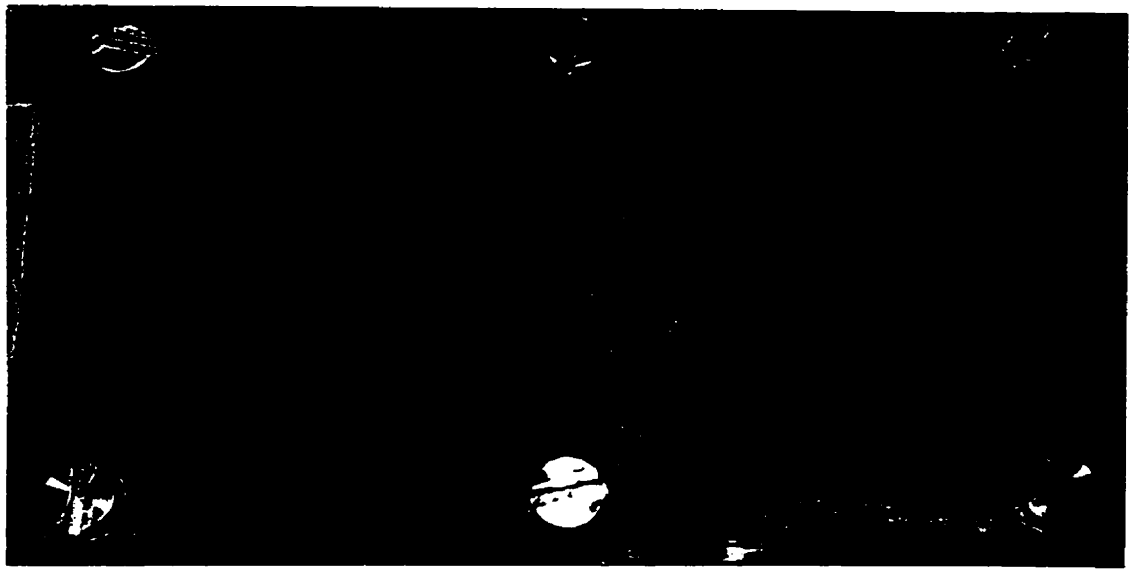

c)

Flow

d)

Fig. 6-42 Formation and removal of corrosion film, a) 0.5m/s for 11 days; b) 0.3m/s for 17 days; c) 0.5m/s for 10 days; d) 1.0m/s for 14 days, 35°C, aerated 3% NaCl solution.

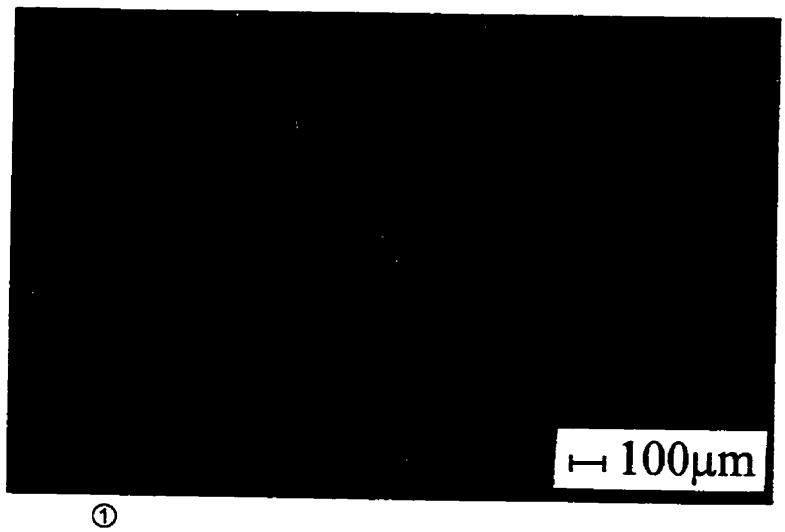

①

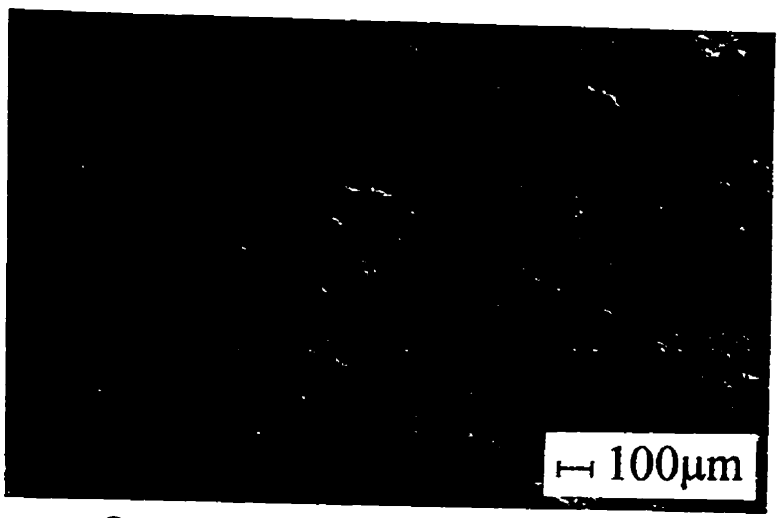

②

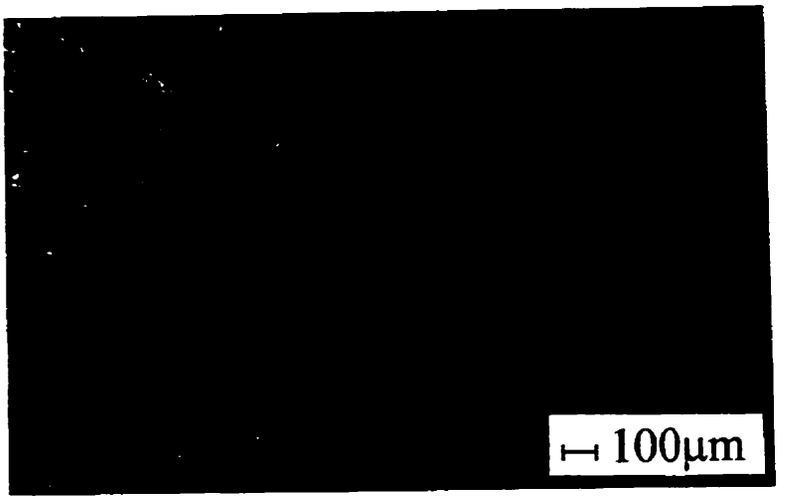

③

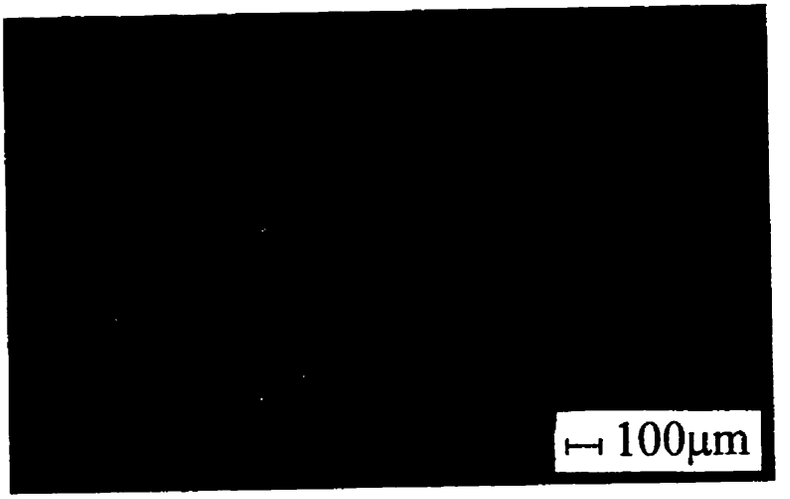

④

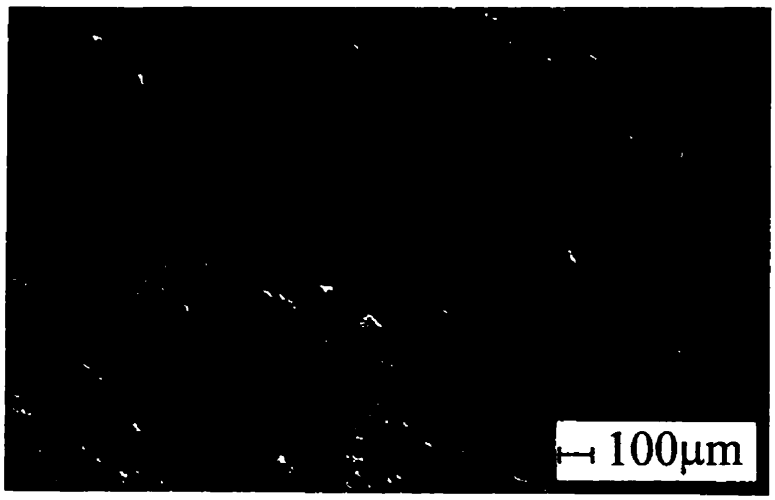

⑤

Fig. 6-43 SEM photomicrographs of surface appearance at different sites of copper deck after experiment, ① Metallic pink area downstream of sudden constriction; ② further downstream region of sudden constriction; ③ Dead water zone; ④ Metallic pink region downstream of sudden expansion, ⑤ Further downstream region of sudden expansion, Copper was exposed in flowing aerated 3% NaCl solution for 52 days at 35°C (0.5m/s for 11 days + 0.3m/s for 17 days + 0.5m/s for 10 days + 1.0m/s for 14 days).

6.5.5. Discussion

The observation made are now discussed in relation to the near wall turbulence parameters, local mass transfer rate and wall shear stress, which are calculated using LRN k-ε turbulence model, and the surface cuprous ion and hydroxyl ion concentrations determined from the electrochemical model.

6.5.5.1.Near Wall Turbulence

The leading edge area of sudden constriction and the recirculation zone downstream of sudden expansion where the films are least easily grown and most easily removed are the two regions where the greatest near wall turbulence would be expected to occur. Near-wall velocity fluctuations, u', were used here to quantify the near wall turbulence (Nesic, 1991). The velocity fluctuations (RMS) were calculated from the kinetic energy of turbulence given by the k-ε turbulence model assuming isotropic turbulence.

The velocity fluctuations for the three bulk velocities used were shown in Fig. 6-44 (a). The predicted velocity fluctuations at 0.6 mm from the wall were used, where y^+=24, 44, and 64 at U_b=0.5, 1.0 and 1.47 m/s, respectively under fully developed flow conditions. If velocity fluctuations can be used as a criterion for the turbulence level required for film removal the following assumptions can be drawn. The fluctuation

velocity of 0.16 m/s at U_b=1.47 m/s prevents the film from growing on copper surface in the present flow geometry. At the fluctuation velocity less than 0.08 m/s at U_b=0.5 m/s, the film will grow on most regions of the copper deck except downstream regions of both the sudden constriction and sudden expansion where the fluctuation velocities are higher than 0.08 m/s at U_b=0.5 m/s (see also Fig. 6-42 (a)). The film formed when the fluctuation velocity was less than 0.08 m/s at U_b=0.5 m/s for more than 20 days could not be removed as the fluctuation was increased to 0.12 m/s at U_b=1.0 m/s and maintained at this velocity for 14 days. This indicates that the critical fluctuation velocity for removing the pre-formed film should be higher than 0.12 m/s.

It should be remembered here that there are no velocity fluctuations directly at the wall. The near wall fluctuating velocity used in this study is only the indicator of the turbulence level required for film removal, not the cause of the film removal. There are however both shear stresses (Shah and Antonia, 1986) and pressure fluctuations (Launder, 1989) directly at the wall. The wall shear stress calculated based on the local mean velocity gradient is not an appropriate parameter as a criterion for film removal under disturbed flow conditions (Nesic and Postlethwaite, 1990) as discussed in the next section. The pressure fluctuations at the wall could provide sufficient lift force to remove the corrosion product film. Unfortunately, the pressure fluctuation at the wall can not be modelled with the k-ε turbulence model with which only the mean value of the pressure term can be calculated. Future modelling work in this field should involve uses of the large eddy simulation (LES) and/or direct numerical simulation (DNS) in the viscous

sublayer that would lead to a much greater understanding of the surface transport process.

The formation and removal mechanisms of the corrosion product film in turbulent pipe flow were also explained qualitatively on the basis of the turbulent "burst" theory (Dawson, 1990). Some turbulent eddies in the free stream fluid will penetrate the boundary layer and impinge on the surface. The impulse motions generate the lift force that could contribute to the removal of the corrosion product film. The major feature of the turbulent burst concept is that the corrosion films are able to nucleate during the quiescent period. A subsequent burst may remove the film nuclei or part of the corrosion product film. Actually, both shear stress and pressure fluctuations at the wall are directly associated with the burst phenomena. Again, the k-ε turbulence model can not predict the impulse motions (or the lift forces) associated with the bursting phenomena, Use of LES or DNS can predict the impulse motions that would help the understanding of the mechanisms of the film formation and removal.

If a critical value of the modelled velocity fluctuations as an indicator for preventing film growth on copper surface were to be chosen in the present flow system, it would be around 0.08 m/s.

6.5.5.2. Wall Shear Stress

The wall shear stress values at U_b=0.5~1.47 m/s at the leading edge of the sudden constriction (Fig. 6-44 (b)) exceed the value of 9.6 Pa, calculated from bulk velocity in a

straight duct system, reported by Efird (1977) for the accelerated corrosion of 99.9% Cu alloy CDA 122, due to degradation and physical removal of protective films. The values in the region downstream of the sudden constriction are also greater than 9.6 Pa at U_b=1.47 m/s. The maximum values of wall shear stress downstream of the sudden expansion at x≈55 mm are smaller than 9.6 Pa, although the position of the maximum value corresponds to the starting position for the film-free band (Fig. 6-42). It must be noted that several investigators (Syrett, 1976; Bianchi, et al, 1978; MacDonald, et al, 1978) have questioned whether the small values of wall shear stress said to be responsible for film removal are indeed capable of physically removing tightly adherent protective films and the values calculated for the present system, even at the points of disturbed flow, are small.

6.5.5.3.Mass Transfer

The mass transfer coefficients calculated on the basis of the transfer of complex ion $CuCl_2^-$ with a Schmidt number of 924 are shown in Fig. 6-44 (c). For the bulk velocities U_b=0.5~1.47 m/s, the rates of mass transfer are much higher in the leading edge section of the sudden constriction where film formation was prevented (see also Fig. 6-42 (a)). In the sudden expansion section, the local maximum values of mass transfer were found in the recirculation zone upstream of the reattachment point where the film formation is also prevented. Syrett (1976), Lotz and Heitz (1983), Bianchi et al (1978) and Bacarella and Griess (1973) have discussed the role of mass transfer in the formation and disruption of protective films on copper. Sydberger and Lotz (1982)

suggested that there is no analogy between mass transfer and wall shear stress at and near the flow reattachment point where $\tau_w = 0$. They suggested that the shear stresses in the regions upstream and immediately downstream of the reattachment point are lower than there for fully developed flow and that is the case in the present simulations. The prediction in this study also shows that the position for maximum mass transfer coincides with the position for the highest value of near-wall turbulence which was found in the recirculation zone upstream of the reattachment point where the values are higher than those in fully developed flow (Fig. 6-44). The present simulation results suggest that it is not appropriate to use wall shear stress as a criterion for film formation and removal in the flow system involving disturbed flow conditions. Mass transfer could be correlated closely with the near-wall turbulence. Disturbed flow condition will cause higher turbulence in the near wall region which in turn leads to a higher mass transfer rate by thinning diffusion controlled mass transfer boundary layer (Nesic and Postlethwaite, 1991a). Furthermore, the non-uniform mass transfer rate of corrosion products away from the corroding surface will cause non-uniform film formation conditions which will be discussed in more detail in the subsequent section.

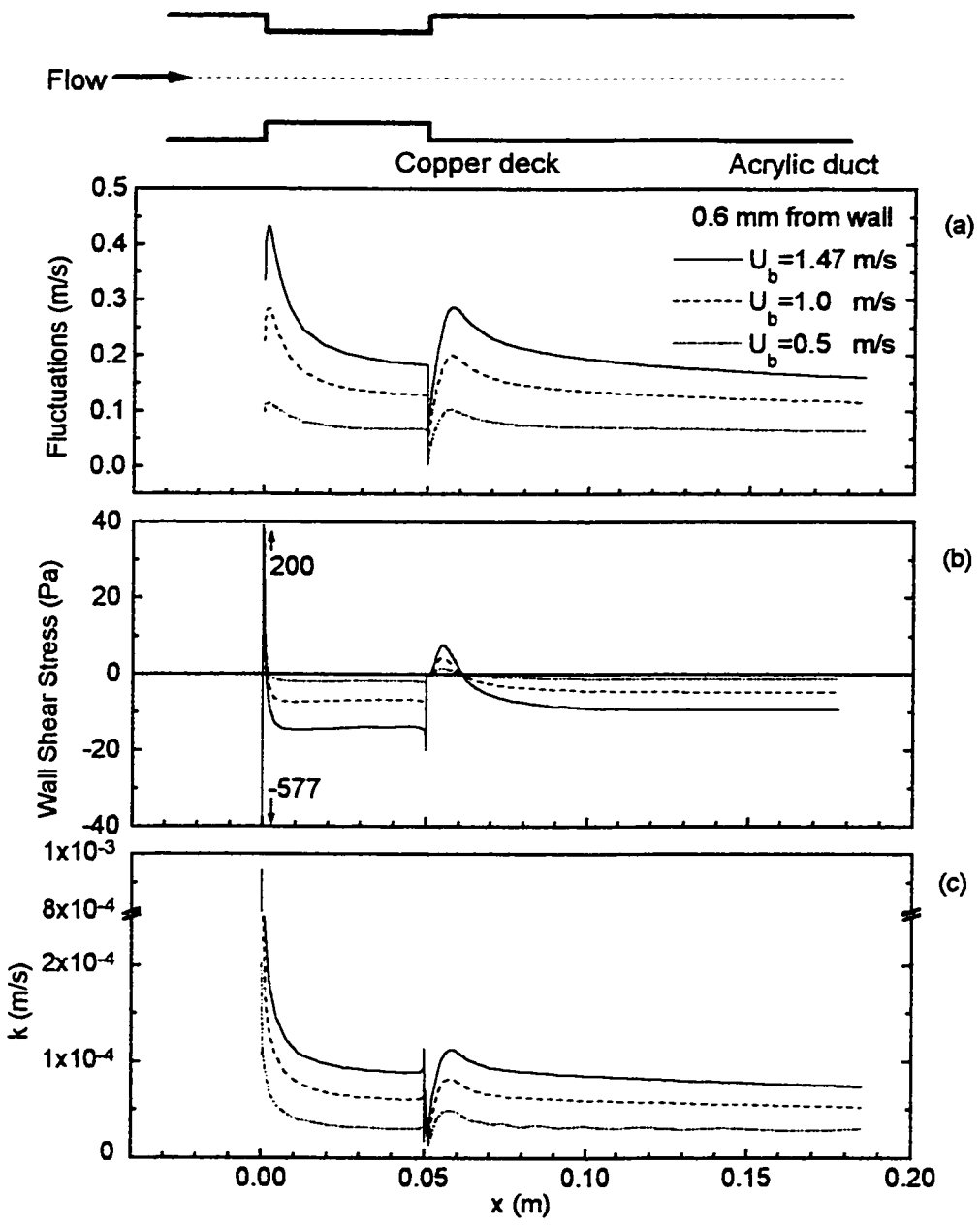

Fig. 6-44 Predicted velocity fluctuations at 0.6 mm from the wall (a), wall shear stresses (b) and mass transfer coefficients (c) at bulk velocities of 0.5, 1.0 and 1.47 m/s at 25°C.

6.5.5.4. Thermodynamic Conditions for Film Formation

The experimental observations made in this study show that the film can not grow in the immediate region downstream of the sudden constriction and the recirculation zone downstream of the sudden expansion, but can grow in other regions on the copper surface at U_b=0.5 m/s (Fig. 6-42 (a)). This prompts us to investigate the thermodynamic conditions for film formation. On a freely corroding copper surface in aerated NaCl solution, both anodic and cathodic processes occur and both $CuCl_2^-$ and OH^- are produced at an equivalent rate. But the surface concentrations of both species are not the same because of different diffusion coefficients of $CuCl_2^-$ and OH^-. The surface OH^- concentration can be calculated from equation (6-25). Surface Cu^+ is in the equilibrium state with surface $CuCl_2^-$ and can be determined from (6-28).

The products of surface [Cu^+] and surface [OH^-], [Cu^+][OH^-], for U_b=0.5~1.47 m/s are shown in Fig. 6-45. Also shown in Fig. 6-45 is the solubility product of Cu_2O at 25°C. Fig. 6-45 illustrates one case in which the product of surface [Cu^+] and [OH^-] is lower than the solubility product of Cu_2O in both downstream regions of sudden constriction and expansion at U_b=0.5 m/s, showing that formation of Cu_2O in both regions is thermodynamically impossible, while in the other regions on the copper deck the product is higher than the solubility product of Cu_2O showing the possibility for the formation of Cu_2O in these regions. Although the above predictions are based on the electrochemical model in which exchange current density for anodic dissolution of

copper in chloride solution is assumed, there is such a possibility that in the present flow geometry (duct flow with sudden constriction and expansion) film formation is thermodynamically possible in some areas (e. g. immediate downstream region of sudden constriction and the recirculating zone downstream of sudden expansion) and impossible in other areas.

Fig. 6-45 also shows that the product of surface [Cu^+] and [OH^-] is lower than the solubility product of Cu_2O on all copper surface except in the narrow zone immediately downstream of sudden expansion at U_b=1.0~1.47 m/s. The experimental observation has shown that no film formed on copper surface at U_b=1.47 m/s. But the experimental observation also shows that the film grown at U_b=0.5 m/s could not be removed at U_b=1.0 m/s while the more green corrosion product precipitates on the film surface. A possible explanation for such a phenomenon is that the green product formed on the previously grown film surface, as observed in present experiments, is a film of sparingly soluble compounds of cupric copper, such as atacamite ($Cu_2(OH)_3Cl$). The presence of cupric species is due to the fact that the corrosion of copper in the active state corresponds to the consumption of only small amounts of oxygen which may diffuse to the surface, while the remaining substantial amount of the total diffusible oxygen is available for the further oxidation of the cuprous species to cupric species (Bianchi, et al, 1978). Furthermore, the presence of an outer film of cupric copper compounds ($Cu_2(OH)_3Cl$) modifies the transport processes of $CuCl_2^-$ and OH^- ions and allows the existence of the protective Cu_2O inner film even at those hydrodynamic conditions

(for example, U_b=1.0 m/s in present flow system) under which Cu_2O film should not grow on copper surface.

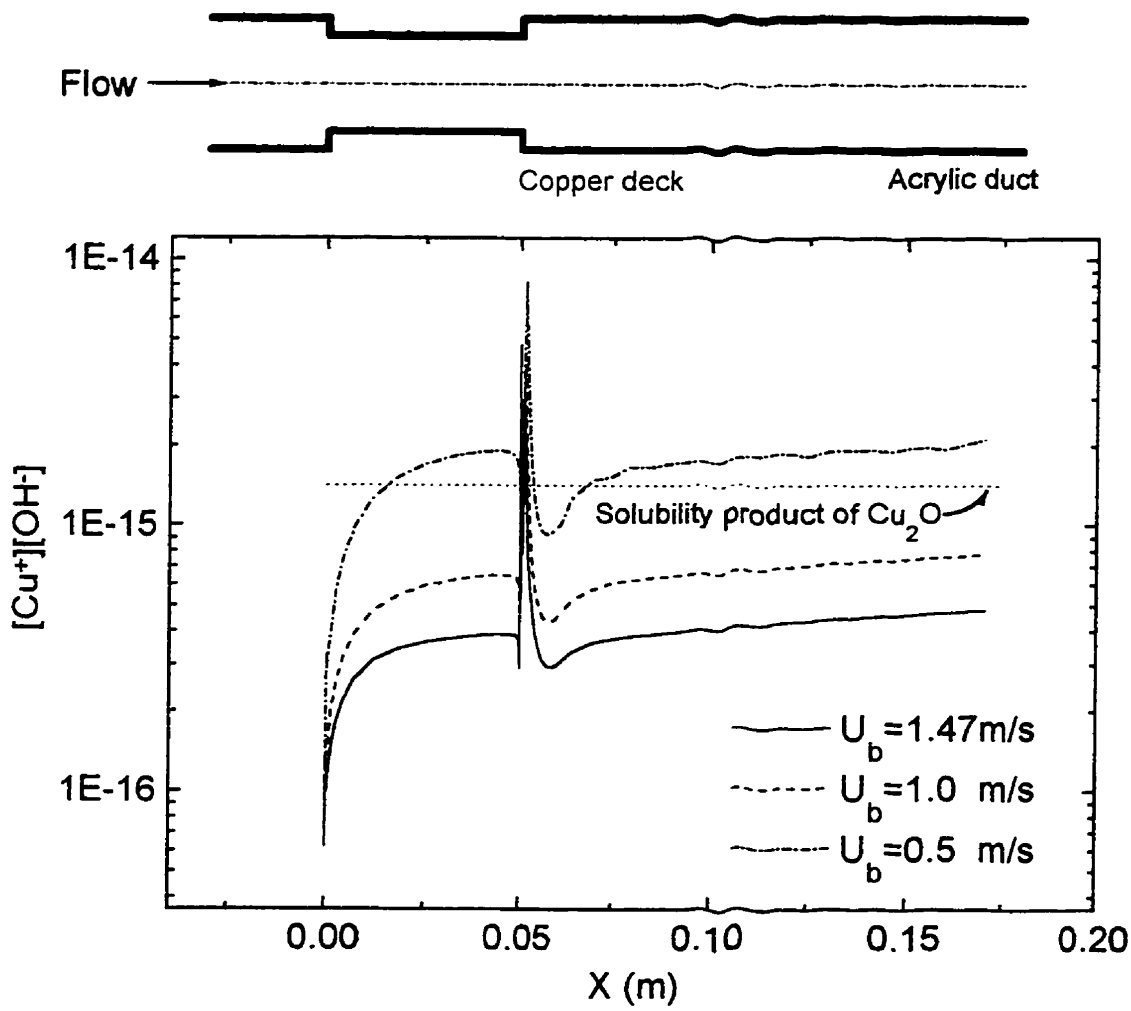

Fig. 6-45 Variation of $[Cu^+][OH^-]$ along the copper deck with forward facing and backward facing steps at bulk velocities of 0.5, 1.0 and 1.47 m/s at 25°C.

6.5.5.5.Summary

The experimental observation of the formation and removal of corrosion film on copper surface was made at U_b=0.3~1.47 m/s. The observation has been discussed with the modelled near-wall turbulence, wall shear stress, mass transfer and film formation conditions. It is found that wall shear stress, calculated from local mean velocity gradient, is not an appropriate parameter as a criterion for film formation or disruption under disturbed flow conditions. Mass transfer coefficients are found to be closely correlated with near-wall turbulence. The disturbed flow conditions in duct flow with a sudden constriction and sudden expansion brings about non-uniform near-wall turbulence and non-uniform mass transfer conditions along the copper deck with both maximum positions coinciding in recirculation zone downstream of the sudden expansion. The non-uniform mass transfer conditions along the copper deck will lead to non-uniform surface metal ion and hydroxyl ion concentrations, which under certain flow condition will provide thermodynamic conditions favoring film formation in some regions and preventing film formation in other regions on copper surface.

7. Conclusions and Recommendations

7.1. Conclusions

A low Reynolds number k-ε eddy viscosity model has been used to determine the effects of mass transfer on corrosion in turbulent pipe flow.

Mass transfer rates were determined under the following conditions;

- developing mass transfer boundary layers;
- fully developed mass transfer boundary layers;
- disturbed flow at backward and forward facing steps.

The mass transfer rate simulations were used to:

- construct E-log*i* kinetic corrosion diagrams for corrosion in both developing mass transfer boundary layers and fully developed mass transfer conditions;
- determine the surface concentration of the dissolved metal ions and the surface pH and predict the film formation condition under the attached and disturbed flow conditions.

- determine the error in electrochemical rate measurement with short working electrodes;
- determine the effect of electrode misalignment on electrochemical corrosion rate measurements;
- prepare mass transfer rate profiles for corroding copper deck under disturbed flow conditions.

The formation and destruction of the corrosion film on copper surface in flowing aerated 3% NaCl solution has been studied in a flow cell at the bulk flow velocities 0.3~1.49 m/s. The copper deck and the symmetrical acrylic cover had backward and forward facing 2 mm steps to form a constriction resulting in disturbed flow in the immediate downstream region of the sudden constriction and the recirculation zone downstream of the sudden expansion. The experimental observations have been discussed with the modelled near-wall turbulence, wall shear stress, mass transfer calculated by the application of the LRN k-ε model.

The following conclusions were drawn:

7.1.1. Mass Transfer in the Entrance Region

1. Comparison has been made between the simulation with the LRN k-ε model and the experimental results of others for the mass transfer in the mass transfer entry length and fully developed region. The predictions are in good agreement with Berger and Hau's (1977) measurements (Re=12,900~135,000, Sc=2244) as well as Son and

Hanratty's (1967) measurements (Re=10,000~55,100, Sc=2400) in both the mass transfer entrance region and the fully developed region. These results show that the model can successfully simulate mass transfer in both the developing mass transfer boundary layer region and under fully developed mass transfer conditions.

2. The predicted mass transfer entrance length (based on local values of the Stanton number) varies from L/d≈5 for Re=12,900 to L/d≈0.25 for Re=135,000 at Sc=2244. Mean Stanton numbers are always higher than local Stanton numbers in the same mass transfer entrance section, and if electrochemical experiments are used to study mass transfer under conditions where the mean K value approaches the fully developed, longer mass transfer sections, from L/d≈9.7 for Re=26,000 to L/d≈1.6 for Re=135,000, are required.

3. There are difficulties in the application of small local electrodes embedded in much larger active electrodes to measure local mass transfer rates. The difficulties are caused by edge effects relating to the electrical insulation surrounding the small local electrode. The errors increase as the local electrode size is decreased. The use of very small electrodes to study the rapidly changing mass transfer rates at the leading edge (<0.2 mm) of the mass transfer entrance length, at high Reynolds numbers, would pose severe practical difficulties since electrodes of the order of 10 μm wide with 1 μm insulation would be required. The use of local electrodes of the order of 100 μm wide with 10 μm insulation for studying the balance of the mass transfer entry length is practical.

7.1.2. Corrosion in the Mass Transfer Entry Length

1. The profiles of the corrosion rate, of the surface concentration of dissolved metal ions and of the surface pH are dependent on the extent to which the mass transfer components control the corrosion process.

2. If the corrosion is under charge transfer control, the surface concentration of dissolved metal ions decreases with rising Reynolds number and increases along the mass transfer entrance region.

3. If the corrosion is solely controlled by the mass transport of oxygen from bulk solution to the metal surface, the corrosion rate increases with Reynolds number and decreases along the mass transfer entrance length. The surface concentration of dissolved metal ions and surface pH do not vary with Reynolds number and the distance along the entrance length. The conditions for film formation would be uniform throughout the mass transfer entrance region.

4. In the case of corrosion being partially controlled by the mass transport of dissolved metal ion from the metal surface to bulk solution, the corrosion rate increases with Reynolds number and decreases along the mass transfer entrance length. The surface concentration of dissolved metal ions and surface pH decrease with rising Reynolds number and increase along the mass transfer entrance length. The much smaller changes of surface metal ion concentration and surface pH in this case, compared to that for corrosion being controlled by O_2 mass transfer, lies in the fact that the corrosion rate is only partially controlled by mass transfer.

7.1.3. Effect of Electrode Misalignment on Corrosion Rate Measurement

1. The effects of both electrode-misalignment and mass-transfer-entry-length can lead to large errors in the measurement of corrosion rates. For example a step height of 500 μm with a 10 mm long protruding electrode increased the 43% mass-transfer-entry-length error with a flush electrode to 86%.

2. The errors due to the mass-transfer-entry-length and electrode-misalignment can be reduced to acceptable values by the choice of electrodes of suitable length (60 mm in the above case) and maintaining the electrode misalignment step height (either protruding or recessed) <50 μm at Reynolds number of 5×10^4.

3. A shorter total length of corroding metal can be used if a preceding corroding specimen is placed immediately upstream and insulated from the working electrode. For polarization resistance measurements with small voltage perturbations of several mV the preceding specimen need not be polarized along with the working electrode. Such an arrangement of the electrodes can reduce the contamination of dissolved metal ion to solution and thus the interference with the corrosion rate measurement.

4. The profiles of both the surface concentration of the dissolved metal ions and the surface pH for mass transfer controlled corrosion are very different to those for charge transfer controlled corrosion. In the mass transfer controlled corrosion the concentration and pH vary little (although with a value much different from the bulk solution) along the corrosion metal surface in the presence of both mass-transfer-entry-length and electrode-misalignment effects. The lack of variation of the metal

ion concentration and pH along the electrode length relates to the ratio of mass transfer coefficients for the reactants and products remaining constant in the presence of both disturbed and developing flow. In the charge transfer case there are substantial variation of surface concentration and pH along the length of the corroding metal.

7.1.4. Relationship between Modelled Turbulence Parameters and Corrosion Film Stability

1. The corrosion films can grow on a copper surface at flow velocity U_b=0.5 m/s ($Re=1.26\times10^4$) in a straight duct with cross section 50 × 15 mm. With the constriction section (step height 2 mm), the film will not grow in both the immediate downstream region of the sudden constriction and the recirculation zone downstream of the sudden expansion. If a critical value of modelled near wall velocity fluctuations was to be used as an indicator for preventing film growth on copper surface in the present flow system it would be around 0.08 m/s.

2. It is not appropriate to use wall shear stress, calculated based on local mean velocity gradient at the wall, as a criterion for film formation and removal in the flow system involving disturbed flow conditions.

3. Local mass transfer coefficients are closely correlated to the near-wall turbulence. Disturbed flow conditions caused by the sudden constriction and sudden expansion will lead to higher turbulence in the near-wall region, which in turn causes higher mass transfer rates in both immediate downstream region of sudden constriction and recirculation zone downstream of sudden expansion. Non-uniform mass transfer

conditions along the copper deck with forward facing step and backward facing step will result in non-uniform film formation conditions. There is a possibility in the present flow system that the film formation is thermodynamically impossible in the area such as the immediate downstream region of the sudden constriction and the recirculation zone downstream of the sudden expansion while it is thermodynamically possible in the remaining regions.

7.2. Recommendations

1. The present turbulence model could be used to simulate the mass transfer and corrosion in the tube side of heat exchanger. The flow conditions in the inlet section of the tubes in heat exchanger involve both developing viscous flow boundary layer and developing mass transfer boundary layer and cause enhanced mass transfer rate and corrosion rates. The simulations results should provide a better understanding of the corrosion rate and film formation and removal conditions in the tube side inlet section of heat exchangers where severe erosion-corrosion problems often occur.
2. 3-D turbulence model should be used in the future work as more powerful computers are available. Such a model should be able to predict the error in electrochemical rate measurement and to determine the effect of electrode misalignment on electrochemical corrosion rate measurement in turbulent pipe flow with small round electrodes installed in the pipe wall.
3. Future experimental work should enable study of the corrosion rate and the film formation and destruction under well controlled hydrodynamic and water chemistry

conditions and enable the application of advanced optical techniques to observe the film growth and removal under various disturbed flow conditions. The concentration of dissolved O_2, solution pH and solution chemical composition should be monitored and controlled continuously. Electrochemical measurement techniques should be used to determine the corrosion rate, corrosion potential and other kinetic parameters (exchange current density and Tafel slopes) under various flow conditions. The relevant parameters obtained during experiment will be input into the turbulence model and the corrosion model. The predicted film formation and removal conditions will be compared with the observed film formation and removal conditions.

BIBLIOGRAPHY

Abe, K., Kondoh, T. and Nagano, Y., "A new turbulence model for predicting fluid flow and heat transfer in separating and reattaching flows-I. Flow field calculations," *Int. J. Heat Mass Transfer*, Vol. 37, No. 1, pp. 139~151 (1994).

Adamopoulos, G. E., "Numerical simulations of erosion-corrosion in 2-D bends", Ph.D. Thesis, University of Saskatchewan (1995).

Amano, R. S., "A study of turbulent flow downstream of an abrupt pipe expansion", *AIAA J*, Vol. 21, pp. 1400~1405 (1983).

Amano, R. S., "A study of turbulent mass transport downstream of an abrupt pipe expansion", *Numerical Heat Transfer*, Vol. 8, pp. 361~371 (1985).

Bacarella, A. L. and Griess, Jr. J. C., "The anodic dissolution of copper in flowing sodium chloride solutions between 25° and 175°C", *J. Electrochem. Soc.*, Vol. 120, No. 4, pp. 459~465 (1973).

Back, L. H. and Roschke, E. J., "Shear-Layer flow regimes and wave instabilities and reattachment lengths downstream of an abrupt circular channel expansion", *ASME, J. Appl. Mech.*, Vol. 94, pp. 677~681 (1972).

Baldwin, B. S. and Lomax, H., "Thin-layer approximation and algebraic model for separated turbulent flows", AIAA Paper 78-257, Huntsville, AL. (1978).

Berger, F. P. and Hau, K.-F. F.-L., "Mass transfer in turbulent pipe flow measured by the electrochemical method", *Int. J. Heat Mass Transfer*, Vol. 20, pp. 1185~1194 (1977).

Berger, F. P. and Ziai, A., "Optimization of experimental conditions for electrochemical mass transfer measurements", *Chem. Eng. Res. Des.*, Vol. 61, pp. 377~382 (1983).

Bianchi, G., and Longhi, P., "Copper in sea-water, potential-pH diagrams", *Corrosion Science*, Vol. 13, pp. 853~864 (1973).

Bianchi, G., Fiori, G., Longhi, P. and Mazza, F., "'Horse shoe' corrosion of copper alloys in flowing sea water: mechanism, and possibility of cathodic protection of condenser tubes in power stations", *Corrosion*, Vol. 34, p. 396 (1978).

Bjorndahl, W. D. and Nobe, K., "Copper corrosion in chloride media. Effect of oxygen", *Corrosion*, Vol. 40, p. 82 (1984).

Blatt, W. and Heitz, E., "Hydromechanical measurements for erosion corrosion", Corrosion/90. Paper no. 25 (Houston, TX: NACE, 1990).

Bockris , J. O'M., Drazic, D. and Despic, A. R., "The electrode kinetics of the deposition and dissolution of iron", *Electrochim. Acta*, Vol. 4, pp. 325~360 (1961).

Boussinesq, J., "Theorie de l'Ecoulement Tourbillant," *Mem. Presentes par Divers Savants Acad. Sci. Inst. Fr.*, Vol. 23, pp. 46-50 (1877).

Cebeci, T. And Smith, A. M. O., "Analysis of Turbulent Boundary Layer", Ser. In Appl. Math. & Mech., Vol. XV, Academic Press. (1974).

Chang, K. C, Hsieh, W. D., and Chen, C. S., "A modified low-Reynolds-number turbulence model applicable to recirculating flow in pipe expansion", *ASME J. Fluids Eng.*, Vol. 117, pp. 417~423 (1995).

Chexal, B., Horowitz, J., Jones, R., Dooley B., Wood, C., Bouchacourt M., Remy, F., Nordmann, F. and St. Paul, P., "Flow-accelerated corrosion in power plants", Electric Power Research Institute, Inc., France, pp. 1-7~1-9 (1996).

Cho, H. H. and Goldstein, R. J., "An improved low-Reynolds-number k-ε turbulence model for recirculating flows", *Int. J. Heat Mass Transfer*, Vol. 37, No. 10, pp. 1495~1508 (1994).

Copson, H. R., "Effects of velocity on corrosion by water", *Ind. Eng. Chem.*, Vol. 44, p. 1745 (1952).

Crooks, R. D., "Copper corrosion causes concern", *Materials Performance*, Vol. 32, No. 4, pp. 72~73 (1993).

Cussler, E. L., *Diffusion, Mass transfer in fluid system*, Cambridge University Press, Cambridge, pp. 123~157 (1984).

Danek, G. J. Jr., "The effect of sea-water velocity on the corrosion behavior of metals", *Naval Engineers J.*, Vol. 78, pp. 763~769 (1966).

Dawson, J. L. and Shih, C. C., "Corrosion under flowing conditions-An overview and model", Corrosion/90, paper no. 21 (Houston, TX: NACE, 1995).

Deslouis, C., Tribollet, B., Mengoli, G. and Musiani, M. M., "Electrochemical behaviour of copper in neutral aerated chloride solution. I. Steady-state investigation", *J. of Applied Electrochem.*, Vol. 18, pp. 374~383 (1988).

Deslouis, C., Tribollet, B. and Viet, L., "Local and overall mass transfer rates to a rotating disk in turbulent and transient flows", *Electrochimica Acta*, Vol. 25, pp. 1027~1032 (1980).

Deslouis, C., Gabrielli, C. and Tribollet, B., "Multi-channel potentiostatic control in electrochemistry: localized mass-transfer rates at the rotating disc electrode", *Physicochemical Hydrodynamics*, Vol. 2, pp. 23~30 (1981).

DeWaard, C. and Milliams, D. E., "Carbonic acid corrosion of steel", *Corrosion*, Vol. 31, p. 177 (1975).

DeWaard, C. and Lotz, U., "Prediction of CO_2 corrosion of carbon steel", Corrosion/93, paper no. 69 (Houston, TX: NACE, 1993).

Durret, R. P., Stevenson, W. H., and Thompsom, H. D., "Radial and axial turbulent flow measurements with an LDV in an axisymmetrical sudden expansion air flow", *ASME J. Fluids Eng.*, Vol. 110, pp. 367~372 (1988).

Dustad, A., Lunde, L. and Videm, K., "Parametric study of CO_2 corrosion of carbon steel", Corrosion/94, paper no. 14 (Houston, TX: NACE, 1994).

Efird, K. D., "Effect of fluid dynamics on the corrosion of copper base alloys in sea water", *Corrosion*, Vol. 33, No. 1, pp. 3~8 (1977).

Efird, K. D., Wright E. J., Boros J. A. and T. G. Hailey, "Correlation of steel corrosion in pipe flow with jet impingement and rotating cylinder tests", *Corrosion*, Vol. 49, p. 992 (1993).

Eriksrud, E. and Sontvedt, T., "Effect of flow on CO_2 corrosion rates in real and synthetic formation waters." Corrosion/83, paper no. 44 (Houston, TX: NACE, 1983).

Engell, H. and Forchhammer, P., " Uber die veranderung des pH-werles an metalloberflachen bei kalhodischem Schutz in meerwasser", *Corrosion Science*, Vol. 5, p. 479 (1965).

Eisenberg, M., Tobias, C. W. and Wilke, C. R., *J. Electrochem. Soc.*, Vol. 101, p. 306 (1954).

Evans, U. R., *The Oxidation and corrosion of metals*, Arnold Publishers, London, pp. 906~1035 (1960).

Faita, G., Fiori, G. and Salvadore, D., "Copper behaviour in acid and alkaline brines--I Kinetics of anodic dissolution in 0.5M NaCl and free corrosion rates in the presence of oxygen", *Corrosion Science* Vol. 15, p. 383 (1975).

Farhanieh, B., Davidson, L., and Suden, B. "Employment of second-moment closure for calculation of turbulent recirculating flows in complex geometry with collocated variable arrangement,: *Int. J. of numerical methods for fluids*, Vol. 16, pp. 525~544 (1993).

Furuta, T., Okazaki, M. and Toei, R., "The effect of the insulation of an isolated electrode on measurements of local mass transfer coefficients by electrochemical method", *J. of Chem. Eng. of Japan*, Vol. 7, p. 350 (1974).

Goldberg, U. C., "Derivation and testing of a one-equation model based on two time scales," *AIAA Journal*, Vol. 29, No. 8, pp. 1337~1340 (1991).

Gosman, A. D., Khalil, E. E. and Whitelaw, J. H., "The calculation of two-dimensional turbulent recirculating flows," in *Turbulent shear flows I*, Durst, F., Launder, B. E., Schmidt, F. W., and Whitelaw, J. H., Eds., Springer-Verlag, New York, pp. 237~255 (1980).

Gould, R. D., Stevenson, W. H. and Thompson, H. D., "Investigation of turbulent transport in an axisymmetric sudden expansion", *AIAA J.*, Vol. 28, pp. 276~283 (1990).

Gray, L. G. S., Anderson, B. G., Danysh, M. J. and Tremaine, P. G., "Mechanism of carbon steel corrosion in brines containing dissolved carbon dioxide at pH 4", Corrosion/89. Paper no. 464 (Houston, TX: NACE, 1989).

Gray, L. G. S., Anderson, B. G., Danysh, M. J. and Tremaine, P. G., "Effect of pH and temperature on the mechanism of carbon steel corrosion by aqueous carbon dioxide", Corrosion/90. Paper no. 40 (Houston, TX: NACE, 1990).

Hanjalic, K and Launder, B. E., "Contribution towards a Reynolds-stress closure for low-Reynolds-number turbulence", *J. of Fluid Mechanics*, Vol. 74, pp. 593~610 (1976).

Harlow, F. H. and Nakayama, P., "Transport of turbulence energy decay rate" Los Alamos Science Lab., University of California Report La-3854 (1968).

Herrero, J., Grau, F. X, Grifoll, J. and Giralt, F., "A near wall k-ε formulation for high Prandtl number heat transfer", *Int. J. Heat Mass Transfer*, Vol. 34, No. 3, pp. 711~721 (1991).

Herrero, J., Grau, F. X, Grifoll, J. and Giralt, F., "The effect of grid size in near-wall k-ε calculations of mass transfer rates at high Schmidt numbers", *Int. J. Heat Mass Transfer*, Vol. 37, No. 5, pp. 882~884 (1994).

Hinze, J. "Turbulence," 2nd Ed., McGraw-Hill, New York (1975).

Hoffmann, K. A., "Computational fluid dynamics for engineering", Engineering Education System™, Austin, Texas (1989).

Jones, W. P. and Launder. B. E., "The prediction of laminarization with a two-equation model of turbulence," *Int. J. Heat Mass Transfer*, Vol. 15, PP. 301~314 (1972).

Jones, W. P. and Launder. B. E., "The calculation of low-Reynolds number phenomena with a two-equation model of turbulence," *Int. J. Heat Mass Transfer*, Vol. 16, pp. 1119~1130 (1973).

Kays, W. M. and Crawford, M. E., "Convective heat and mass transfer", McGraw-Hill, New York, pp. 225~229 (1980).

Kim, J., Moin, P. and Moser, R., "Turbulence Statistics in fully developed channel flow at low Reynolds number," *J. of Fluid Mechanics*, Vol. 177, pp. 133~166 (1987).

King, F. and Litke, C. D., "The electrochemical behaviour of copper in aerated 1 mol dm^{-3} NaCl at room temperature. Part 1. Anodic dissolution of copper", Atomic Energy of Canada Limited Report, AECL-9571 (1989).

Kolmogorov, A. N., "Equation of turbulent motion of an incompressible fluid", *Izvestia academy of sciences, USSR; Physics*, Vol. 6, Nos. 1 and 2, pp. 56~58 (1942).

Kudova, A. K. and Sesonske, A., "Structure of turbulent viscosity and temperature fields in ethylene glycol pipe flow at low Reynolds number, *Int. J. Heat Mass Transfer*, Vol. 15, p. 12 (1972).

Lam, C. K. G. and Bremhorst, K. "A modified form of the k-ε model for predicting wall turbulence," *ASME J. Fluids Eng.*, Vol. 103, pp. 456~460 (1981).

Launder, B. E., "Second - Moment closure: Present and Future", *Int. J. Heat Fluid Flow*, Vol. 10, pp. 282-300 (1989).

Launder, B. E. and Sharma, B. I., "Application of the energy dissipation model of turbulence to the calculation of flow near a spinning disc", *Letters in heat and mass transfer*, vol. 1, No. 2, pp. 131~138 (1974).

Launder, B. E. and Spalding, D. B., "The numerical computation of turbulent flows", *Comp. Meth. Appl. Mech. Eng.*, Vol. 3, pp. 269~289 (1974).

Levich, V., "Physicochemical Hydrodynamics," Pretice-Hall, Englewood Cliffs, NJ, pp. 144~154 (1962).

Linton, W. H. and Sherwood, T. K., "Mass transfer from solid shapes to water in streamline and turbulent flow, *Chem. Engng Progr.*, Vol. 46, p. 288 (1950).

Lorenz, W. and Heusler, K., "Anodic Dissolution of Iron Group Metals", in Corrosion Mechanism, ed. F. Mansfeld, Marcel Dekker, New York (1987).

Lotz, U. and Heitz, E. "Flow dependent corrosion-current understanding of the mechanism involved", *Werkestoffe und Korrosion*, Vol. 34, pp. 454~461 (1983).

Lotz U. and Postlethwaite, J., "Erosion-corrosion in disturbed two phase liquid/particle flow", *Corrosion Science*, Vol. 30, pp. 95~106 (1990).

MacDonald, D. D., Syrett, B. C. and Wing, S. S., The corrosion of copper-Nickel alloys 706 and 715 in flowing sea water. I--effect of oxygen, *Corrosion*, Vol. 34, No. 9, pp. 289~301 (1978).

Mahato, B. K., Voora, S. K. and Shemilt L. W., "Steel pipe corrosion under flow conditions. I. An isothermal correlation for a mass transfer model", *Corrosion Science*, Vol. 8, p. 173 (1968).

Martinuzzi, R. and Pollard, A. "Comparative study of turbulence models in predicting turbulent pipe flow. Part I: Algebraic stress and k-ε models", *AIAA J.*, Vol. 27, pp. 29~36 (1989).

Mattsson, E. and Bockris, J. O'M., "Galvanostatic studies of the kinetics of deposition and discussion in the copper + copper sulphate system", *Trans. Faraday Soc.* Vol. 55, pp. 1586~1601 (1959).

Melton, D. G., Evaluation of copper piping with grooved mechanical connectors, Corrosion report—A technical publication of LaQue center for CORROSION TECHNOLOGY, INC., Vol. 6, No. 1 (1991).

Meyerink, E. S. C. and Friedlander, S. K., "Diffusion and diffusion controlled reaction in fully developed turbulent pipe flow", *Chem. Eng. Sci.*, Vol. 17, p. 121 (1962).

Myong, H. K., Kasagi, N. and Hirata, M., "Numerical prediction of turbulent pipe flow heat transfer for various Prandtl number fluids with the improved k-ε turbulence model", *JSME Int. J.*, ser. II, Vol. 32, No. 4, pp. 613~622 (1989).

Myong, H. K. and Kasagi, N., "A new approach to the improvement of k-ε turbulence model for wall-bounded shear flows," *JSME Int. J.*, ser. III, Vol. 33, No. 1, pp. 63~72 (1990)

Nagano, Y. and Tagawa, M., "An improved k-ε model for boundary layer flows," *ASME J. Fluids Eng.*, Vol. 112, pp. 33~39 (1990).

Nagy, Z., "Application of non-equilibrium thermodynamics to the theory of overvoltage", *Electrochimica Acta*, Vol. 22, pp. 191~195 (1977).

Nallasamy, M., "Turbulence models and their applications to the prediction of internal flows: A review," *Computers and Fluids*, Vol. 15, No. 2, pp. 151~194 (1987).

Nesic, S., "Computation of localized erosion-corrosion in disturbed two-phase flow", Ph.D. Thesis, University of Saskatchewan (1991).

Nesic, S. and Postlethwaite, J., "Relationship between the structure of disturbed flow and erosion-corrosion", *Corrosion*, Vol. 46, p. 874 (1990).

Nesic, S. and Postlethwaite, J., "Hydrodynamics of disturbed flow and erosion-corrosion. Part I. Single-phase flow study", *Can. J. Chem. Eng.*, Vol. 69, pp. 698~703 (1991a).

Nesic, S. and Postlethwaite, J., "Hydrodynamics of disturbed flow and erosion-corrosion. Part II. two-phase flow study", *Can. J. Chem. Eng.*, Vol. 69, pp. 704~710 (1991b).

Nesic, S. and Postlethwaite, J., "A predictive model for localized erosion-corrosion", *Corrosion*, Vol. 47, p.582 (1991c).

Nesic, S., Postlethwaite, J. and Bergstrom D. J., "Calculation of wall-mass transfer rates in separated aqueous flow using a low Reynolds number k-ε model", *Int. J. Heat Mass Transfer*, Vol. 35, pp. 1977~1985 (1992).

Nesic, S., Postlethwaite, J. and Olsen, S., "An electrochemical model for prediction of corrosion of mild steel in aqueous carbon dioxide solutions" *Corrosion*, Vol. 52, pp. 280~294 (1996).

Nesic, S., Solvi, G. T. and Enerhaug, J., "Comparison of the rotating cylinder and pipe flow tests for flow-sensitive carbon dioxide corrosion", *Corrosion*, Vol. 51, pp. 773~787 (1995).

Newman, J., "Mass Transport and Potential Distribution in the Geometries of Localized Corrosion" NACE-3, pp. 45~61 (1974).

Nikjooy, M., and Mongia, H. C., "A second-order modelling study of confined swirling flow," *Int. J. of Heat and Fluid Flow*, Vol. 12, pp. 12~18 (1991).

Parsons, R., *Handbook of electrochemical constants*, Academic Press, New York, p. 85 (1959).

Patankar, S. V., "Numerical heat transfer and fluid flow", McGraw-Hill, New York (1980).

Patankar S. V. and Spalding, D. B., A calculation procedure for heat, mass and momentum transfer in three-dimensional parabolic flows", *Int. J. heat Mass Transfer*, Vol. 15, pp. 1787~1806 (1972).

Patel, V. C., Rodi, W. and Scheuerer, G., "Turbulence models for near-wall and low Reynolds number flows: A review", *AIAA J.* Vol. 23, No. 9, pp. 1308~1319 (1985).

Pollard, A. and Martinuzzi, R., "Comparative study of turbulent models in predicting turbulent pipe flow. Part II: Reynolds stress and k-ε models", *AIAA J.*, Vol. 27, pp. 1714~1721 (1989).

Postlethwaite, J., "Effect of resistance to mass transport on $M^{z+} + z\,e^{-} \Leftrightarrow M$ reaction", *Electrochim. Acta*, Vol. 15, p. 1847 (1970).

Postlethwaite, J., "Electrochemical studies of inhibitors in aqueous slurries of sand, iron ore, and coal", *Corrosion*, Vol. 35, pp. 475~480 (1979).

Postlethwaite, J. and Lotz, U., "Mass transfer at erosion-corrosion roughened surfaces", *Can. J. Chem. Eng.*, Vol. 66, p. 75 (1988).

Postlethwaite, J. and Sharp, D. M., "Interfacial concentration in aqueous corrosion process", *Trans. Instn Chem. Engrs*, Vol. 47, p. 198 (1969).

Postlethwaite, J., Dobbin, M. H. and Bergvin, K., "The role of oxygen mass transfer in the erosion-corrosion of slurry pipelines", *Corrosion*, Vol. 42, pp. 514~521 (1986).

Postlethwaite, J., Fiadzigbe, E. and Aruliah, S., "Effect of solution flow on the anodic dissolution of copper and mild steel", *Corrosion*, Vol. 34, p. 85 (1978).

Postlethwaite, J., and Wang, Y., "Numerical simulation of the effects of electrode misalignment and electrode length on the determination of corrosion rates in turbulent pipe flow", *Proceedings of 13th international Corrosion congress*, Melbourne, Australia, Paper No. 435 (1996).

Pourbaix, M., "*Atlas of electrochemical equilibria in aqueous solution*", p. 313, Pergamon Press (1966).

Prandtl, L. "Uberdie ausgebildete Turbulenz", *ZAMM*, Vol. 5, p.136. (1925).

Prandtl, L., "Uber ein neues formelsystem fur die ausgebildete turbulenz," *Nacr. Akad. Wiss. Gottingen, Math-Phys. Kl. 1945*, pp. 6~19 (1945).

Reynolds, O., "On the dynamic theory of incompressible viscous fluids and the determination of the criterion", *Philosophical transactions of the Royal society of London, Series A*, Vol. 186, p. 123 (1895).

Rotta, J. C., "Statistische theorie nichthomogener turbulenz," Zeitschrift fur physik, Vil. 129, pp. 547~572 (1951).

Runchal, A. K, "Mass transfer investigation in turbulent flow downstream of sudden enlargement of a circular pipe for very high Schmidt numbers", *Int. J. Heat Mass Transfer*, Vol. 14, pp. 781~792 (1971).

Saffman, P. G. and Wilcox, D. C., "Turbulence-model predictions for turbulent boundary layers," *AIAA Journal*, Vol. 12, No. 4, pp. 541~546 (1974).

Schlichting H., "Boundary layer theory", 7th edition, McGraw-Hill, New York (1979).

Schutz, G., "Untersuchung des stoffausch-anlaufgebietes in einem rohr bei vollausgebildeter hydrodynamischer stromung mit einer elektrochemischen method", *Int. J. Heat Mass Transfer*, Vol. 7, pp. 1077~1082 (1964).

Shah, D. A. and Antonia, R. A., "Scaling of wall shear stress fluctuations in a turbulent duct flow", *AIAA J.*, Vol. 25, pp. 22-29 (1986).

Shaw, D. A. and Hanratty, T. J., "Turbulent mass transfer rate to a wall for large Schmidt Numbers", *AIChE J.* Vol. 23, pp. 28~37 (1977).

Shaw, P. V., Ph.D. thesis, University of Illinois, Urbana (1963).

Shaw, P. V., Reiss, L. P. and Hanratty, T. J., "Rates of turbulent transfer to a pipe wall in the mass transfer entry region", *AIChE J.* Vol. 9, p. 362 (1963).

Shemilt, L. W., Cha, C. Y., Fiadzigbe, and Ponter, A. B., "Steel pipe corrosion under flow conditions. III. Effect of sulphate ion", *Corrosion Science*, Vol. 20, pp. 443~455 (1980).

Sillen, L. G. and Martell, A. E., "*Stability constants of metal-ion complexes*", The Chem. Soc., Spec. Pub. No. 17, London (1964).

Silverman, D. C., "Rotating cylinder electrode for velocity sensitivity testing", *Corrosion*, Vol. 40, pp. 220~226 (1984).

Smyrl, W. H., "Digital impedance for Faradac analysis", *J. Electrochem. Soc.*, Vol. 132, pp. 1555~1562 (1985).

Son, J. S., M.Sc. thesis, University of Illinois, Urbana (1965).

Son, J. S. and Hanratty, T. J., "Limiting relation for the eddy diffusivity close to a wall", *AIChE J.*, Vol. 13, p. 689 (1967).

Sprague, P. J., Ph.D. thesis, Exeter University U.K. (1984).

Sydberger, T. and Lotz, U., "Relation between mass transfer and corrosion in a turbulent pipe flow", *J. Electrochem. Soc.*, Vol. 129, No. 2, pp. 276~283 (1982).

Syrett, B. C., "Erosion-corrosion of copper nickel alloys in sea water and other aqueous environments -- a literature review", *Corrosion*, Vol. 32, No. 6, pp. 242~252 (1976).

Tribollet, B. and Newman, J., "Impedance model for a concentrated solution", *J. Electrochem. Soc.*, Vol. 131, pp. 2780~2785 (1984).

Turgoose, S., Dawson, J. L., Palmer, J. W. and Rizk, T., "Boundary layer effects in turbulent flow testing", Corrosion/95, paper no. 112 (Houston, TX: NACE, 1995).

Wang, Y., and Postlethwaite, J., "Application of low Reynolds number k-ε turbulence model to corrosion modelling in the mass transfer entrance region", *Corrosion Science*, in press (1997).

Wang, Y., Postlethwaite, J. and Bergstrom, D. J., "Modelling mass transfer entrance lengths in turbulent pipe-flow with application to small cathodes for measuring local mass transfer rates", *J. of Applied Electrochem.*, Vol. 26, pp. 471~479 (1996).

Wang, Y., Postlethwaite, J., and Bergstrom, D. J., "Effects of "non-flush" pipe-wall working electrodes on electrochemical corrosion rate measurements in pipes", *Corrosion*, in press (1997).

Wein, O. and Wichterle, K., *Collec. Czech. Chem. Commun.*, Vol. 54, p. 3198 (1989).

Wilcox, D. C., "Turbulence Modelling for CFD," DCW industries, California (1993).

Wood, R. J. K., Hutton, S. P. and Schiffrin, D. J., "Mass transfer effects of non-cavitating seawater on the corrosion of Cu and 70Cu-30Ni", *Corrosion Science*, Vol. 30, pp. 1177~1201 (1990).

Wragg, A. A., "Application of the limiting diffusion current technique in chemical engineering", *The Chemical Engineer*, No. 316, January, pp. 39~44 (1977).

Yapici, S., Patrick, M. A., and Wragg, A. A., "Electrochemical study of mass transfer in decaying annular swirl flow. Part 1: Axial distribution of local mass transfer coefficients", *J. of Applied Electrochem.*, Vol. 24, pp. 685~693 (1994).

Appendix I Derivation of general rate equation for iron dissolution taking into account the effect of OH^-

General equation $Fe = Fe^{2+} + 2e$

Mechanism (Bockris et al, 1961):

$$Fe + OH^- \longleftrightarrow FeOH + e$$

$$FeOH \xrightarrow{R.D.S} FeOH^+ + e$$

$$FeOH^+ \longleftrightarrow Fe^{2+} + OH^-$$

From Bockris et al (1961):

$$i_a = k_a\left[OH^-\right]^{n_{OH^-}} \exp\left(\frac{\alpha_a FE}{RT}\right) \quad (1)$$

$$i_c = k_c\left[OH^-\right]^{n_{OH^-}}\left[Fe^{2+}\right]^{n_{Fe^{2+}}} \exp\left(-\frac{\alpha_c FE}{RT}\right) \quad (2)$$

Let $f = \frac{F}{RT}$. equations (1) and (2) become:

$$i_a = k_a\left[OH^-\right]^{n_{OH^-}} \exp\left(\alpha_a fE\right) \quad (3)$$

$$i_c = k_c\left[OH^-\right]^{n_{OH^-}}\left[Fe^{2+}\right]^{n_{Fe^{2+}}}\exp\left(-\alpha_c FE\right) \tag{4}$$

at $E = E_e$

$$i_a = i_0 = k_a\left[OH^-\right]^{n_{OH^-}}\exp\left[\alpha_a f\left(E^0 + \frac{1}{zf}\ln[Fe^{2+}]\right)\right]$$

or $$i_0 = k_a\left[OH^-\right]^{n_{OH^-}}[Fe^{2+}]^{\frac{\partial_a}{z}}\exp(\alpha_a fE^0) \tag{5}$$

and

$$i_c = i_0 = k_c\left[OH^-\right]^{n_{OH^-}}[Fe^{2+}]^{n_{Fe^{2+}}}\exp\left[-\alpha_c f\left(E^0 + \frac{1}{zf}\ln[Fe^{2+}]\right)\right]$$

or $$i_0 = k_c\left[OH^-\right]^{n_{OH^-}}[Fe^{2+}]^{n_{Fe^{2+}}-\frac{\partial_a}{z}}\exp(-\alpha_c fE^0) \tag{6}$$

Net current density:

$$i = i_a - i_c = k_a\left[OH^-\right]^{n_{OH^-}}\exp\left(\alpha_a fE\right) - k_c\left[OH^-\right]^{n_{OH^-}}\left[Fe^{2+}\right]^{n_{Fe^{2+}}}\exp\left(-\alpha_c FE\right) \tag{7}$$

From equations (6) and (7)

$$\frac{i}{i_0} = \frac{k_a\left[OH^-\right]^{n_{OH^-}}\exp\left(\alpha_a fE\right)}{k_a\left[OH^-\right]^{n_{OH^-}}\exp\left(\alpha_a fE_e\right)} - \frac{k_c\left[OH^-\right]^{n_{OH^-}}\left[Fe^{2+}\right]^{n_{Fe^{2+}}}\exp\left(-\alpha_c FE\right)}{k_c\left[OH^-\right]^{n_{OH^-}}\left[Fe^{2+}\right]^{n_{Fe^{2+}}}\exp\left(-\alpha_c FE_e\right)} \tag{8}$$

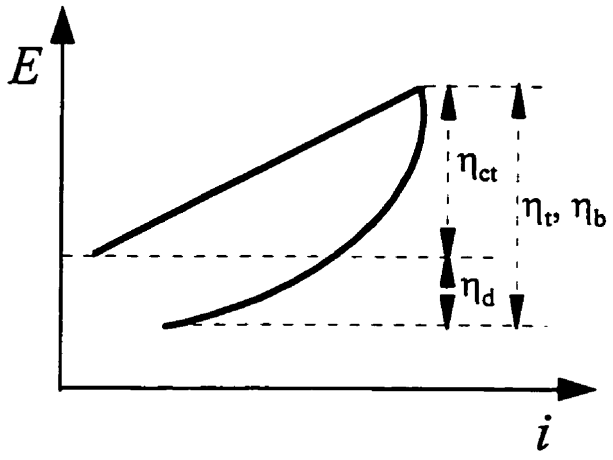

Fig. I Schematic overpotential-current diagram.

Let $\eta_{ct} = E - E_e$, equation (8) becomes

$$i = i_0\left[\exp(\alpha_a f\eta_{ct}) - \exp(-\alpha_c f\eta_{ct})\right] \tag{9}$$

Since $\eta_t = \eta_{ct} + \eta_d$, and $\eta_d = \dfrac{RT}{zF}\ln\left(\dfrac{[Fe^{2+}]_s}{[Fe^{2+}]_b}\right)$

Then $$\eta_{ct} = \eta_t - \frac{1}{zf}\ln\left(\frac{[Fe^{2+}]_s}{[Fe^{2+}]_b}\right) \tag{10}$$

Substitution of equation (10) into equation (9) gives

$$i = (i_0)_s\left[\exp\left(\alpha_a f\left(\eta_t - \frac{1}{zf}\ln\left(\frac{[Fe^{2+}]_s}{[Fe^{2+}]_b}\right)\right)\right) - \exp\left(-\alpha_c f\left(\eta_t - \frac{1}{zf}\ln\left(\frac{[Fe^{2+}]_s}{[Fe^{2+}]_b}\right)\right)\right)\right]$$

or

$$i = (i_0)_s \left[\left(\frac{[Fe^{2+}]_s}{[Fe^{2+}]_b} \right)^{-\frac{\alpha_a}{z}} \exp(\alpha_a f\eta_t) - \left(\frac{[Fe^{2+}]_s}{[Fe^{2+}]_b} \right)^{\frac{\alpha_c}{z}} \exp(-\partial_c f\eta_t) \right]$$

or

$$i = (i_0)_s \left(\frac{[Fe^{2+}]_s}{[Fe^{2+}]_b} \right)^{-\frac{\alpha_a}{z}} \left[\exp(\alpha_a f\eta_t) - \left(\frac{[Fe^{2+}]_s}{[Fe^{2+}]_b} \right)^{\frac{\alpha_a+\alpha_c}{z}} \exp(-\alpha_c f\eta_t) \right] \tag{11}$$

According to Nagy (1977):

$$\alpha_c + \alpha_a = \frac{z}{\nu} \quad \text{and} \quad \nu = 1$$

Therefore, equation (11) becomes

$$i = \underbrace{(i_0)_s \left(\frac{[Fe^{2+}]_s}{[Fe^{2+}]_b} \right)^{-\frac{\alpha_a}{z}}}_{(i_0)_{new}} \left[\exp(\alpha_a f\eta_t) - \left(\frac{[Fe^{2+}]_s}{[Fe^{2+}]_b} \right) \exp(-\alpha_c f\eta_t) \right] \tag{12}$$

From equation (5)

$$(i_0)_s = k_a \left[OH^- \right]_s^{n_{OH^-}} [Fe^{2+}]_s^{\frac{\alpha_a}{z}} \exp(\alpha_a fE^0) \tag{13}$$

Therefore,

$$(i_0)_{new} = k_a \left[OH^- \right]_s^{n_{OH^-}} [Fe^{2+}]_s^{\frac{\alpha_a}{z}} \exp(\alpha_a fE^0) \left(\frac{[Fe^{2+}]_s}{[Fe^{2+}]_b} \right)^{-\frac{\alpha_a}{z}}$$

or $$(i_0)_{new} = k_a \left[OH^- \right]_s^{n_{OH^-}} [Fe^{2+}]_b^{\frac{\alpha_a}{z}} \exp(\alpha_a fE^0)$$

or
$$(i_0)_{new} = (i_0)_b \frac{[OH^-]_s^{n_{OH^-}}}{[OH^-]_b^{n_{OH^-}}} \tag{14}$$

where

$$(i_0)_b = k_a [OH^-]_b^{n_{OH^-}} [Fe^{2+}]_b^{\frac{\alpha_a}{z}} \exp(\alpha_a f E^0) \tag{15}$$

Substituting equation (14) into equation (12) and letting $\eta_b = \eta_t$, we obtain the final form of general rate equation

$$i = (i_0)_b \frac{[OH^-]_s^{n_{OH^-}}}{[OH^-]_b^{n_{OH^-}}} \left[\exp\left(\frac{\alpha_a F}{RT}\eta_b\right) - \left(\frac{[Fe^{2+}]_s}{[Fe^{2+}]_b}\right) \exp\left(-\frac{\alpha_c F}{RT}\eta_b\right) \right] \tag{16}$$

where n=1 (pH<4)

n=0 (pH>4)

α_a=1.5 α_c=0.5 z=2

Appendix II Derivation equation (I) from equation (II)

$$St_d = 0.276\,\mathrm{Re}^{-0.417}\,Sc^{-2/3}\left(\frac{L}{d}\right)^{-1/3} \tag{I}$$

$$< K^+ > = 0.81\,Sc^{-2/3}\,(L^+)^{-1/3} \tag{II}$$

where $St_d = \dfrac{K}{U_b}$ $\qquad Sc = \dfrac{\nu}{D} = \dfrac{\mu}{\rho D}$

$< K^+ > = \dfrac{K}{u_\tau}$ $\qquad L^+ = \dfrac{Lu_\tau}{\nu} = \dfrac{L\rho u_\tau}{\mu}$

Since $u_\tau = \left(\dfrac{\tau_w}{\rho}\right)^{1/2}$ and $\tau_w = \dfrac{1}{8}\lambda\rho U_b{}^2$ (Schlichting, 1979)

then $u_\tau = \left(\dfrac{f}{8}\right)^{1/2} U_b$ where f is friction factor. (III)

Equation (II) can be rewritten as

$$\frac{K}{u_\tau} = 0.81\,Sc^{-2/3}\left(\frac{L\rho u^*}{\mu}\right)^{-1/3} \tag{IV}$$

or
$$\frac{K}{u_\tau} = 0.81\, Sc^{-2/3}\left(\frac{L}{d}\right)^{-1/3}\left(\frac{\rho d u^*}{\mu}\right)^{-1/3} \qquad \text{(V)}$$

Substitution of equation (III) into equation (V) gives

$$\frac{K}{U_b}\left(\frac{f}{8}\right)^{-1/2} = 0.81\, Sc^{-2/3}\left(\frac{L}{d}\right)^{-1/3}\left(\frac{\rho d U_b}{\mu}\left(\frac{f}{8}\right)^{1/2}\right)^{-1/3} \qquad \text{(VI)}$$

or
$$\frac{K}{U_b} = 0.81\, Sc^{-2/3}\left(\frac{L}{d}\right)^{-1/3}\mathrm{Re}^{-1/3}\left(\frac{f}{8}\right)^{1/3} \qquad \text{(VII)}$$

Substitute the Blasius friction relation

$$f = 0.316\,\mathrm{Re}^{-0.25} \qquad 4000 < \mathrm{Re} < 10^5 \qquad \text{(VIII)}$$

into equation (VII) and rearrange equation (VII) we obtain

$$\frac{K}{U_b} = 0.276\, Sc^{-2/3}\left(\frac{L}{d}\right)^{-1/3}\mathrm{Re}^{-5/12} \qquad \text{(IX)}$$

That is

$$\frac{K}{U_b} = 0.276\,\mathrm{Re}^{-0.417}\, Sc^{-2/3}\left(\frac{L}{d}\right)^{-1/3} \qquad \text{(X)}$$

Equation (X) is the same as equation (I), which indicates that equation (II) is equivalent to equation (I).